Quantitative SPECT Image Reconstruction using an Accelerated Monte Carlo based Maximum A–Posteriori (MAP) Algorithm

Quantitative SPECT Image Reconstruction an Accelerated Monte Carlo based Maximum A−Posteriori (MAP) Algorithm

By Muhammad I. Karamat, M. Sc.

A Thesis Submitted to the School of Graduate Studies in Partial Fulfilment of the Requirements for the Degree Doctor of Philosophy

McMaster University DOCTOR OF PHILOSOPHY (2016) Hamilton, Ontario (Medical Physics)

TITLE: Quantitative SPECT Image Reconstruction using an Accelerated Monte Carlo based Maximum A-Posteriori (MAP) Algorithm

AUTHOR: Muhammad I. Karamat, M.Sc. (McMaster University)

SUPERVISOR: Dr. Troy H. Farncombe

NUMBER OF PAGES: xxiv, 142

Abstract

Monte Carlo is an important and well established research tool used in emission tomography. While used extensively in research applications, these techniques are not typically implemented clinically due to their low detection efficiency and long acquisition times. In order to make this computational tool faster, the variance reduction technique known as convolution-based forced detection (CFD) has been implemented into the SIMIND MC code (CFD-SIMIND) by our group. Briefly, at each site of interaction within the object, photons are forced to travel in a direction perpendicular to the detector and are then convolved with a distance dependent blurring kernel specific to that collimator and photon energy. A similar CFD method has already been implemented as an option in the SIMIND Monte Carlo program. The study presented in Chapter 2 performs a comparison between a well established, non-VRT Monte Carlo program, GATE, with our accelerated CFD-SIMIND. The intent of this work is to establish if CFD-SIMIND can either replace or be used in conjunction with GATE in order to gain significant reduction in simulation times for low and medium energy isotopes. A number of simulation studies were performed using point sources in air and water, along with the 3D XCAT phantom and a rectangular sheet source for ^{99m}Tc with low and medium energy collimator and ^{111}In with medium energy collimator. A comparison in the projection domain was then performed in terms of spatial resolution, sensitivity, image profiles and energy spectra. The study has shown percent differences of between 3−5% in sensitivity between CFD-SIMIND and GATE with mean universal image quality index value of 0.994 ± 0.009 and spatial resolution within 0.2 mm of each other. CFD-SIMIND offers a significant reduction in simulation time by a factor of 5−6 orders of magnitude compared to GATE. This acceleration time is useful for many applications. This study also provides an objective tool that can help to determine if CFD-SIMIND can be used in place of GATE in order to achieve images of sufficient quality within a reduced time and at much lower computational cost.

Simultaneous multi-isotope SPECT imaging has a number of applications in cardiac, brain and cancer imaging. The major concern however, is the significant crosstalk contamination due to photon scatter between the different isotopes. The second study (Chapter 3) focuses on a method of downscatter compensation between two isotopes

in simultaneous dual isotope SPECT acquisition applied to cancer imaging using ^{99m}Tc and ^{111}In. We have developed an iterative image reconstruction technique that simulates the photon down-scatter from one isotope into the acquisition window of a second isotope. Our approach uses CFD-SIMIND for the forward projection step in an iterative reconstruction algorithm. The MC estimated scatter contamination of a radionuclide contained in a given projection view is then used to compensate for the photon contamination in the acquisition window of other nuclide. We use a modified ordered subset-expectation maximization (OS-EM) algorithm named simultaneous ordered subset-expectation maximization (Sim-OSEM), to perform this step. In this study, we have undertaken a number of simulation tests and phantom studies to verify this approach. The proposed reconstruction technique was also evaluated by reconstruction of experimentally acquired phantom data. Reconstruction using Sim-OSEM showed very promising results in terms of contrast recovery and uniformity of object background compared to alternative reconstruction methods implementing alternative scatter correction schemes (i.e., triple energy window or separately acquired projection data). In this study the evaluation is based on the quality of reconstructed images and activity estimated using Sim-OSEM. In order to quantitate the possible improvement in spatial resolution and signal to noise ratio (SNR) observed in this study, further simulation and experimental studies are required.

It is perceived that in simultaneous dual-isotope breast SPECT studies using ^{123}I-labelled Z-MIVE and ^{99m}Tc-sestamibi, ^{123}I-labelled Z-MIVE not only detects the presence of estrogen receptor (ER) but, also thought to complement ^{99m}Tc-sestamibi in differentiating between benign and malignant breast lesions for patients with breast cancer (Chapter 4). The major concern in simultaneous ^{99m}Tc/^{123}I SPECT is the significant crosstalk contamination between the different isotopes used. The current study focuses on a method of crosstalk (downscatter and spillover) compensation between two isotopes with data acquired using Thallium activated Sodium Iodide (NaI(Tl)) detector (Energy resolution 9.8% at 140 keV) and Cadmium Zinc Telluride (CZT) detector (Energy resolution 5% 140 keV) respectively. The study uses Sim-OSEM for crosstalk compensation between the isotopes. We have undertaken a number of simulation studies using our modeled breast phantom to verify this approach. Reconstruction using Sim-OSEM showed very promising results in terms of crosstalk and scatter compensation and uniformity of background. In our case images obtained using Sim-OSEM were comparable or even better than the images reconstructed from

separately acquired projection data using analytical attenuation based reconstruction. This may be due to better small angle scatter compensation in case of Sim-OSEM as CFD-SIMIND based MC forward projector was used.

Compensation of the image degradation effects (i.e. attenuation, scatter and collimator-detector response) is necessary for an accurate quantification in SPECT imaging. We have previously proposed an accelerated Monte Carlo (MC) based iterative SPECT reconstruction algorithm that accurately corrects for attenuation and scatter once provided with attenuation information (Chapters 3 and 4). This algorithm uses SIMIND MC program accelerated through the implementation of a variance reduction technique known as, convolution forced detection (CFD), (CFD-SIMIND). With ever increasing number of hybrid SPECT/CT systems, CT-based attenuation correction is becoming a standard clinical protocol. This co-registered CT image with SPECT data can also be used to incorporate anatomical information as a prior into a *maximum a-posteriori* (MAP) SPECT image reconstruction algorithm. The study presented in Chapter 5 proposes a MAP reconstruction algorithm that includes CFD-SIMIND as a forward projector and a CT-image as an anatomical prior (CFD-AMAP) for simultaneous compensation of scatter and attenuation and, enhancement of spatial resolution during reconstruction. We have performed a number of simulation and experimental studies to elaborate the advantages of CFD-AMAP. These studies show an accurate quantification (within $\pm 5\%$ and $\pm 8\%$ for simulation and experimental studies respectively) accompanied by a significant reduction in coefficient of variation (CoV). This reduction of CoV results in an improved boundary delineation and the Gibbs artifact compensation. However, this compensation comes at the cost of loss of an overall contrast in the reconstructed images due to a more uniform distribution of estimated activity over the regions of interest (ROI's).

Further studies with more complex phantoms and real patient data, task-based ROC studies, improvement in CFD-SIMIND in terms of speed and use of better Bayesian image reconstruction algorithms are needed to elaborate on the strengths and weaknesses of this proposed MC based forward projector and to pave the way for CFD-SIMIND based image reconstruction algorithms from research to clinic.

Acknowledgements

All the praise for Allah, **The beneficent**, **The Merciful** who guides us in darkness and helps us in difficulties. I firmly believe that Allah never spoils any effort.

All and every kind of praise is for Holy Prophet (PBUH) who is really a source of light for awareness of our minds.

I would like to thank Department of Medical Physics and Applied Radiation Sciences and Hamilton Heath Sciences for giving me chance and privilege to study at one of the top universities of the world.

My deep sense of gratitude and thanks for my research supervisor, **Dr. Troy H. Farncombe** for providing me guidance, support, advice and every kind of help in my research work. I felt myself more researcher in his company and supervision.

I express my heart felt gratitude to my teachers and instructors for their exceptional teaching and guidance during the course of my degree.

My great thanks goes to supervisory committee members, **Dr. Tom Farrell** and **Dr. Soo Hyun Byun** for their guidance, help and time during the course of this work.

This work would not have been possible without the funding from numerous organizations. I would like to acknowledge the financial support provided by the Ontario Institute Cancer Research (OICR) under Smarter Imaging Program. I would also like to acknowledge Government of Ontario for providing funds in part for this work.

I greatly appreciate the help and suggestions from all of my colleagues A. Tao and Dost Khan.

I am thankful to staff at Nuclear Medicine Department, McMaster University Medical Center (MUMC) especially Cheryl, Scott, Sandra, Sue and Joon for helping and assisting me in the experiments performed during this work. I would like also to thank administrative staff at Department of Medical Physics and Applied Radiation Sciences and Nuclear Medicine Department at MUMC for helping and facilitating me during the course of this work.

I extend my heart-felt gratitude and special regards to my most respectable and affectionate parents, Karamat Ali and Shahnaz Begum. Although they are no longer

in this world but, their prayers love and affection will remain an invaluable asset for me. I believe all of my achievements and success are due to their blessings and prayers.

I am grateful to my wife, Bushra for her support encouragement and sacrifices. I can just imagine the difficulties and pains she faced all alone in my busy and stressed times during the course of this work. My love and thanks to my children Areeba, Abdullah and Anabia. They had made my life beautiful and more purposeful. My regards and love to my mother in law and phopho Riaz Begum, for her prayers and great thanks to her for looking after my family in my absence. Finally, I would like to thank my brothers, sisters and friends who always prayed for my success and betterment.

Muhammad Irfan Karamat

November, 2016

To my parents Karamat Ali and Shahnaz Begum, my beautiful wife Bushra Irfan and my lovely and incredible children Areeba, Abdullah and Anabia.

Contents

List of Tables

List of Figures

List of Abbreviations and Symbols

$\mathbf{H^T}$ Backprojector

$\mathbf{H}$ System matrix or forward projector

$\mathbf{P}(\omega, \theta)$ Projection in frequency domain

$\mathbf{p}(\mathbf{s}, \theta)$ Projection in spatial domain

ϕ Azimuthal angle

θ Polar angle

f_j^{new} New updated image estimate

f_j^{old} Current image estimate

Q_{UI} Universal image quality index

ADC Analogue to digital converter

CdT Cadmium Telluride

CFD Convolution forced detection

CFD-SIMIND Accelerated convolution-based forced detection SIMIND Monte Carlo

CoV Coefficient of variation

cps Counts per second

CT Computed tomography

CZT Cadmium Zinc Telluride

EGS Electron gamma shower

FBP Filtered backprojection

FD Forced detection

FOV Field of view

FWHM Full with at half maximum

GEANT Geometry and tracking

IEC-NEMA International Electrotechnical Commission and National Electrical Manufacturing Association

ITS Integrated tiger series

JOSEM Joint ordered subset expectation maximization

LEHR Low energy high resolution

MC Monte Carlo

MCNP Monte Carlo nuclear particle transport

MEGP Medium energy general purpose

MLEM Maximum likelihood expectation maximization

MRI Magnetic resonance imaging

MSE Mean square error

NaI(Tl) Thallium activated sodium iodide detector

NMSE Normalized mean square error

OSEM Ordered subset expectation maximization

OSL One-step-late

PET Positron emission tomography

PMT Photomultiplier tube

PSF Point spread function

PTAR Percent total activity ratio

PVR Peak to valley ratio

Sim-OSEM Simultaneous ordered subset expectation maximization

SIMIND-CFD Accelerated convolution-based forced detection SIMIND Monte Carlo

SiPM Silicon Photomultiplier

SPECT Single photon emission computed tomography

SPET Single photon emission tomography

TEW Triple energy window

VRT Variance reduction technique

XCAT Extended cardiac torso phantom

Chapter 1

Introduction

DIAGNOSTIC imaging is all about bringing invisible to light in a non-invasive or minimally invasive way. Diagnostic nuclear medicine is one such modality that has been used to perform physiological imaging since 1950s [1]. Nuclear medicine involves therapeutic and diagnostic use of radionuclides. The main classes of nuclear medicine imaging involve i) 2D Planar imaging, ii). Single Photon Emission Computed Tomography (SPECT) and iii). Positron Emission Tomography (PET). This work mainly focuses on SPECT imaging that involves the use of gamma ray emitting radionuclides. In diagnostic nuclear medicine trace amounts of radioactivity are administered in order to provide information of diagnostic importance. Radioactivity is generally administered in the form of a radiopharmaceutical (i.e. radioisotope tagged with pharmaceutical to guide the radioisotope to target tissue, organ or system). Activity administration to the patient is performed via intravenous, oral or inhalation routes. With the decay of administered radioisotope, gamma rays are emitted and detected using an external gamma camera. SPECT has number of applications, examples of some such applications are scanning of bones for metastasis or other bone anomalies, myocardial scan to study the function and perfusion of cardiac muscle and brain imaging performed to look for the presence of tumor or to study different mental conditions. This chapter encompasses a detailed description of the steps involved in SPECT imaging and a brief description of the ideas and concepts used in this work. SPECT imaging starts from the selection of a suitable radiopharmaceutical (radionuclide + pharmaceutical) followed by administration to the patient, projection

data acquisition using a gamma camera and finally, image reconstruction.

1.1 Tracer Principle and Radiopharmaceuticals

The tracer principle, developed by George de Hevesy forms the basis of SPECT imaging [1]. This principle is based on the fact that physiologically/chemically gamma emitting radionuclides behave like their non-radioactive counterparts in the body. Therefore, the gamma emission associated with these radionuclides can be used to study physiological processes in the body. After the development of first rectilinear scanner and gamma camera in the 1960s by Benedict Casssen and Hal Anger respectively, ^{131}I was one of the first radiotracers used to scan the thyroid. A radionuclide is rarely administered to the patient in its elemental form these days, and almost always the administration is performed in form of a radiopharmaceutical. ^{131}I, used for thyroid imaging, is one of very a few examples of radionuclides used in their elemental form. This may be the reason that the United States Food and Drug Administration (FDA) defines all the radio-labeled compounds and substances used for diagnosis as radiopharmaceuticals [2].

Some of the considerations for a SPECT radiotracer can easily be derived by using some basic knowledge of radiation physics. For example, a radiotracer should have a type of emission that has range and energy large enough to make out of the patient's body to reach the the detector. The energy should also be small enough for the detector to get fully absorbed in the detector to generate a response. These requirements can easily be fulfilled by gamma emitters having high yield of emission in keV range (e.g. 70-511 keV). Another consideration is the half life of the tracer. The half life should be large enough to allow the radiopharmaceutical to reach the tissue or organ of interest for imaging. At the same time it should be small enough to allow quick removal from the body through biological and physical routes. A half life in minutes to a few hours is ideal for this purpose. High radionuclidic and radiochemical purity, non-toxicity and high affinity for different pharmaceuticals are other important considerations for a SPECT radiotracer [3].

A major breakthrough in the diagnostic nuclear medicine was the development of ^{99}Mo $\rightarrow$ ^{99m}Tc generator in 1960s [2, 3]. ^{99m}Tc meets most if not all of the expectations described earlier. With 140 keV gamma emission and half life of 6 hours, ^{99m}Tc showed flexibility to be labeled to an array of pharmaceuticals that allowed imaging of almost

all the organs of the body [2, 3]. An equally important aspect is the ability of a long lived ^{99}Mo $\rightarrow$ ^{99m}Tc generator to allow on-site and easy access to ^{99m}Tc as per requirement. These advantages have made ^{99m}Tc the most commonly used radionuclide for SPECT imaging [3]. Table 1.1 provides a list of some commonly used SPECT radiopharmaceuticals.

Table 1.1: Some commonly used SPECT radiopharmaceuticals in clinic [1].

Radiopharmaceutical	**Applications**	**Physical Half Life**
^{99m}Tc-DTPA[a]	Lung perfusion and renal obstruction	6.02 h
^{99m}Tc-MDP[b]	Bone fracture and/or metastases	–
^{99m}Tc-RBCs[c]	Liver hemangioma detection	–
^{99m}Tc-sestamibi or tetrofosmin	Myocardial perfusion and/or viability, parathyroid localization	–
^{99m}Tc-sulfur colloid	Liver spleen function	–
^{123}I (NaI)	Thyroid function assessment	13.2 h
^{201}Tl (TlCl)	Myocardial perfusion and/or viability	73.1 h

[a] DTPA, diethylenetriamine pentaacetate; [b] MDP, methylene diphosphonate;
[c] RBCs, red blood cells.

1.2 Image Data Acquisition

The introduction of Anger scintillation camera in late 1950's revolutionized the field of nuclear medicine imaging. This camera uses a large area thallium activated sodium iodide (NaI(Tl)) detector and photomultiplier tubes (PMTs), to significantly increase detection efficiency and reduce acquisition time compared with rectilinear scanner with film based image acquisition. The design of the Anger Camera or gamma camera has significantly been refined since then and has evolved as the most widely used nuclear medicine imaging system (Figure 1.1).

As depicted in Figure 1.1, in modern gamma cameras each PMT is equipped with its own analogue to digital converter (ADC) to perform event positioning and energy calculations using computer software and pre-determined look-up tables respectively. Previously available gamma cameras used analog positioning and summing circuits to perform these operations. These improvements in gamma camera design have

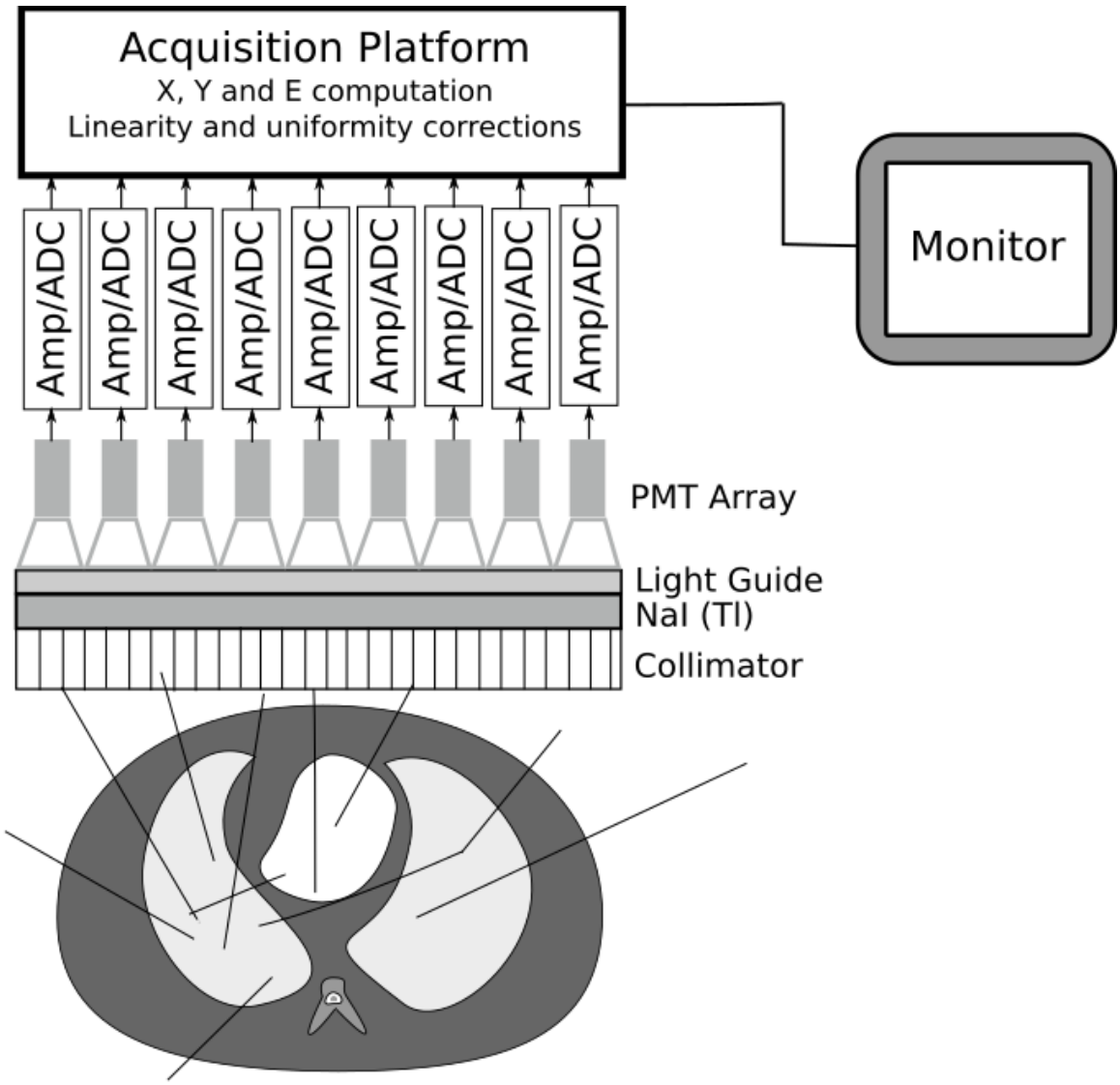

Figure 1.1: Schematic of gamma camera in general.

enabled manufacturers to use fewer PMTs as close packing is not required due to use of computer software.

1.2.1 Collimators

Perhaps, the most important physical advantage of PET over SPECT is 2−3 orders of magnitude higher sensitivity for PET [4]. The main reason for this lower sensitivity in SPECT is the need of a collimator. In SPECT, administration and subsequent deposition of a radiopharmaceutical into a target organ/tissue results in isotropic x-rays or $\gamma-$emission. A collimator is thus required to develop a correspondence between the position of the emission and position of detection on the NaI(Tl) detector. A collimator is essentially a honeycomb made of lead (Pb) that presumably only allow photons that are aligned along the collimator holes to reach the crystal. The photons that hit the collimator walls (known as septa) are assumed to be absorbed. Collimators are classified based on energy and hole orientation. On the basis of energy, collimators are classified as, i) low energy (100−150 keV), ii) medium energy (150−400 keV) and iii) high energy (350 keV and higher) [3]. Even though energy based categorization implies larger collimator septal thickness for higher energy photons, desired collimator sensitivity and amount of activity that can be administered to the patient are the limiting factors for collimator septal thickness and hole size. In reality, septal thickness and hole size are often based on a compromise between these factors and acceptable collimator septal penetration. Based on hole orientation, collimators can be classified as, i) parallel− ii) converging− iii) diverging− and iv) pin-hole collimators [3] as shown in Figure 1.2.

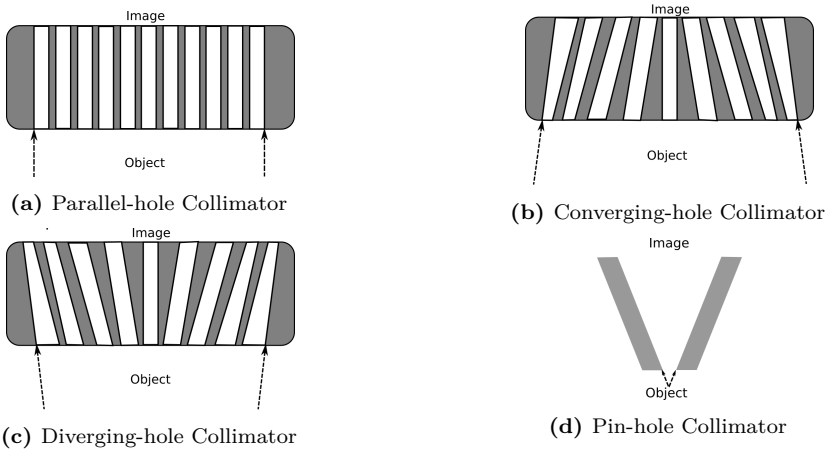

(a) Parallel-hole Collimator

(b) Converging-hole Collimator

(c) Diverging-hole Collimator

(d) Pin-hole Collimator

Figure 1.2: Collimator classification based on hole orientation as, (a) parallel- (b) converging- (c) diverging- and (d) pin-hole collimator.

It is evident from Figure 1.2 that converging-, diverging and pin-hole collimators

have similar basic design with the only difference in hole orientation (i.e. converging hole). Therefore, on the basis of design, collimators can be classified as i) parallel-hole and ii) converging-hole collimator [4, 5].

In terms of image reconstruction and filtering, converging-hole collimator pose more challenges compared with parallel-hole collimators but can result in enhanced sensitivity or detection efficiency for given field of view (FOV) [3–5]. There are other different collimator designs proposed with an intent to enhance sensitivity in SPECT that are mainly in research and not in widespread clinical use. Important examples of such collimators include i) rotating slat collimators, ii) multisegment slant-hole collimators and iii) multipinhole collimators. The description of these collimators is beyond the scope of this work and details and relevant references can be found elsewhere in (e.g. [4, 6]).

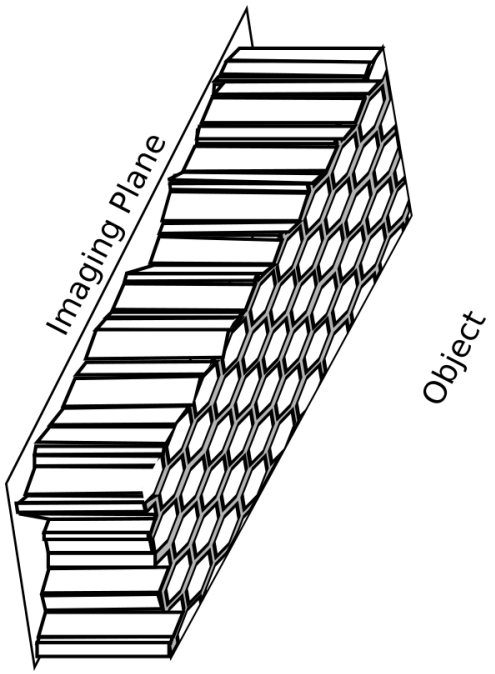

Figure 1.3: Parallel-hole collimator with hexagonal holes in hexagonal array.

This work mainly focuses on parallel-hole collimators specifically, with hexagonal holes in a hexagonal array (Figure 1.3). Parallel-hole collimators can be specified completely by lattice structure of hole pattern and three parameters that include i) septal thickness (T), ii) hole separation and iii) the hole size (l). In the case of hexagonal hole collimators, hole size is given as side length of the hole and is related to face-face distance ($f2f$) as $f2f = \sqrt{3}l$. Parallel-hole collimators with hexagonal

holes in a hexagonal array are the most commonly used collimator design in clinical settings [3, 5].

1.2.2 Detector System

In SPECT imaging, regardless of the way the detection system is designed, the main objective of the system is to convert γ-ray energy into a measurable electrical signal. The number of information-carriers created by gamma-ray interactions in the detector (e. g. visible light photons in case of inorganic scintillators) is the ultimate limiting factor in detector system performance [7]. The relatively high density (ρ=3.67 g/cm^3) and atomic number (Z=53), high photon yield of about 3.3 $\times$ 10^{-2} photons/eV makes NaI(Tl) an excellent candidate for γ- and x-rays detection in the 50-250 keV energy range [3]. These crystals are also transparent to their own light. These physical properties and the fact that it can be grown into relatively large and nearly defect-free plates, have made NaI(Tl) the detector of choice for general purpose gamma cameras [3, 7].

The photomultipliers are an integral part of scintillator based gamma cameras that convert scintillator output (in form of visible photons) into measurable electrical signal. Almost all of the currently available general purpose gamma camera systems use of vacuum tubes, known as photomultiplier tube (PMT). The PMT produces a current pulse when activated by a weak light signal (schematic shown in Figure 1.4). The internal surface of the entrance window (the photocathode) is coated with a photo-emissive material that emits electrons when visible light photons interact with it. The typical value of quantum efficiency for a photocathode, defined as number of electrons emitted per photon absorbed, is 10-30% [3, 8].

The electrons emitted by the photocathode are then accelerated through an array of metal plates, known as dynodes, with increasing potential. The internal surface of each dynode is coated with material having high secondary emission. These electrons get accelerated towards the end of the tube and get amplified to large pulse of current due to the emission of secondary electrons at each dynode step. The overall gain, A, with n number of dynode steps, having amplification factor δ per step, can be given as in Equation 1.1 [8].

$$A = \alpha\delta^n \tag{1.1}$$

where α is the fraction of photo-electrons collected by the first dynode step. A gamma

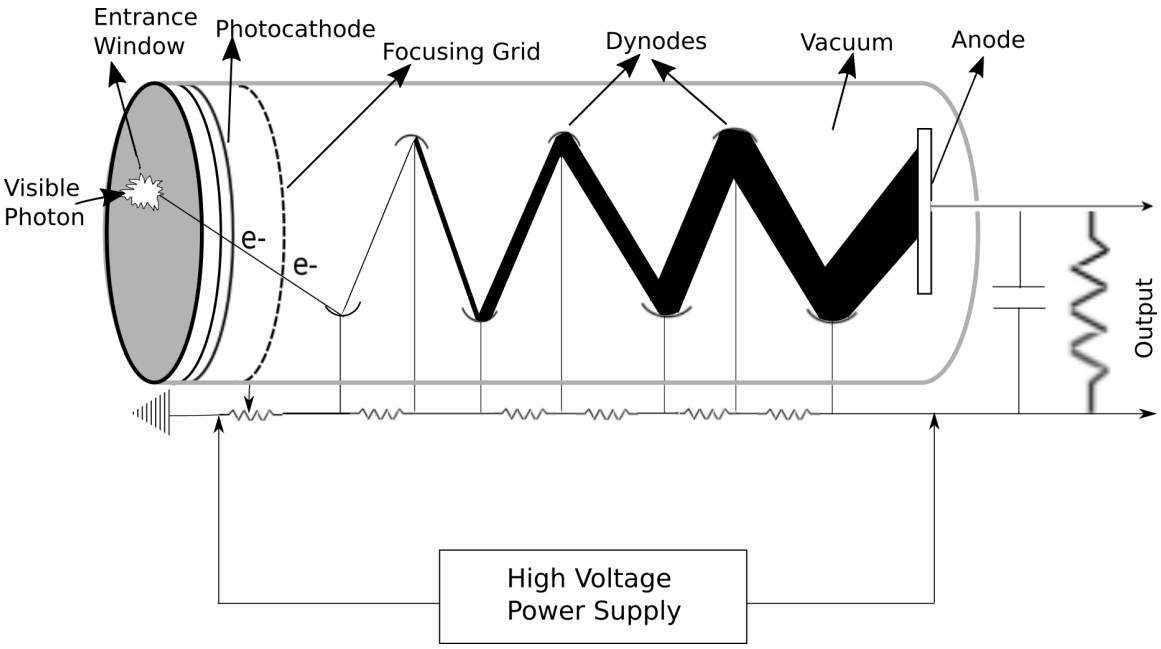

Figure 1.4: Schematic of photomultiplier tube (PMT).

camera usually has an array of these PMT tubes. Despite their widespread use, NaI(Tl)-PMT based gamma camera have following disadvantages.

- Due to its hygroscopic nature, NaI(Tl) usually requires an aluminum cover to avoid moisture from reaching and damaging the crystal. These crystals can easily be cracked through mechanical and thermal stress that might not make the crystal unusable but raise the opacity of the crystal to its own light [3].
- The most commonly used photomultiplier tubes (PMTs) with their associated electronics, make the system relatively bulky and large and that the whole system needed to be magnetically shielded.
- NaI(Tl)-PMT based system have relatively limited energy resolution ($\approx 10\%$).

These shortcomings and an urge to develop a better nuclear medicine imaging system are the key factors that have lead scientific and engineering communities to keep looking for better system in terms of spatial and energy resolution, sensitivity and size. There are currently two areas are of interest in this regard, 1) semiconductor based photomultiplier arrays and 2) Room temperature semiconductor detectors.

A Silicon photomultiplier (SiPM) consists of an array of avalanche photodiodes working in Geiger mode. The details on working and development of SiPMs can be

found in [8]. While, as an important area of research in SPECT imaging, use of SiPM as photomultipliers not only offer the ability to make a SPECT system relatively more compact but, also make the system suitable to work in large magnetic fields. The SiPM based hybrid PET/MRI systems are now commercially available but, a hybrid SPECT/MRI system is yet to become commercially available. However, the efforts to build one are in progress [9, 10].

Cadmium Telluride (CdTe) and the Cadmium Zinc Telluride (CZT) based semiconductor detectors offer direct transfer of deposited gamma ray energy into measurable electric signal with no need of photomultipliers. Their higher atomic number (Cd (Z= 48) and Te (Z=52)) compared to Silicon (Z=14) and Ge (Z=32) and ability to work at room temperature have made these detector suitable to use for emission tomography. These detectors offer higher carrier output with about 31,000 electron-hole pairs for each 140 keV ^{99m}Tc photon compared to 1000 photocathode electrons in NaI(Tl)-PMT detector system [8, 11]. They also offer better energy (about 5% compared to about 10% for NaI(Tl)-PMT) and spatial resolution due to much larger number of information carriers and ability to acquire images with much smaller pixel sizes (about 0.5 mm $\times$ 0.5 mm $\times$ 0.5 mm) respectively [7, 11]. A more detailed description on development and working of these detectors can be found in [7, 8, 11].

1.2.3 Gamma Camera Designs

Different gamma camera designs for general and/or dedicated use are standard imaging devices in nuclear medicine imaging clinics worldwide [3]. On the basis of design and usability, gamma cameras can be divided into three broad categories, namely i) General purpose, ii) Dedicated and iii) Multimodality or hybrid systems.

General purpose single and dual-head gamma cameras are the work-horses of most SPECT facilities. The working principle and construction of these NaI(Tl)-PMT based systems have been described previously in Section 1.2. Theoretically, more heads imply higher sensitivity and reduced imaging time. Reduced imaging time in turn means enhanced patient comfort and reduced patient motion related image artifacts. At the time of this writing, almost all the SPECT systems sold commercially are dual-head gamma cameras.

As discussed at the end of Section 1.2.2, a desire to develop nuclear medicine imaging systems with high resolution and with smaller footprints especially, in the new imaging locales, have raised the interest in CdT and CZT based solid state systems.

Recent developments in solid state detector design and image formation schemes or collimation, and the importance of nuclear cardiology have lead to commercial CZT-based **dedicated cardiac scanners** [11, 12]. A couple of such systems, one from Spectrum Dynamics Inc. (D-SPECT®) and other from General Electric Systems Inc. (Discovery NM 530c®), are shown in Figures 1.5(a) and 1.5(b) respectively. D-SPECT® uses nine pixelated CZT detectors spanning over L-shaped 90^o geometry (Figure 1.5(a)) with each detector fitted with parallel square-hole tungsten collimator. This camera can perform cardiac acquisition from sitting to supine position without any detector or patient-couch motion [12]. The camera is focused over left precordium (i.e. the region or the thorax immediately in front of the heart) using a scout scan. On the other hand, Discovery NM 530c®, camera employees 19 pixilated CZT detectors in a similar L-shaped geometry (Figure 1.5(b) with each detector having its own tungsten pinhole collimator [12]. A detailed description on anatomy and physiology (literally) of these systems can be found in [12].

(a) D-SPECT® camera (Spectrum Dynamics Inc.)

(b) Discovery NM 530c® (General Electric Medical Systems Inc.)

(c) Discovery NM 750b® (General Electric Medical Systems Inc.)

Figure 1.5: Cadmium Zinc Telluride (CZT) based solid state nuclear cardiology scanners (a) D-SPECT® from Spectrum Dynamics Inc. (Image downloaded from `http://www.spectrum-dynamics.com` on August 17, 2016) and (b) Discovery NM 530c® by General Electric Systems Inc. (Image downloaded from `http://www3.gehealthcare.ca` on August 17, 2016). A CZT based dedicated dual head molecular breast imaging (MBI) system (c) Discovery NM 750b® by General Electric Systems Inc. (Image downloaded from `http://www3.gehealthcare.ca` on August 17, 2016).

A dedicated dual-head scintimammography scanner known as, molecular breast imaging (MBI) system (Discovery NM 750b® by General Electric Systems Inc.) composed of CZT detectors has been reported to have superior sensitivity for lesions as small as 3 mm (Figure 1.5(c)) [13].

Despite its superior sensitivity and ability to measure concentrations in nanomolar

to picomolar range, nuclear medicine imaging suffers from the problem of poor spatial resolution. Poor resolution compared to modalities like CT or MRI has earned nuclear medicine the nickname, "unclear medicine" [14, 15]. As an attempt to transform to "clearer medicine" and recent interest in multimodality imaging has resulted in development of hybrid SPECT/CT and SPECT/MRI systems. Virtually all the PET systems and an increasing number of SPECT systems are integrated with x-ray CT scanners [16]. **Hybrid SPECT/CT** scanners provides co-registered SPECT and CT

Figure 1.6: Infinia Hawkeye 4® by General Electric Systems Inc. (Image downloaded from `http://www3.gehealthcare.ca` on August 17, 2016).

images that offer following advantages compared to conventional SPECT systems [17, 18]:

- Co-registered CT-based images provide anatomical reference to interpret poorly resolved SPECT images when placed side by side or analyzed in fused form.
- CT images can be used for attenuation correction of SPECT images (described later in Section 1.5.2).
- CT image information can also be incorporated into an iterative reconstruction algorithm as a prior for SPECT to correct for partial volume effect (PVE) in SPECT images (as discussed later in Section 1.5.1).

An example of SPECT/CT system is shown in Figure 1.6. It is important to describe here that the experimental studies presented in this thesis were performed on one such system (GE Infinia Hawkeye® General Electric Systems Inc.) at our department. For consistency, a similar system was also modeled in all the simulation studies performed in this work.

1.3 Image Reconstruction

The data acquired using the gamma camera at a given projection angle gives a two dimensional projection of three dimensional activity distribution. Each projection represents the ray sum, line integral or Radon transform of an object at detector position represented by a vector (s, θ). In this case, the projection (i.e. Radon transform) of 2D activity distribution $f(x, y)$ with no attenuation can be given by Equation 1.2 and is depicted in Figure 1.7 for an object with two hot disk sources within cold background.

$$p(s, \theta) = \int_{-\infty}^{\infty} \int_{-\infty}^{\infty} f(x, y)\delta(\mathbf{x} \cdot \boldsymbol{\theta} - s)dxdy \tag{1.2}$$

where $\mathbf{x} = (x, y)$ and $\boldsymbol{\theta} = (cos\theta, sin\theta)$.

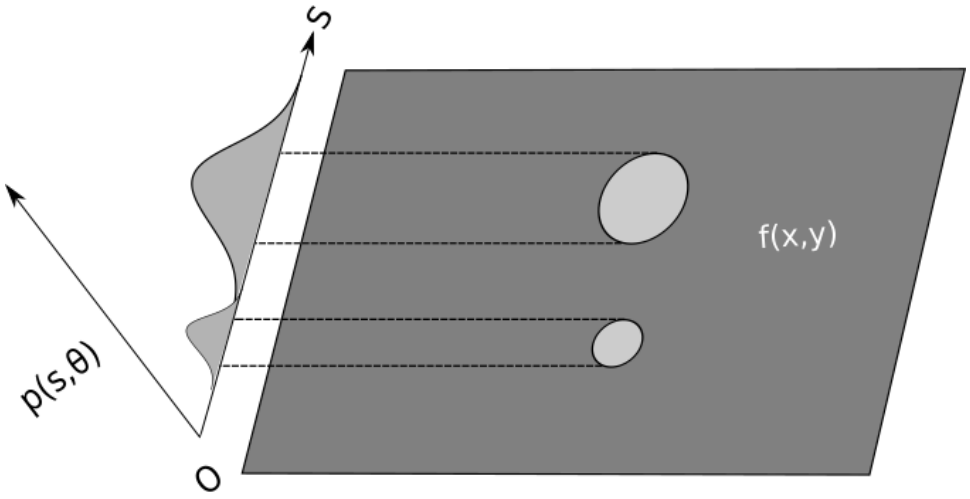

Figure 1.7: Projection view at an angle θ for an object $f(x, y)$ with two disk sources in cold background.

A two dimensional projection has no depth information, but in many cases it can still be diagnostically useful. For example, a whole body bone scan image provides

enough information as there is no tracer uptake in tissue lying above and below the skeletal system. More commonly, however, in a SPECT acquisition data has to be acquired at number of angles in step and shoot mode. These projections help in estimating the 3D-activity distribution using image reconstruction methods.

The reconstruction methods can broadly be categorized as, i) analytical and ii) iterative reconstruction methods.

1.3.1 Analytical Reconstruction Methods

At the heart of all the analytical reconstruction methods is the Fourier central slice theorem that states, the 1−D Fourier transform $P(\omega, \theta)$ of the parallel projection data represents the 2−D Fourier transform, $F(\omega_x, \omega_y)$ of object distribution $f(x, y)$ (see Appendix A.1 for derivation). This implies that inverse Fourier transform of a complete 2−D noise-free projection set of 3−D activity distribution, should yield the original activity distribution. However, this is not the case, backprojection results in a blurry image due to scaling by a factor of $1/|\omega|$ in frequency domain (see Appendix A.2 for details). This scaling in frequency domain can be represented as convolution of the original distribution with blurring function $1/r$ (where r being the distance from the center of point source location [19]. In mathematical form the blurry image obtained through backprojection, $f^{'}(x, y)$, can be written as Equation 1.3.

$$f^{'}(x, y) = f(x, y) * \frac{1}{r} \tag{1.3}$$

Therefore, it is important to remember here that the backprojection does not represent exact inverse of projection operation and in linear algebra it is often referred as conjugate transpose [19]. In order to recover the exact activity distribution, noise-free projection data has to be filtered using $|\omega|$ (i.e. ramp filter) in frequency domain. This filtering of projection data gives rise to one of the most commonly used analytical reconstruction methods known as, filtered backprojection (FBP). In this method the projection data is convolved with suitable filter in the spatial domain and then backprojected. In order to avoid the convolution step in spatial domain, the Fourier transform of projection data is used as convolution that implies a simple scaling in frequency domain.

As described earlier, a high-pass ramp filter is required for reconstruction of noise-free data. In case of noisy data, application of the ramp filter often results in the

enhancement of high frequency noise (i.e. graininess) in the image. Therefore, in order to achieve a balance between suppression of high and low-frequencies the ramp filter is often replaced with a band-bass filter. Finally, an inverse Fourier transform of the filtered data is taken to obtain the final image. The detail description of FBP and other analytical image reconstruction algorithms and band-pass filters can be found in [19, 20].

1.3.2 Iterative Reconstruction Methods

Filtered back projection (FBP) is a one-step process that leads to inaccuracies as inclusion of more complex effects like the collimator-detector response or scatter is not straight forward. In order to avoid the inaccuracy problem associated with Radon model based reconstruction, modern iterative reconstruction algorithms can be used. These algorithms describe the imaging problem as a system of linear equations and perform reconstruction by minimizing an objective function (e.g. likelihood function). It should be noted that in order to achieve accuracy, efficiency has to be sacrificed to some extent as iterative algorithms are much more computation intensive compared to FBP.

We can consider reconstruction of SPECT data as a **linear inverse problem** and can represent projection data at a given angle as in Equation 1.4.

$$\mathbf{Hf} = \mathbf{p} \tag{1.4}$$

Where, $\mathbf{H}$ is the system matrix which maps a 3D activity distribution $\mathbf{f}$, to projection space to form a projection $\mathbf{p}$.

In 2D, the system matrix $\mathbf{H}$, is generally a rectangular matrix and able to represent effects such as attenuation and any other blurring mechanism. Each element h_{ij} of the system matrix $\mathbf{H}$, can be thought to represent the mean contribution of each pixel j to each data bin i. The linear model can take into account different effects such as, attenuation, detector response and scatter by considering the contribution from many pixels into one imaging bin. Comparatively, Radon transform approach models only the contribution from pixels along the line of response (LOR) into an imaging bin. The system matrix is generally a large sized rectangular matrix that is difficult or impossible to invert. However, a generalized inverse may be found using least-square minimization and/or singular value decomposition method [19].

There are number of iterative reconstruction techniques being used for emission tomographic reconstruction, but maximum likelihood expectation (MLEM) and its variations are the most used iterative algorithms. MLEM was first demonstrated for use in SPECT in 1984 [21, 22]. Figure 1.8 shows a flow diagram of an iterative image reconstruction algorithm in general.

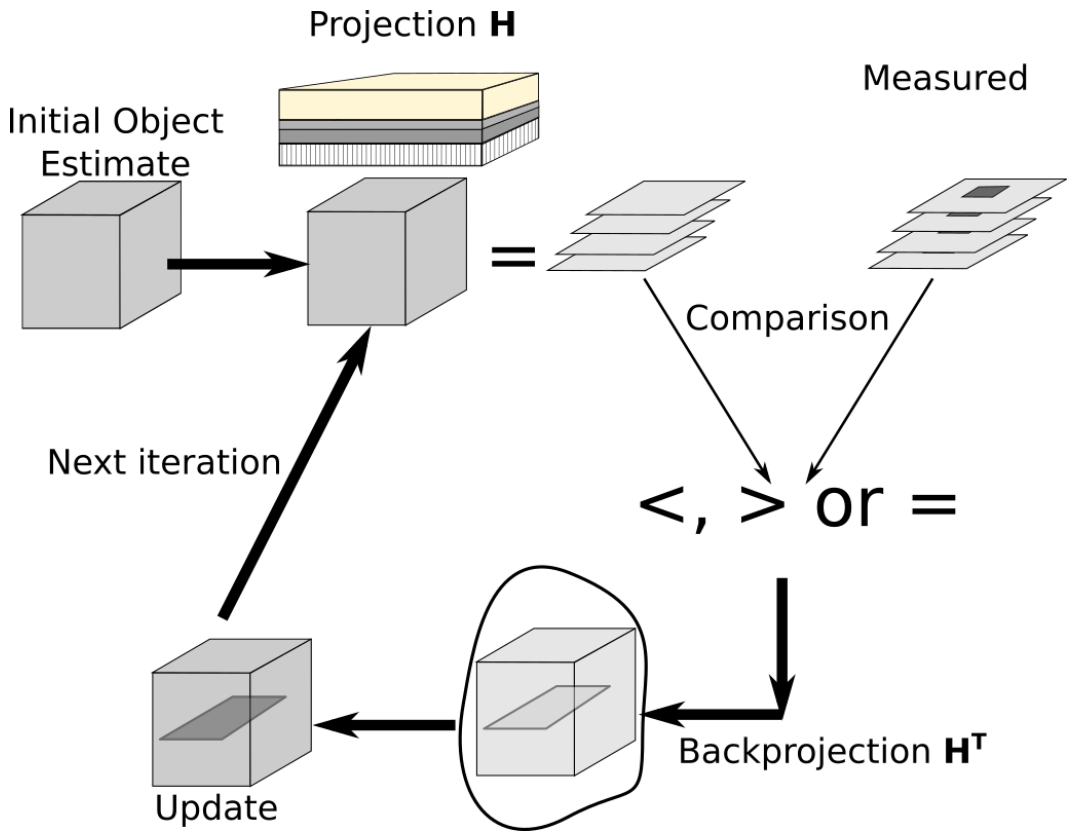

Figure 1.8: Flow diagram of an iterative reconstruction algorithm in general.

1.3.2.1 Maximum Likelihood Expectation Maximization (MLEM)

The MLEM algorithm is based on the fact that the emission of photon within a certain time interval from a radioactive source can be described by a Poisson distribution. The detailed derivation of this algorithm can be found in reference [21]. MLEM for SPECT can be expressed as Equation 1.5.

$$f_j^{new} = \frac{f_j^{old}}{\sum_i H_{ij}^T} \sum_i H_{ij}^T \frac{p_i}{\sum_j H_{ij} f_j^{old}} \tag{1.5}$$

The flow of MLEM is similar to the one shown in Figure 1.8 with comparison step performed as ratio between measured data and corresponding projections of the current estimate. Backprojection of these ratios determine the update factor for the current estimated f_j^{old} to get the new estimate f_j^{new}.

There are two main shortcomings of MLEM, i) The convergence of the algorithm is very slow. An acceptable solution may require many hundreds of iterations. ii) After many iterations MLEM algorithm tries to fit the noise present in the measured data thereby, degrading the reconstructed image quality. Therefore, the reconstruction has to be interrupted before too much image degradation occurs. The selection of the stopping point is usually subjective and based on user's experience.

1.3.2.2 Ordered Subset Expectation Maximization (OSEM)

As discussed earlier, convergence of MLEM is slow due to the fact that the update of the current object estimate is performed after going through the whole set of projection data. One way to accelerate the reconstruction is to increase the number of updates per iteration. This can be done by a method proposed by Hudson and Larkin [23], known as ordered subset expectation maximization (OSEM). In this algorithm projection data is divided into a number of sets known as ordered subsets and the current estimate is updated to get a new estimate after going through each of the subset.

$$f_j^{new} = \frac{f_j^{old}}{\sum_{a \epsilon s} H_a^T} \sum_{a \epsilon s} H_a^T \frac{p_i}{\sum_{a \epsilon s} H_a f_j^{old}} \tag{1.6}$$

where, s represents a ordered subset of the projection data. It is important to note that, despite of all the similarities of OSEM with MLEM, it is quite different from MLEM as, it has no proof of convergence for the data with noise. In OSEM, the speed of convergence can be increased by increasing the number of subsets, by making the subsets size small. However, the cost of improved speed is the increased noise level for the same level of bias compared to MLEM [24]. In OSEM acceleration of about 8-10 time can be achieved with very little increase in noise levels. Members of an ordered subset usually chosen at maximum possible angular displacement. One such example is shown in Figure 1.9.

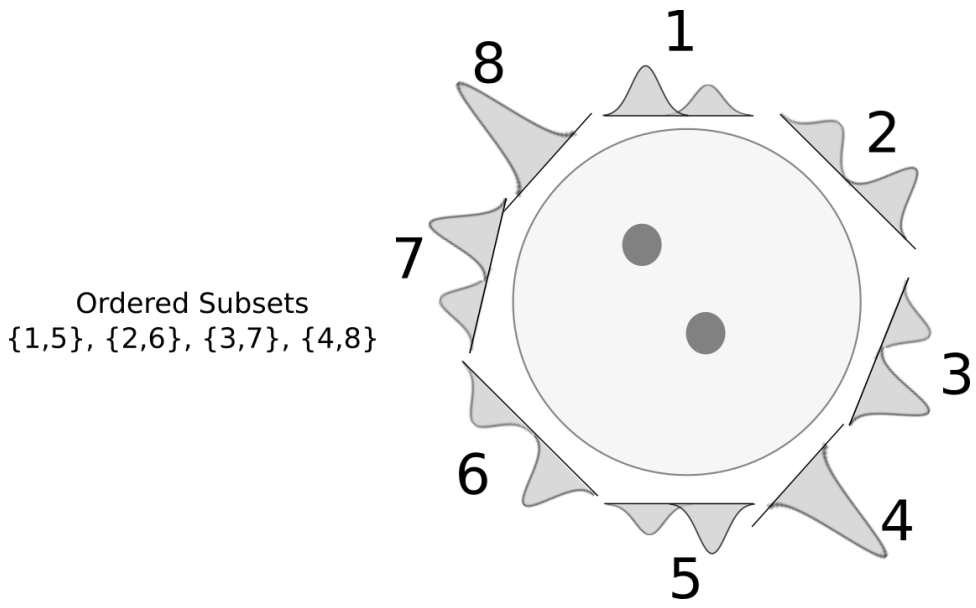

Figure 1.9: Projection data consisted of 8 projections divided into 4 ordered subsets.

1.3.2.3 Green's One-step -late (OSL) Algorithm

As described previously, MLEM estimates tend to become noisy as the number of iterations increases. Therefore, improvements in criterion could be made on two aspects, a) achieve a better match between estimated and measured data and b) comparatively less noise in the reconstructed images. The regularization using *a prior* knowledge can help to achieve a) and b). Hence, the goal of this Bayesian reconstruction algorithm is to achieve maximization with penalization to achieve a) and b). This kind of maximization leads to Green's one-step-late (OSL) algorithm (Equation 1.7).

$$f_j^{new} = \frac{f_j^{old}}{\sum_i H_{ij}^T + \beta \frac{\partial}{\partial f_j} V(f_j^{old})} \sum_i H_{ij}^T \frac{p_i}{\sum_j H_{ij} f_j^{old}} \tag{1.7}$$

here the prior term $\beta(\partial/\partial f_j)V(f_j^{old})$, involves the derivative of an energy function V (to enforce smoothing) and weighting factor β to modulate the importance of prior. One way to avoid possible negative values in the denominator due introduction of prior term in MLEM is to choose a low prior weight β.

1.4 Monte Carlo Methods for SPECT Simulation

The idea of Monte Carlo (MC) simulation was conceived by Stanislaw Ulam in 1946 [25] that he further developed in collaboration with another Manhattan project colleague John V. Neumann [26]. Instead of solving complex differential equations and integrals, these methods utilize random numbers and probability density/distribution functions to generate results. The term Monte Carlo originated from a popular gambling place known as Monte Carlo in Monaco. This is because probability (i.e. measurement of chance) is closely related to random nature of these activities. The probability functions and cross sections for photon/electron transport related physical processes have been so accurately formulated that MC simulations can conveniently be used to obtain results that are very close to reality. This has made MC a very important research and clinical tool in emission tomography [27, 28].

One of the major advantages of MC technique is that they allow study and measurement of parameters that are very difficult or impossible to measure in practical situations. For example, the contribution and composition of scatter detected under the photopeak energy window in a SPECT acquisition can only be calculated or estimated accurately using these techniques. In MC methods different factors/parameters (e.g scatter or attenuation) can be turned on and off to study the effect of these factors/parameters on image quality or to create a reference image. These methods also allow optimization and testing of novel equipment designs and effect of different parts and parameter on the system design (e.g. crystal thickness, collimator hole shape and dimensions and/or phantom size etc.) without performing a costly practical design and manufacturing exercise.

A major limitation of these methods is that the results of these methods are as accurate as the implementation of physical model in the computer. Therefore, one important question to ask while using these methods is whether all the factors that can affect the results have been included in the model. Even though MC techniques offer endless opportunities in terms of testing a conceptual equipment design or a new imaging technique or protocol, the long calculation times (often several hours to days) has hampered the widespread use of theses techniques in clinical settings (e.g. for image reconstruction). The main reason for this inherently long simulation time is the low detection efficiency in SPECT. In a SPECT simulation, only 1 out of about 10,000 emitted photons are able to reach the detector (i.e a probability of 10^{-4}) [27, 28].

1.4.1 Variance Reduction Techniques

In order to improve the ratio of detected events to the actual number of photon emissions, methods known as **variance reduction techniques** (VRTs) are employed. These techniques involve modification of probability function(s) to improve that ratio. The biasing introduced by modified probability function(s) is countered by changing the weight of the simulated particle using a simple rule given in Equation 1.8.

$$w_o p_o(x) = w_m p_m(x) \tag{1.8}$$

where w and $p(x)$ denote weight and probability function for a variable x respectively. Correspondingly subscript o and m stand for original and modified. For example, in a SPECT simulation each detected photon would mean addition of one event in detector bin that is a weight, $w_o = 1$. Now, if we modify the emission probability function by simulating photons in only one hemisphere under the condition that there is no scattering media or probability of scattering is very low in the other hemisphere. This would make sense only if we now change the photon weight, w_m, to 0.5.

One of the most efficient VRTs used in a gamma camera simulation is called as **forced detection (FD)**. In this method, either angular or spatial probability distribution function is modified to increase the number of detected events (Figure 1.10(a)). At each interaction site a copy of photon is forced towards detection system within limited arc (i.e. angular with $0 \leq \theta \leq \theta_{max}$ and $0 \leq \phi \leq 2\pi$) or limited range of photon path length (i.e. spatial with $0 \leq l_{path} \leq l_{max}$) [27].

The weight of each of the forced copy is also modified based on the probability of scattering and reaching the detector system at sampled polar and azimuthal angles or path-length. While, FD significantly reduces the simulation time, the time frame still remains too long to be used in clinical settings [29].

Another VRT that has been extensively validated and used in this work is known as **convolution-based forced detection (CFD)** that is very similar to FD. The CFD is different from FD only in two aspects. i) the convolution of detection probability with distance dependent collimator response function (Gaussian) and ii) forcing the photons only along the paths perpendicular to the collimator as shown in Figure 1.10(b). It has been shown that the detector response (represented as the distance dependent point spread function, PSF) of collimator can be approximately modeled as a Gaussian as

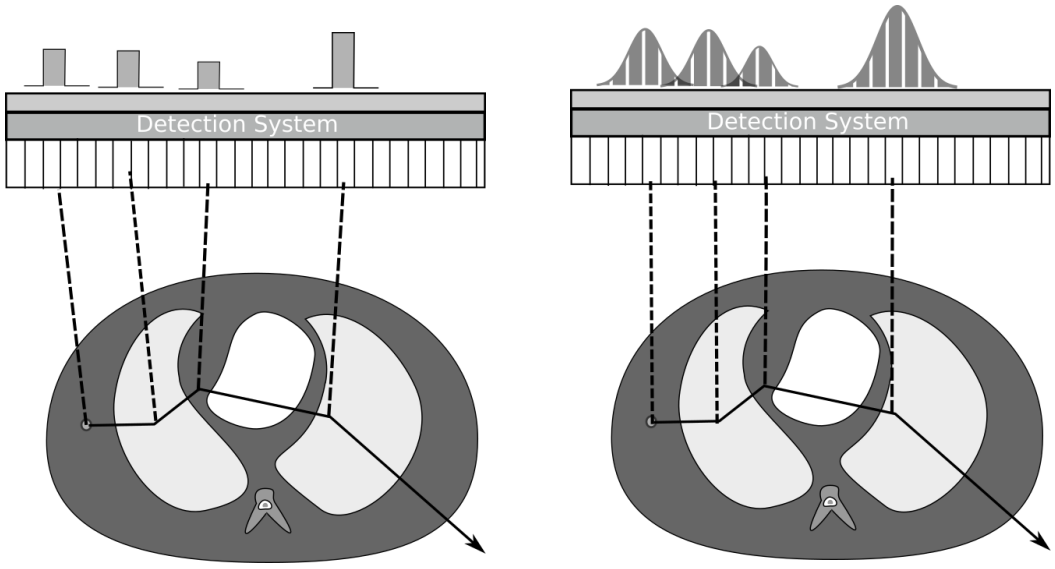

(a) Forced Detection **(b)** Convolution-based Forced Detection

Figure 1.10: Schematic of (a) forced detection and (b) convolution-based forced detection with solid and dashed lines representing actual and forced paths in both the cases respectively. The corresponding modeled responses shown above the detection system of gamma camera.

given in Equation 1.9.

$$PSF(x,y,z) = \frac{1}{2\sigma_x(z)\sigma_y(z)}.e^{-\frac{1}{2}\left(\frac{x-x_o}{\sigma_x(z)}\right)^2-\left(\frac{y-y_o}{\sigma_y(z)}\right)^2} \tag{1.9}$$

where(x_o, y_o) is the center pixel where photons are detected on the collimator face. $\sigma_x(z)$ and $\sigma_y(z)$ are standard deviation or spread in $x-$ and $y-$direction respectively. The standard deviation can easily be derived from spatial resolution (FWHM) of Gaussian response function (discussed latter in Sections 2.1.1 and 3.1.1) using Equation 1.10.

$$\sigma = \frac{FWHM}{2\sqrt{2ln2}} \tag{1.10}$$

In general, Compton scattering and photoelectric effect are the main modes of photon interaction in SPECT. In this case the sum of probabilities for Compton scattering and photoelectric effect can be considered as unity and the relative probability of Compton scattering can be determined approximately as $(1 - P_{photo}(E))$, where $P_{photo}(E)$ is probability of photon of energy E to undergo photoelectric effect. The probability of photon detected by a detector at an angle, α using CFD can be evaluated using

Equation 1.11 [29].

$$P(\alpha) = w_i \times (1 - P_{photo}(E)) \times KN(\phi) \times e^{-\int_0^{l_{fd}} \mu(E)\, dl} \tag{1.11}$$

where,
w_i = Photon history weight initially set at 1.
$1 - P_{photo}(E)$ = Probability that photon is not absorbed by photoelectric effect (approximately equal to probability of Compton scattering).
$KN(\phi)$ = Klein-Nishina cross-section based probability for a photon to scatter at an azimuthal angle ϕ.
$e^{-\int_0^{l_{fd}} \mu(E)\, dl}$ = Photon attenuation factor due to forced path length of l_{fd}.

In this work convolution based force detection (CFD), is being used to accelerate the Monte Carlo photon transport modeling in SIMIND MC program.

1.4.2 Monte Carlo Codes

With regards to SPECT, available MC codes can be divided into two broad categories, i) general purpose and ii) dedicated. Table 1.2 provides a list of some well known general purpose MC codes. It is important to note here that simulation studies involving nuclear medicine imaging system with generalized codes often require extensive programming skills. In order to address this issue some research groups have developed the MC codes based on one of the codes, described in Table 1.2, as a core layer. These codes provide developers with the opportunity to construct application specific modules in a hierarchical layer architecture [30]. Sim-SPECT based on MCNP and GATE based on GEANT-4 are the examples of such codes.

There are three types of dedicated MC software packages used in nuclear imaging simulations namely, SPECT dedicated MC, PET dedicated MC (not discussed here), and MC used in both. Table 1.3 provides a brief description of some dedicated MC codes used in SPECT imaging.

The choice of MC code is generally made, based on the type of imaging application, user's programming abilities and ease of use. In fact, one of the major motivations behind the development of dedicated MC codes, is to build user-friendly interface that requires minimal level of programming skills. This ease of use may be the reason behind the popularity of these codes in nuclear medicine imaging simulation studies [25].

Table 1.2: A brief description of the available general purpose Monte Carlo Codes used in Nuclear Medicine Imaging.

Code	Brief Description
EGS [31]	Simulates coupled photon/electron transport in any material or geometry defined by the user. The nuclear medicine imaging simulations require extensive programming skills in MORTRAN as specific modeling is not included in the code
ETRAN [32]	Ability to simulate coupled photon/electron transport but, with limited geometry options. ETRAN is available as a part of MCNP and ITS due to its capabilities to investigate a specific interaction.
ITS [33]	Nuclear medicine imaging system simulations require extensive programming skills in FORTRAN. The code is capable of coupled electron/photon transport simulation in any material in slabs, cylinders or combinatorials.
MCNP [34]	Coupled neutrons/photons/electrons transport in any material through user-defined generalized geometry. Simulation of nuclear imaging systems not specifically included and requires an extensive amount of user manipulation of input date files to model complex geometries.
FLUKA [35]	The code is capable to simulates coupled photons/electrons transport in any material through combinatorial geometry. Simulation of nuclear imaging systems not specifically included and requires an extensive amount of user programming in C/C++.
GEANT-4 [36]	Coupled photons/electrons transport in any material through combinatorial geometry. Simulation of nuclear imaging systems not specifically included and requires an extensive amount of user programming in C/C++.

1.5 Image Degradation Factors in SPECT

SPECT imaging has always been regarded as highly sensitive modality with limited quantitative accuracy and relatively poor image quality. The image quality and quantitative accuracy are affected by physical factors like, i) spatial resolution or partial volume effects, ii) loss of photons due to photoelectric absorption and scatter within patient's body (i.e. attenuation), iii) contamination of detected photons due to scattered photons either emitted from patient's body or scattered in collimator and remain available for detection. Therefore, correction of these factors is necessary for obtaining a better image quality and improved quantification [37, 38].

Table 1.3: A brief description of some of the available dedicated Monte Carlo Codes used in SPECT Imaging.

Code	Brief Description
SIMIND [39]	Dedicated for SPECT. Simulates photon through transport shape- or voxel-based phantom. A user module written in FORTRAN could be linked.
SIMSET [40]	Dedicated for SPECT or PET simulations written in C. Ability to simulate photon transport in any material through voxelized phantoms.
MCMATV [41]	Ability to perform SPECT simulations. The code is written in FORTRAN and can simulate photon transport in voxelized phantom.

1.5.1 Partial Volume Effects

In SPECT imaging, it is possible to quantify a 3D activity distribution within a patient. However, relatively poor resolution in SPECT (remember the moniker,"unclear medicine") limits the accuracy of quantification. These effects are often called as, partial volume effects (PVE). In order to elaborate on PVE, a simple simulation exercise using a uniform ^{99m}Tc sheet source (40 cm $\times$ 20 cm) as shown in Figure 1.11(b) within non-radioactive water-bath (250 cm $\times$ 250 cm $\times$ 250 cm) was performed. SIMIND Monte Carlo program was used to perform the simulation with setup depicted in Figure 1.11(a). In this study all other effects except collimator response modeling were turned off. From Figure 1.11(a), it can be seen that two representative photons A and B emitted within the sensitive volume defined by spatial resolution of the instrument (shown as a gray triangular region) will be detected at a given detector bin. That is any emission within the sensitive region will generate similar response on the detector in this case. This loss of location information within sensitive volume region results in a loss of high frequency information (i.e. edges and boundaries) in the resulting image as shown in Figure 1.11(c).

Another type of PVE is the sampling effect related to the voxel size in the image (usually several mm^3). This PVE results in inability to resolve sub-voxel structures in the final image. Additional PVE may also be caused by cardiac, respiratory or patient motion. Motion-correction is itself is a large area of research [42] but, beyond the scope of this work.

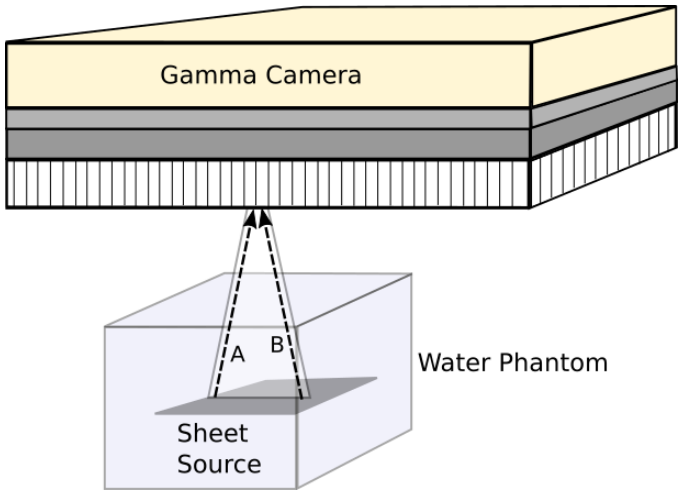

(a) Partial volume effect

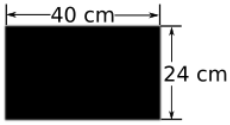

(b) Simulated rectangular sheet source

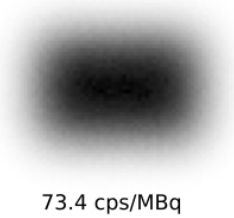

(c) PVE only

Figure 1.11: Partial Volume Effect (PVE): photons A and B, depicted in (a), emitted within the sensitive region defined by spatial resolution of gamma camera from (b) rectangular source will be detected in a given detector bin. This loss of location information within the sensitive region caused an overall loss of edges and boundary (i.e. high frequency information) in the image as shown in (c).

The partial volume correction (PVC) methods can broadly be divided into three possible categories as, i) image enhancement (during or post reconstruction) with resolution modeling and/or anatomical priors, ii) image domain-based and iii) projection domain-based PVC methods [43].

The image enhancement based PVC methods rely on resolution recovery using emission data and/or anatomical information to perform PVC. One such method that performs PVC during reconstruction using higher resolution MRI imaging data has been developed by Bowsher et.al. [44]. This algorithm promotes smoothing among nearby voxels that have similar MRI signal. This method has been recently used in cardiac SPECT using CT-based anatomical prior within Green's one-step-late algorithm to suppress noise in the image [45]. One major advantage of using this method is that it does not require any image segmentation. The post-reconstruction PVC methods involves deconvolution using point spread function (e.g. [46]) or applying

high frequency information using blurred version of MRI or CT-based co-registered image (e.g. [47]).

Shcherbinin and Celler [48] have presented a template based PVC. This method iteratively corrects for PVE using correction factors generated through forward projection, reconstruction and smoothing of CT-based binary template and activity values in initial image reconstructed without PVC in image domain.

In projection-domain the PVE can be corrected either using recovery coefficients obtained through segmentation and reconstruction of region of interest (ROI) (e.g. [49]) or by using anatomical based PVC method described above (e.g. [50]). It is important to note here that anatomical based methods in projection domain also require segmentation [43]. A brief description of PVC methods in emission tomography and related references can be found in [43].

1.5.2 Attenuation

Figure 1.12(a) depicts the loss of photons due to either photoelectric absorption in the phantom (photon C) or Compton scattering (photon B) away from the gamma camera that is attenuation. For this purpose, a simulation setup similar to the one shown in Figure 1.11(a) was used to see the effect of inclusion of attenuation on the image of a rectangular sheet source (Figure 1.12(b)). It is evident from Figure 1.12(c) that attenuation increases the noise in the image by significantly reducing the number of detected events (reduction of about 84% compared to the image in Figure 1.11(c)).

Considerable effort has been made to develop methods that perform attenuation compensation in either i) image domain or ii) during analytical or iterative reconstruction.

The Chang algorithm [51], once the most commonly used attenuation correction method clinically [37, 38], is used to perform post-filtered backprojection reconstruction attenuation correction. In this method an attenuation correction factor (ACF) averaged over number of projections (Equation 1.12) is used to perform attenuation compensation on image reconstructed using FBP [38].

$$ACF = \left(M^{-1} \sum_{i=1}^{M} e^{-\mu s_i} \right)^{-1} \tag{1.12}$$

Where M^{-1} is the number of projections and s_i is the distance from the object center plane and the projection plane. A number of solutions for attenuated (i.e.

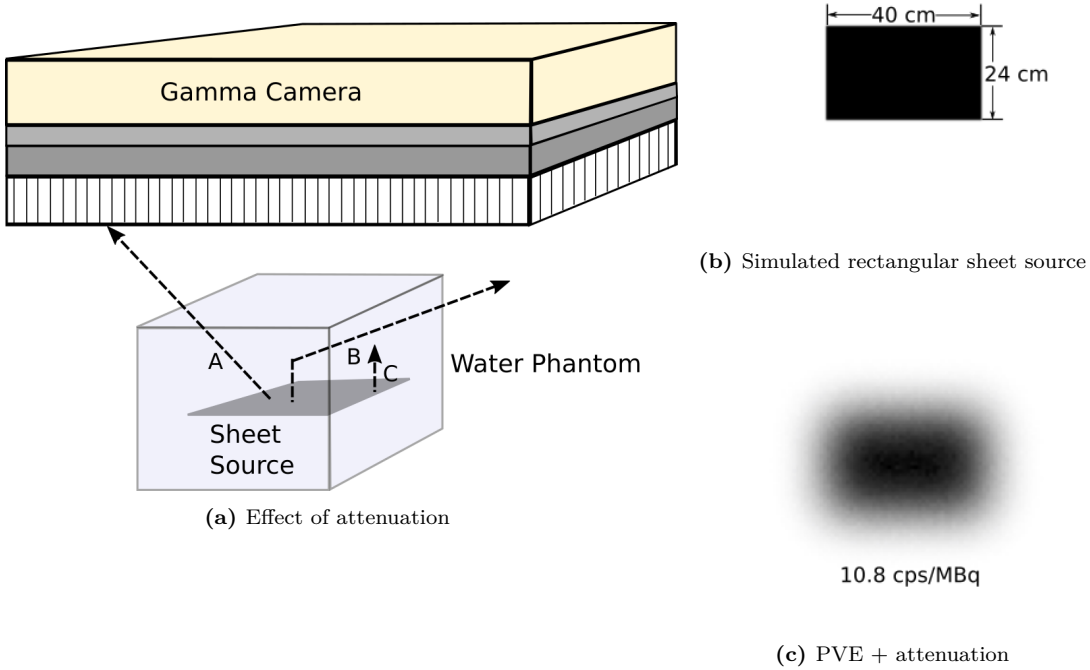

(a) Effect of attenuation

(b) Simulated rectangular sheet source

(c) PVE + attenuation

Figure 1.12: Attenuation: photons A, B and C are lost due to attenuation as depicted in (a) after emission from (b) rectangular source. The loss of photon results in significant reduction in number of detected events in the image as shown in (c).

exponential) Radon transform have been proposed. However, these solutions do not work for non-uniform attenuators and have poor noise properties [37].

Analytical solution of attenuated Radon transform in case of non uniform attenuation has also been proposed. Description of these FBP based attenuation correction method is beyond the scope of this work and can be found in [37].

Among many advantages of iterative reconstruction methods is the flexibility to involve attenuation and scatter modeling into transition system matrix [37, 52]. Accurate determination of the attenuation map is critical in performing attenuation correction using iterative image reconstruction methods. The methods used to calculate the attenuation map can broadly be divided into two categories i) transmission-less and ii) transmission-based methods. Transmission-less methods involve attenuation map calculations using emission data. One such method has been developed for cardiac perfusion imaging. In this method, patient is re-imaged after delayed imaging using ^{99m}Tc with macroaggregated albumin (MAA) to manually segment out lungs and

body contours to calculate the attenuation map [53, 54]. In order to avoid additional ^{99m}Tc-MAA injection and patient re-imaging, the scatter energy window in addition to the photopeak energy window (PEW) is acquired to segment the body contour and lung in emission data respectively. Inability of this approximative method to calculate attenuation maps for all the patients has made this method of limited clinical use [55]. Iterative approach to solve for both attenuation and emission maps from emission data has also been proposed [56, 57]. Transmission based attenuation map determination methods involve either the use of registration and segmentation of computed tomography (CT) or magnetic resonance imaging (MRI) images [37, 38] or the use of a gamma camera with different source and collimator configurations to calculate the attenuation map [37, 38, 52]. Even though suffering from emission data crosstalk contamination, the use of line source scanning across the field of view (FOV) with narrow energy window is dominant attenuation map calculation configuration in currently available SPECT scanners [37]. With the availability of hybrid SPECT/CT systems, CT based attenuation map determination is now becoming a standard clinical protocol [38]. However, comparatively much shorter CT data acquisition times and the presence of metal implants or CT contrast agents may affect the accuracy of these attenuation maps [37, 38].

1.5.3 Scatter

Due to the limited energy resolution of the most commonly used NaI(Tl) detector (≈10%) in gamma camera, significant image degradation is caused by the scattered photons detected under PEW [37]. A simulation study using the rectangular sheet source (Figure 1.13(b)) described for PVE and attenuation in Sections 1.5.1 and 1.5.2 respectively was repeated to see the effect of inclusion of scatter on the image. Figure 1.13(a) depicts the image degradation caused by erroneous detection of photons A and B due to scattering away from their respective points of origin. It is clear from Figure 1.13(c) that cause image degradation by erroneous positioning of detected events. Some of such regions are indicated using circles on Figure 1.13(c).

The methods to correct for scatter detected under PEW can be categorized as, i) energy spectrum based methods, ii) scatter distribution based scatter estimation and correction and iii) reconstruction based scatter correction methods [37, 38, 58].

Scatter compensation in projection or image domain can be performed either by subtraction of a scatter estimate or restoration through deconvolution of an approximate

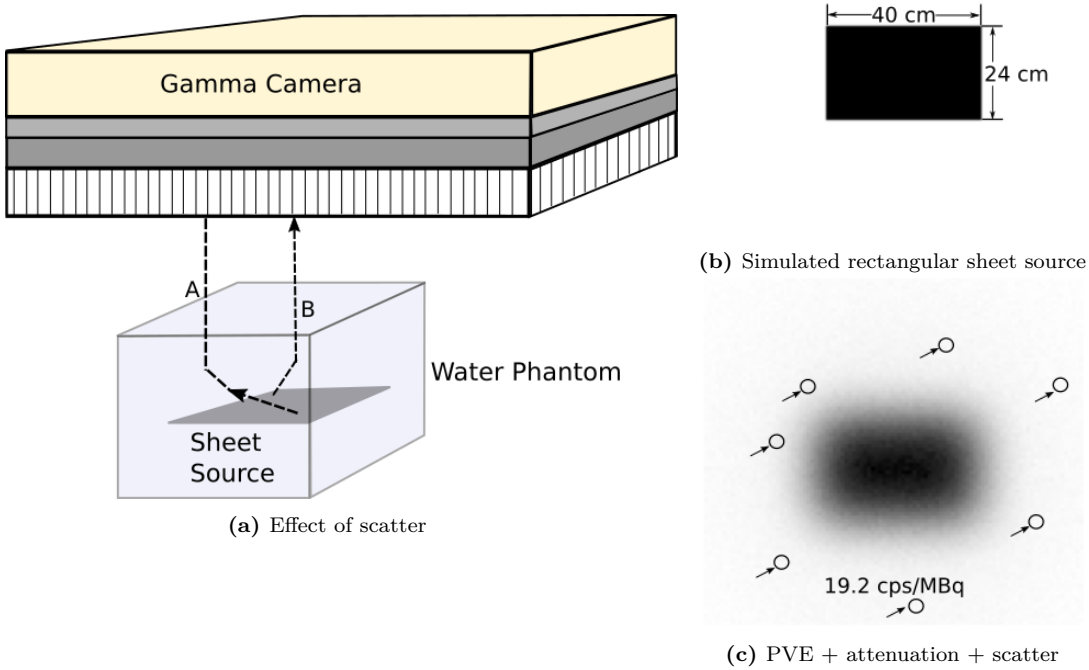

(a) Effect of scatter

(b) Simulated rectangular sheet source

(c) PVE + attenuation + scatter

Figure 1.13: Scatter: inclusion of scatter photons A and B in (a) caused these photons to be detected at erroneous position after emission from the (b) sheet source and resulted in a more image degradation as depicted in (c).

spatial scatter distribution function.

The energy-distribution based methods involve scatter estimation in a pixel and subsequent subtraction from PEW data generally require acquisition of additional energy windows (e.g. [59–62]). The triple energy window (TEW) scatter compensation method is an example of subtraction based scatter compensation methods [60, 61]. TEW based compensation uses two narrow energy windows adjacent to each of the PEWs in order to determine crosstalk contribution within each of the PEWs. In order to get scatter $S_{i,j}$ contribution in ith PEW for jth pixel Equation 5.1 can be used.

$$S_{i,j} = \left(\frac{C_{il,j}}{W_{il}} + \frac{C_{iu,j}}{W_{iu}}\right) \frac{W_{il} + W_{iu}}{2} \tag{1.13}$$

where, W_{il} and W_{iu} are window widths for scatter windows below and above the ith PEW respectively, and $C_{il,j}$ and $C_{iu,j}$ are the total number of counts collected in jth pixel of corresponding scatter windows respectively. The method is not only

performs scatter compensation for a single isotope, but has also been used to correct for downscatter between the two isotopes in simultaneous dual-isotope SPECT. One such example of TEW based correction is simultaneous ^{99m}Tc/^{111}In SPECT is shown in Figure 1.14 with PEWs and scatter/crosstalk windows. It should be noted that W_{3u}=0 and hence $C_{3u,j}$=0 for 245 keV PEW that implies dual-energy window correction in this case. Among many other energy window based scatter correction techniques only

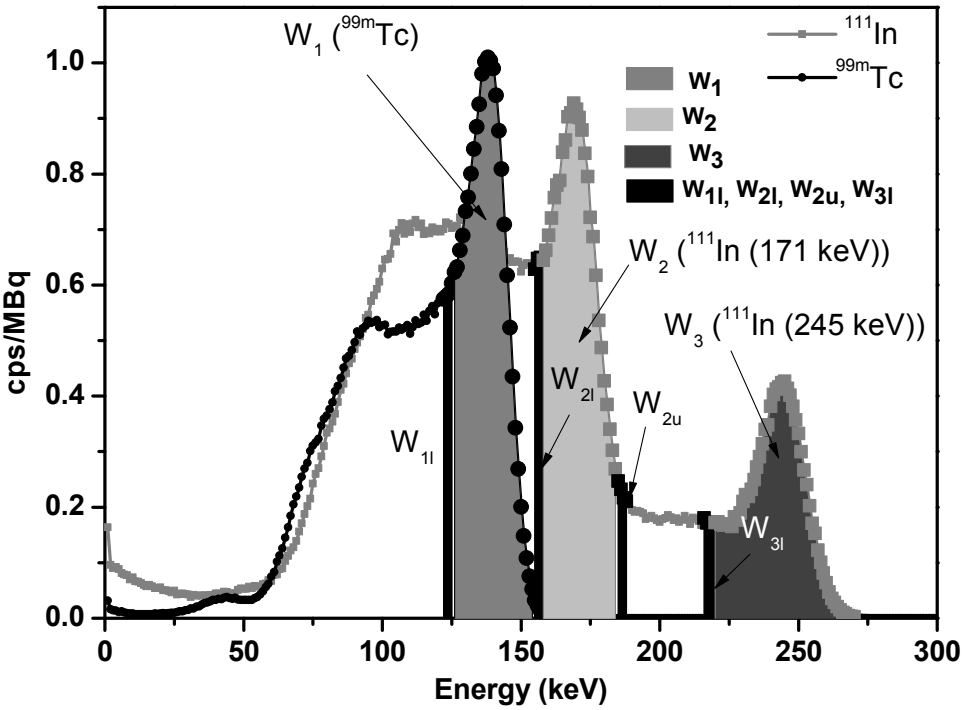

Figure 1.14: ^{99m}Tc/^{111}In spectrum with windows used for TEW based scatter and crosstalk correction of projection data.

TEW and dual energy window based scatter correction method withstood the test of time [58]. The energy window based scatter correction methods have the advantage of being simple, speedy and easy to implement [37, 58]. Undesired noise amplification and approximative (i.e. not exact) scatter estimation are the disadvantages that may be associated with these methods [37, 58].

More recent spectral distribution based scatter correction methods involve spectral fitting [63] factor analysis (e.g. [64, 65]) and artificial neural network (e.g. [64, 66, 67]). These methods promise to provide accurate scatter compensation but, require either list mode or multiple-energy windows based (often $\geq$10) acquisition [37, 58, 68]. List mode data and required multiple energy window acquisition facilities are currently not

available on most of the SPECT imaging systems [37, 58].

Modeling of the scatter in PEW by some scatter function based on either line source measurements [69, 70] or individualized patient based transmission point spread function (PSF) through an attenuation map [71, 72] form the basis of convolution-subtraction method. This method is an example of spatial scatter distribution based methods. Rather than using a stationary scatter distribution based estimate, methods other than Monte Carlo (MC), have been developed to incorporate a non-stationary scatter estimate into iterative reconstruction algorithms (e.g. [73–76]). In these methods transport through a non-homogeneous tissue is approximated by water-equivalent depths represented by slabs. Effective scatter source estimation (ESSE) method is an example of one such method, refined for Compton scatter based attenuation correction [74, 77, 78].

The methods that involve inclusion of scatter model into the system matrix can be categorized as reconstruction based scatter correction methods (RBSC) e. g. [79, 80].

Compared to other approximative methods for scatter estimation, MC methods are expected to provide quite accurate estimation of scatter but, individualized patient-based scatter estimation has always been considered computationally too demanding to be practical. Especially, if it is to be incorporated into iterative reconstruction algorithm [58]. The problem with these notoriously slow MC methods is there inherent low detection efficiency in SPECT simulation studies [27]. In order to address this issue a variance reduction technique (VRT), known as convolution forced detection (CFD) [81], has previously been incorporated into SIMIND Monte Carlo Program by our group with [29] and without [82] detailed collimator scatter and septal penetration modeling. CFD implementation generates low-noise projections often within a minute of acquisition time [29, 81]. In this VRT a weighted copy of photon at each interaction site is forced in direction that is perpendicular to the gamma camera head while convolving it with distance-dependent collimator response kernal modeled as Gaussian [29, 81]. The CFD-based accelerated MC forward projector has been successfully incorporated into iterative reconstruction framework to correct for scatter and crosstalk between the isotopes in simultaneous dual-isotope SPECT [83–86].

1.6 About This Work

This thesis work is written in sandwich form. Most of the basic concepts and ideas related to the main work have been presented in this chapter (**Chapter 1**).

Chapter 2 presents a comparative study between convolution-based forced detection implemented in SIMIND Monte Carlo program (CFD-SIMIND) and GEANT-4 based simulation toolkit GATE. This work was based on an intent to perform an exhaustive comparison between (or validation of) CFD-SIMIND and (using) an independent gold standard Monte Carlo program like GATE, as such comparison has never been reported. This work has been accepted for publication **IEEE Transactions on Nuclear Science**.

The study presented in **Chapter 3** of this work has been published in **5th issue of Volume 62 (2015) of IEEE Transactions on Nuclear Science**. The title of the work is, "Simultaneous ^{99m}Tc/^{111}In SPECT Reconstruction using Accelerated Convolution-based Forced Detection Monte Carlo". As the title suggests, this work focuses on Simultaneous ^{99m}Tc/^{111}In SPECT reconstruction using CFD-SIMIND as forward projector to compensate for crosstalk, scatter and attenuation in the corresponding images of ^{99m}Tc and ^{111}In.

The work presented in **Chapter 4** is based on a simulated application of simultaneous ^{99m}Tc/^{123}I SPECT in breast imaging and reconstruction of simulation data using CFD-SIMIND. This work, titled, "Accelerated Monte Carlo based Simultaneous ^{99m}Tc/^{123}I SPECT Reconstruction" has already been published in **Proceedings of 2012 IEEE Imaging Conference**.

Chapter 5 is based on a recent submission to **IEEE Transactions on Nuclear Science**. This study is based on the use of accelerated CFD-SIMIND MC and CT-based anatomical prior to take care of the quantification and PVE respectively. This work incorporates CFD-SIMIND as a forward projector and CT-based Bowher's prior in Green's one-step-late algorithm to improve quantification.

Finally, the conclusion and some recommendations for future work are presented in **Chapter 6** of this work.

Chapter 2

A Comparison between GATE and Accelerated Convolution-based Forced Detection SIMIND for Low- and Medium-energy Collimators: A Simulation Study

Accepted for publication in IEEE Transactions on Nuclear Science©, 2016

MONTE CARLO (MC) based photon transport modeling is commonly used for simulation studies in emission tomography [25, 28, 87, 88] and is often regarded as the gold-standard for photon modeling methods. One of the most precise and accurate methods, GATE, was born out of high energy physics code (GEANT4) and was initially developed for emission and transmission tomography simulations in 2004 [89], but has since been extended to optical imaging and radiation therapy. GATE is now a well established MC tool and extensively used in simulation studies in nuclear medicine.

Assie *et al*, [90], validated GATE against experimental point and line source data for ^{99m}Tc with a LEHR collimator, ^{99m}Tc with a MEGP collimator, and ^{111}In with a MEGP collimator in both air and water. The comparison for ^{99m}Tc and ^{111}In was performed using different dual head gamma cameras for each isotope. A comparison between

experimental and GATE simulation data was performed using spatial resolution, count sensitivity and the measured energy spectra. The study showed that GATE simulation results that are very similar to those obtained from experimental data with spatial resolution measurements within 0.1 mm and sensitivity values within 4−5%. In a subsequent study the accuracy of GATE was compared with experimental data for ^{111}In SPECT and indicated an overall difference of 2% and 4% in spatial resolution and sensitivity respectively for line source simulations on a GE DST-XLi camera [91]. This also showed that the GATE SPECT simulation of a cylindrical phantom with spheres and bony inserts closely reproduced experimental results. It is important to mention here that both these studies were performed with the first version of GATE and that additional improvements in geometrical design and physics implementation have been made since.

While MC has some potential clinical applications (e.g. model based single and simultaneous dual-isotope SPECT image reconstruction [85, 86, 92–94]), conventional MC methods are too slow to implement in clinically useful times. As a result, our group has previously implemented a number of different variance reduction techniques (VRT's) using the SIMIND MC code to make it feasible to use in reduced time frames. These VRT's include convolution forced detection (CFD) [95], multiple projection sampling [29] and accelerated collimator penetration modeling [82]. We have shown very good agreement between our simulation methods and experimental data for simple phantoms, but a systematic study of the accuracy of our approach to other MC programs has not previously been performed.

The current study focuses on a comparison between our CFD-accelerated SIMIND MC program (CFD-SIMIND) and a well established GEANT4 based Monte Carlo code, GATE (version 7.1). A similar CFD implementation based on the work of [29] has already been incorporated as an option in the standard SIMIND Monte Carlo program. The motivation behind this work stems from previously reported simulation and experimental studies that have shown detailed collimator scatter and septal penetration modeling has negligible impact for medium and low energy isotopes (e.g. [96–98]). Thus, there is a question of whether CFD-SIMIND can be used in place of GATE in certain applications utilizing low to medium energy nuclides with little or no loss of accuracy. CFD-SIMIND does not include detailed collimator scatter and septal penetration modeling, and by doing so, offers significant reductions in simulation times. Also, the use of two or more independent codes is often required for simulation

studies involving single photon emission tomography [99]. Simulation studies involving model-based correction of image degradation factors like scatter and attenuation in single or dual-isotope SPECT during iterative reconstruction process are the examples of such studies (e.g. [86, 93, 100]).

2.1 Methods

2.1.1 Convolution based Forced Detection

In the CFD method, at each photon interaction location, a weighted copy of the interaction photon is forced to undergo a scatter in the direction of the detector. The detection location on the camera is then convolved with an energy and distance dependent collimator response kernel. The detailed description of CFD can be found in [81]. It should be noted that in the current implementation, collimator scatter and septal penetration have not been modeled, although our group has developed a method to model these effects [82] at the expense of longer simulation times. Neglecting these effects, the overall geometric response can be modeled as an energy and depth dependent Gaussian with FWHM ($F(z, E)$) given by Equation 2.1.

$$F(z, E) = \sqrt{F_i(E)^2 + \left(\frac{d(l_e(E) + z)}{l_e(E)}\right)^2} \tag{2.1}$$

where $F_i(E)$ is the energy dependent intrinsic FWHM system resolution, d is the collimator hole diameter, l_e is the effective septal length for a specific photon energy and for a hole length l equivalent to $l_e = l - 2/\mu(E)$ and z is the distance from the detector. Equation 2.1 depicts an overall response in CFD that includes both intrinsic and geometric response of the detector and collimator respectively. Further details on the implementation can be found in [29, 86].

2.1.2 Point Source Simulations

For comparison purposes, a GE Infinia gamma camera (General Electric, USA) with a 9.5 mm thick NaI(Tl) crystal was modeled with both CFD-SIMIND and GATE for all simulation studies. Both Low Energy High Resolution (LEHR) and Medium Energy General Purpose (MEGP) collimators were used to acquire point source data for ^{99m}Tc

(photopeak energy window (PEW) 126-154 keV) and in the case of ^{111}In (PEW 154-188 keV and 221-270 keV) only, a MEGP collimator was modeled. A summary of the simulation setups used in the study is given in Table 2.1.

It is important to mention slight differences in the way photons are detected in GATE and SIMIND. In CFD-SIMIND, forced detection occurs by sending a weighted photon from the point of last interaction in the direction of the detector system [101]. The probability of detection is then determined based on the detector geometry (ie, thickness and material composition) and the photon detection weight is altered according to the detection probability. The overall spatial resolution is then modeled as an energy dependent Gaussian kernel with FWHM, $F(z, E)$, given by Equation 2.1. The intrinsic spatial resolution, F_i of the detector in Equation 2.1 is based on a fixed value at 140 keV and varies as $1/\sqrt{E}$ [39, 101]. We have used the value $F_i = 4.8$ mm as measured on the GE Infinia camera with 9.5 mm crystal.

In GATE, the detector material is treated as any other object material and photon interactions are modeled in this material [91]. Each detected event in GATE is placed at the centroid of all the interaction points in the crystal weighted by the ratio of deposited energy to the total energy deposited in the crystal [91, 102]. GATE uses a fixed intrinsic spatial resolution value (ie, $F_i = 4.8$ mm in this study) to model Gaussian blurring kernel at each interaction location within the detector unless optical photon simulation is enabled [102, 103]. The use of this option, while increasing realism, greatly adds to the simulation time and hence, is not usually performed when not investigating optical photon transit [103]. For both methods, we have made no attempt to improve the intrinsic detection model as we feel this aspect is relatively minor component compared to geometric (ie, collimator) response and object scatter.

Table 2.1: Summary of point source simulation setups.

Isotope	**Energy (keV)**	**Collimator**	**Photopeak Energy Window (PEW)**
^{99m}Tc	140	LEHR, MEGP	126-154 keV
^{111}In	171, 245	MEGP	154-188 keV
			221-270 keV

A comparison is performed, in terms of detection sensitivity and spatial resolution for point source simulations in air. For point source simulation studies in water, the comparison between GATE and CFD-SIMIND was based on image profiles and energy

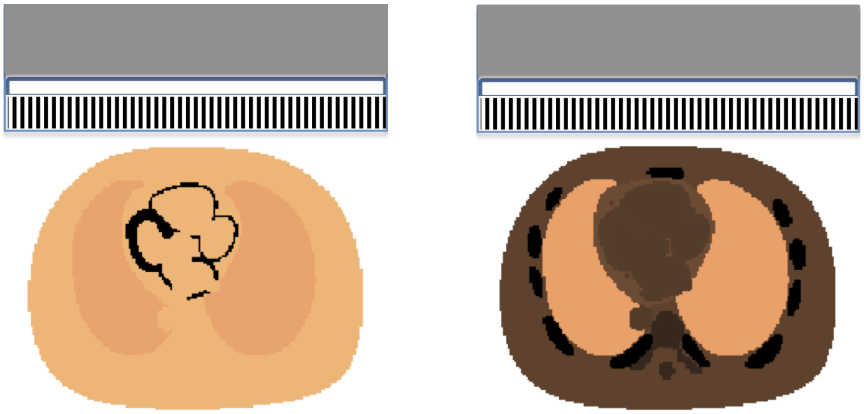

(a) (b)

Figure 2.1: XCAT Phantom simulation setup showing camera head position with respect to (a) activity map and (b) electron density map respectively.

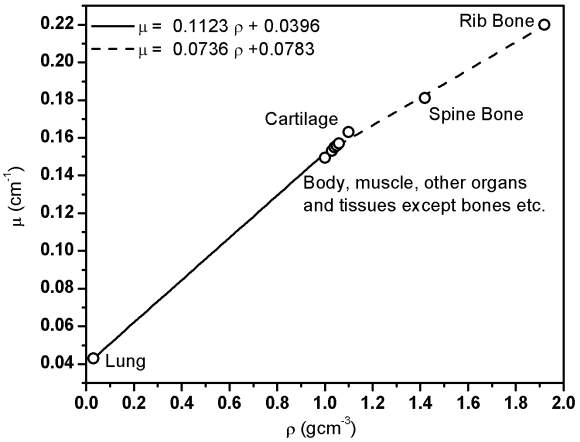

Figure 2.2: Attenuation coefficient, μ (cm^{-1}) versus density, ρ (gcm^{-3}) for different organs and tissues used for CFD-SIMIND simulation setup of XCAT Phantom.

spectra obtained through both the MC codes. An image profile based comparison was performed along the central lines on logarithmic and linear scales and Universal Image Quality Index (Q_{UI}) values for all the source depths in water [104]. This metric can be described by Equation 2.2.

$$Q_{UI} = \frac{4\bar{g}\bar{s}\left(\sum_{i=1}^{N} g_i s_i - N\bar{g}\bar{s}\right)}{(\bar{g}^2 + \bar{s}^2)\left(\sum_{i=1}^{N}(g_i^2 + s_i^2) - N(\bar{g}^2 + \bar{s}^2)\right)} \tag{2.2}$$

where $\bar{g}$ and $\bar{s}$ are the mean pixel content of images g and s, with each having N pixels

respectively. With $Q_{UI} \epsilon [-1, 1]$, a value of $Q_{UI} = 1$ indicates a perfect match that is $g = s$. We have chosen this metric as it has shown to outperform mean square error (MSE) under different image distortion conditions [104, 105].

It is pertinent to mention here that all the simulation studies presented in this work use only projection data with no corrections, filtering or reconstruction algorithm applied for comparison between CFD-SIMIND and GATE.

For the case of CFD-SIMIND, low-noise images, totaling $2.5{\times}10^8$ photon histories were simulated, whereas GATE simulated a 40 minute acquisition of a 10 MBq point source, thereby approximating low-noise projection data in all the cases.

2.1.3 XCAT Phantom Simulation

Simulation setups similar to the point source data acquisition (described in Section 2.1.2 and Table 2.1) were used to obtain low-noise projection data for an extended source distribution and non-uniform attenuation map of the 4D extended cardiac torso (XCAT) phantom [106]. XCAT phantom with grid size of $256 \times 256 \times 256$ (voxel size of $2.21 \times 2.21 \times 2.21$ mm^3) was used for the simulations with activity concentration ratios of 1:2:10 between the background, the lungs and the myocardium respectively. Figure 2.1 depicts the camera and phantom position used in the XCAT phantom simulation.

For the case of CFD-SIMIND, about 3.9×10^{10} photon histories were simulated for all the isotope/collimator combinations described in Table 2.1 for the XCAT simulation, whereas for GATE, corresponding PEW projections consisted of about 4.2, 4.3 and 6.9 million counts in the case of ^{99m}Tc with LEHR collimator, ^{99m}Tc with MEGP collimator and ^{111}In with MEGP collimator, respectively. For ^{111}In, both the photopeak windows (i.e. 171 keV and 245 keV respectively) were summed together to provide 6.9 million counts, thus representing low noise data in all the cases. It is important to mention here that the XCAT code provides the attenuation map in units of cm^{-1} and in order to convert to density as needed for CFD-SIMIND simulations, a conversion using two distinct linear regions with inflection point at 1.0 gcm^{-3} (Figure 2.2) is necessary. The conversion factors between attenuation coefficient and tissue density are shown in Figure 2.2. For the GATE simulations, the required density map is created using a range of attenuation coefficients associated with each of the organ tissues from the GATE material database.

A comparison similar to the point source simulation data in water, as described in Section 2.1.2, was performed using the XCAT phantom projection data between image profiles and energy spectrum.

Also, in order to evaluate the applicability of CFD-SIMIND for simultaneous dual-isotope SPECT, an additional down-scatter energy window data was acquired for ^{111}In using both CFD-SIMIND and GATE. The width of the additional window was set equal to the photopeak energy window width used for the ^{99m}Tc study. XCAT projection data obtained using GATE consisted of about 3 million counts. A comparison similar to the one performed for XCAT phantom PEW data, described above, was also carried out for the downscatter projection data (i.e., in the ^{99m}Tc window).

2.1.4 Sheet Source Simulations

Projection data using a uniform rectangular sheet source (40×24 cm^2) of 100 MBq or ^{99m}Tc or ^{111}In was acquired in order to compare the image noise properties (coefficient of variation (CoV) and Q_{UI}) and simulation times between GATE and CFD-SIMIND. Twenty consecutive projections with acquisition time of 30 s were acquired using GATE for all the isotope and collimator combinations. Approximately the same number of source photons were simulated for the corresponding CFD-SIMIND based projections. Acquisition energy windows similar to that used for the XCAT phantom were used for the simulations. A rectangular region of interest (ROI) of size 20×10 cm^2 with relatively uniform count distribution within the central part of the sheet source was used for CoV determination. A comparison of the CoV as a function of number of detected photons and simulation time was then performed. The variation in Q_{UI} as function of number of detected photons was also studied.

2.2 Results

2.2.1 Point Source Simulations in Air

Table 3.1 depicts the sensitivity values at a source to collimator distance of 10 cm for point source of ^{99m}Tc and ^{111}In respectively. Slightly lower sensitivity values are seen for CFD-SIMIND, with percentage difference between CFD-SIMIND and GATE from -3.0 to -4.9%, likely due to the absence of septal penetration and collimator scatter

when using CFD-SIMIND. Sensitivity values for ^{99m}Tc with the MEGP have closer agreement likely due to negligible septal penetration effect in this case.

Table 2.2: Comparison of sensitivity values (cps/MBq) at source to collimator distance of 10 cm for point source in air.

Isotope	**Collimator**	**CFD-SIMIND**	**GATE**	**% Difference**
^{99m}Tc	LEHR	73.8	76.4	-3.4
^{99m}Tc	MEGP	74.0	76.3	-3.0
^{111}In (171 keV)	MEGP	64.4	67.1	-4.0
^{111}In (245 keV)	MEGP	40.6	42.7	-4.9

Figure 2.3 depicts fitted FWHM values in the horizontal and vertical directions for each of the source to collimator distances of CFD-SIMIND as a function of the corresponding values obtained in the GATE simulation. A comparison to the ideal line of unity (shown in the dotted gray line in Figure 2.3) and in terms of correlation coefficient (r) (ranges from 0.9997 to 1.000) is depicted on each of the plots. The comparison shows FWHM values for CFD-SIMIND that are within 0.2 mm of the corresponding values for GATE for both LEHR and MEGP collimators in both the horizontal and vertical directions.

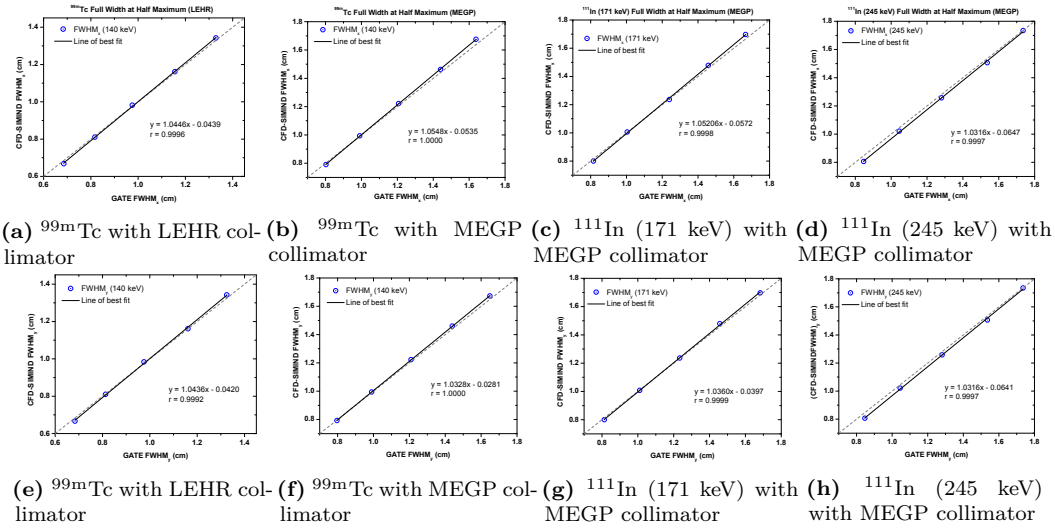

(a) ^{99m}Tc with LEHR collimator **(b)** ^{99m}Tc with MEGP collimator **(c)** ^{111}In (171 keV) with MEGP collimator **(d)** ^{111}In (245 keV) with MEGP collimator

(e) ^{99m}Tc with LEHR collimator **(f)** ^{99m}Tc with MEGP collimator **(g)** ^{111}In (171 keV) with MEGP collimator **(h)** ^{111}In (245 keV) with MEGP collimator

Figure 2.3: Point source in air: Comparison of Full Width Half Maximum (FWHM) values shown in terms of CFD-SIMIND values as a function of GATE based FWHM values obtained at different source to collimator distances (5-25 cm in steps of 5 cm) in both horizontal and vertical directions. The comparison in horizontal direction is shown in (a) for 140 keV with LEHR, (a) for 140 keV with MEGP,(c) for 171 keV and (c) for 245 keV with MEGP collimator respectively whereas, (e), (f), (g) and (h) depict the corresponding comparison in vertical direction respectively.

2.2.2 Point Source Simulations in Water

Figure 3.1 depicts image profiles on both logarithmic and linear scales obtained from representative CFD-SIMIND and GATE point source simulations in water at different depths for i) ^{99m}Tc PEW with a LEHR collimator, ii) ^{99m}Tc PEW with a MEGP collimator and iii) ^{111}In PEW with a MEGP collimator. It should be noted here that ^{111}In data for 171 keV and 245 keV windows have been summed together in accordance with our routine clinical practice. It is evident from Figure 3.1 that the CFD-SIMIND based image profiles match well with corresponding profiles obtained using GATE.

The Q_{UI} values and percent difference in sensitivity obtained between CFD-SIMIND and GATE MC projection data at different depths in water with respect to the collimator surface are given in Table 3.2. Close agreement between the CFD-SIMIND and GATE MC based PEW projections for i) ^{99m}Tc with LEHR (0.986−0.999), ii) ^{99m}Tc with MEGP (0.985−0.997) and iii) ^{111}In with MEGP (0.988−0.996) collimators in terms of Q_{UI} is evident from Table 3.2. The percent difference between the CFD-SIMIND and GATE ranges from -1.8 to -4.9% for all the isotope/collimator combinations.

Figure 2.5 depicts a comparison of energy spectra obtained from CFD-SIMIND

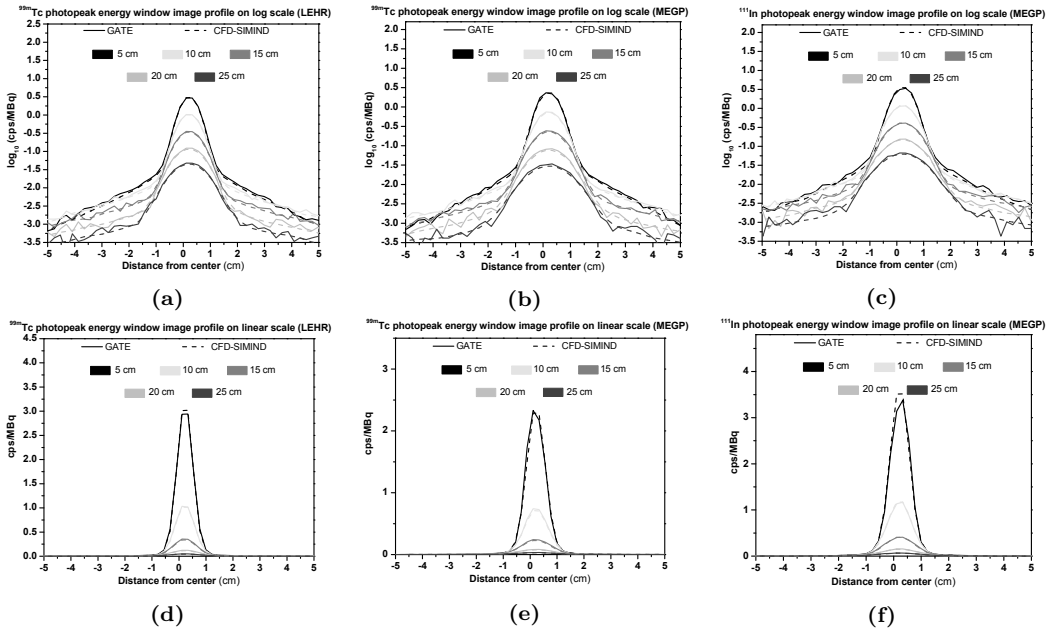

Figure 2.4: Point source in water: Image profiles obtained at different depths in water with GATE MC and CFD-SIMIND base point source simulations for (a) ^{99m}Tc PEW with LEHR collimator, (b) ^{99m}Tc PEW with MEGP collimator and (c) ^{111}In PEW with MEGP collimator on logarithmic scale, whereas corresponding profiles are shown in (d), (e) and (f) on linear scale respectively.

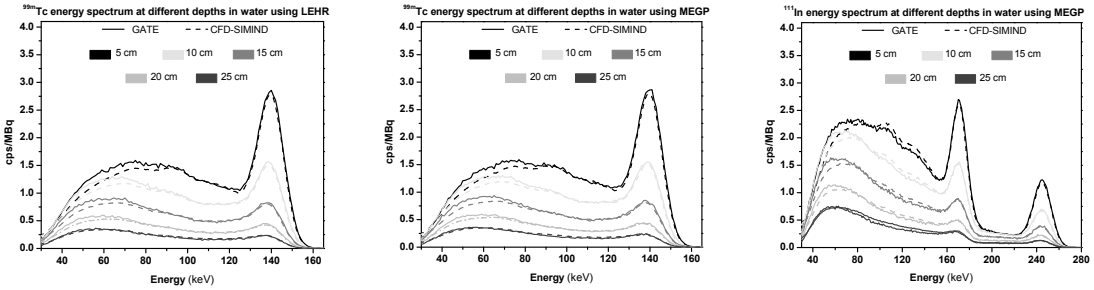

(a) ^{99m}Tc with LEHR collimator **(b)** ^{99m}Tc with MEGP collimator **(c)** ^{111}In with MEGP collimator

Figure 2.5: Point source in water: Comparison between CFD-SIMIND and GATE based energy spectrum at different depths in water in case of (a) ^{99m}Tc with LEHR, (b) ^{99m}Tc with MEGP and (c) ^{111}In with MEGP collimator respectively.

and GATE programs, for the energy range of 30-170 keV for ^{99m}Tc and 30-300 keV for ^{111}In, at different depths in water for all the isotope/collimator combinations used in this study. It is evident from this figure that the spectra obtained using CFD-SIMIND match closely with the corresponding energy spectra obtained from GATE albeit with slightly lower counts per second per MBq for energies below about 80 keV. This is likely due to the absence of collimator scatter in the CFD-SIMIND modeling approach.

A comparison of scatter order as a percentage of total scatter for a source depth of

Table 2.3: Universal image quality index (Q_{UI}) at different depths in water for SIMIND-CFD compared to GATE MC.

	Q_{UI} Value (% Difference in Sensitivity)		
Depth (cm)	**^{99m}Tc with LEHR collimator**	**^{99m}Tc with MEGP collimator**	**^{111}In with MEGP collimator**
5	0.999 (-3.9)	0.997 (-3.2)	0.996 (-2.9)
10	0.999 (-4.2)	0.998 (-3.7)	0.998 (-2.7)
15	0.996 (-4.7)	0.996 (-4.3)	0.997 (-2.4)
20	0.993 (-4.9)	0.992 (-4.4)	0.994 (-1.8)
25	0.986 (-4.9)	0.985 (-4.5)	0.988 (-2.2)

Table 2.4: Composition of scatter in photopeak energy window data for different isotope and collimator combinations.

		Percentage of total scatter under PEW					
Order of scatter		**1**	**2**	**3**	**4**	**5**	**>5**
Acquisition	**Code**						
^{99m}Tc with LEHR collimator	GATE	75.38	20.93	3.30	0.35	0.04	0.00
	CFD-SIMIND	72.79	22.42	4.18	0.55	0.06	0.00
^{99m}Tc with MEGP collimator	GATE	75.03	21.22	3.36	0.36	0.03	0.00
	CFD-SIMIND	73.07	22.30	4.05	0.52	0.06	0.00
^{111}In (171 keV) with MEGP collimator	GATE	50.87	31.11	13.30	3.81	0.78	0.13
	CFD-SIMIND	49.57	30.88	14.24	4.16	0.95	0.20
^{111}In (245 keV) with MEGP collimator	GATE	84.83	13.93	1.17	0.07	0.00	0.00
	CFD-SIMIND	84.37	14.32	1.23	0.08	0.00	0.00

15 cm is given in Table 2.4. For each scatter order, the contribution is very consistent between CFD-SIMIND and GATE, thus suggesting that CFD-SIMIND provides very similar interaction modeling to GATE.

2.2.3 Comparison using XCAT Phantom

Figures 2.6 and 2.7 show projections and corresponding image profiles (Figure 2.6(c) and 2.7(c)) for ^{99m}Tc with i) LEHR and ii) MEGP collimator respectively, along the lines depicted in the corresponding projections for GATE and CFD-SIMIND of the XCAT phantom. The corresponding projections obtained through CFD-SIMIND and GATE show very good agreement with respective Q_{UI} values of 0.988 for both ^{99m}Tc with LEHR and ^{99m}Tc with MEGP collimator.

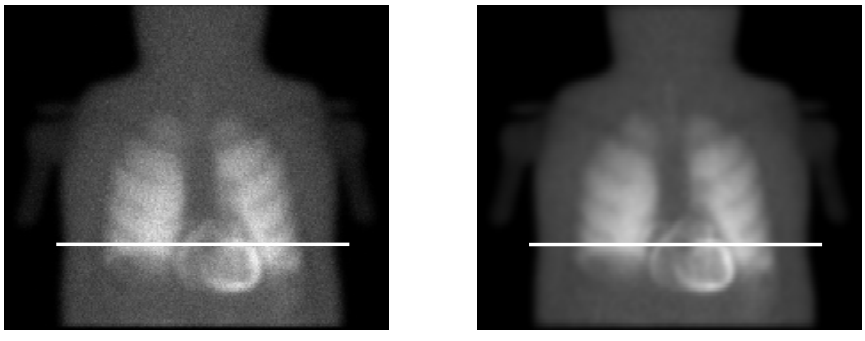

(a) GATE **(b)** CFD-SIMIND

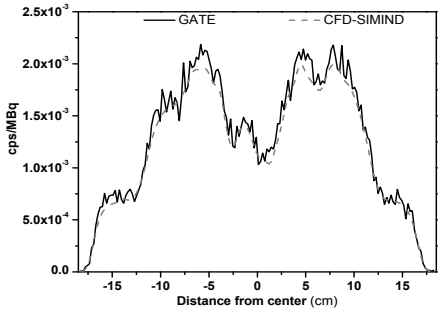

(c) XCAT image profile

Figure 2.6: ^{99m}Tc with LEHR collimator: XCAT images obtained in case of ^{99m}Tc with LEHR collimator through (c) GATE and (d) CFD-SIMIND simulations whereas, (c) shows image profile along the line depicted in both the projections shown in (c)and (d).

A comparison similar to that performed for ^{99m}Tc is depicted for ^{111}In XCAT simulations in Figure 2.8. The XCAT projections acquired using GATE and CFD-SIMIND for i) ^{111}In PEW (i.e. sum of 171 keV and 245 keV PEW) and, ii) ^{111}In down-scatter energy window, with window width equal to that used for ^{99m}Tc, with MEGP collimator. The respective GATE and CFD-SIMIND projections for i) are shown in Figure 2.8(a) and 2.8(b) whereas, the projections for ii) are depicted in Figure 2.8(c) and 2.8(d). A comparison of image profiles for ^{111}In for data sets i) and ii) along the lines depicted in projections is shown in Figure 2.8(e) and 2.8(f). The

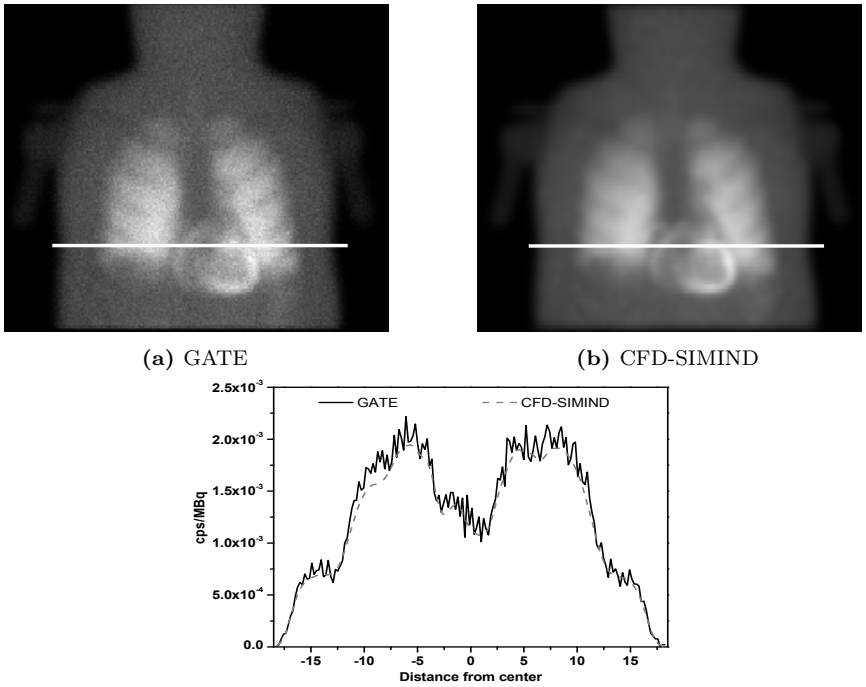

(a) GATE **(b)** CFD-SIMIND

(c) XCAT image profile

Figure 2.7: ^{99m}Tc with MEGP collimator: XCAT images obtained in case of ^{99m}Tc with MEGP collimator through (a) GATE and (b) CFD-SIMIND simulations whereas, (c) shows image profile along the line depicted in both the projections shown in (a) and (b).

XCAT phantom projection data sets i) and ii) acquired for ^{111}In using GATE and CFD-SIMIND show close agreement between the two MC simulators with Q_{UI} values of 0.993 and 0.983 for i) and ii) respectively.

A comparison of energy spectra for all tested isotope/collimator combinations given in Table 2.1, is shown in Figure 2.9. Table 2.5 compares GATE and CFD-SIMIND based XCAT energy spectra depicted in Figure 2.9 in terms of scatter to total counts in PEW and scatter-to-total spectrum area ratios for all the spectra. A comparison of XCAT spectra for all the energy windows described previously in Section 2.1.3, in terms of scatter composition is given in Table 2.6.

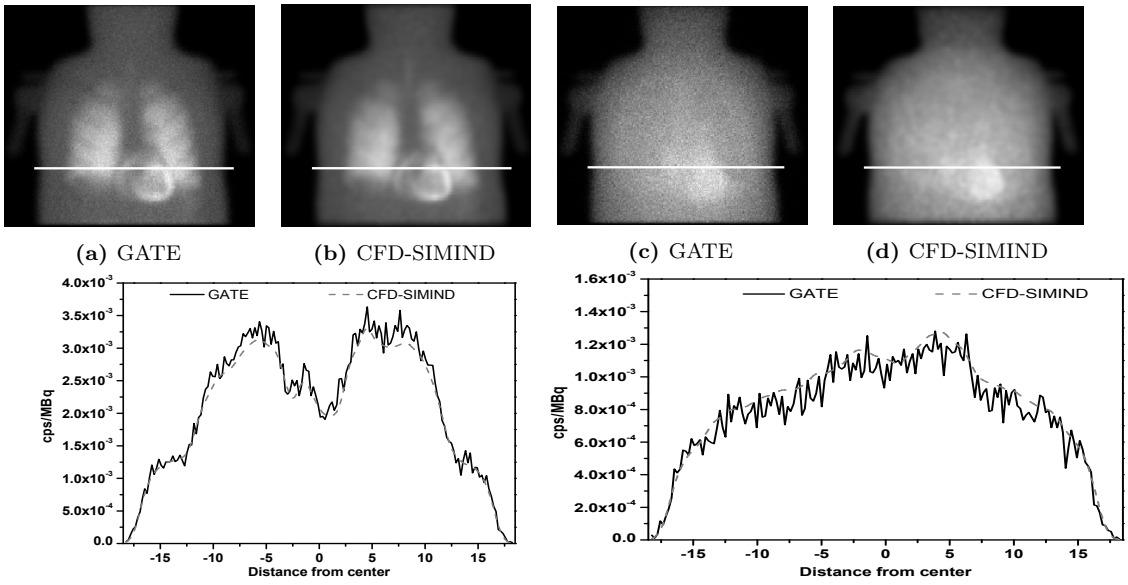

(a) GATE **(b)** CFD-SIMIND **(c)** GATE **(d)** CFD-SIMIND

(e) XCAT image profile **(f)** XCAT image profile

Figure 2.8: ^{111}In with MEGP collimator: XCAT images obtained with MEGP collimator for in case of i). summed ^{111}In PEWs (171 keV + 245 keV PEW) ii). ^{111}In in ^{99m}Tc down-scatter window obtained through (a) & (c) GATE and (b), & (d) CFD-SIMIND simulation for i) & ii) respectively. whereas, (e) and (f) show corresponding image profiles along the lines depicted in the projections for i) and ii) respectively.

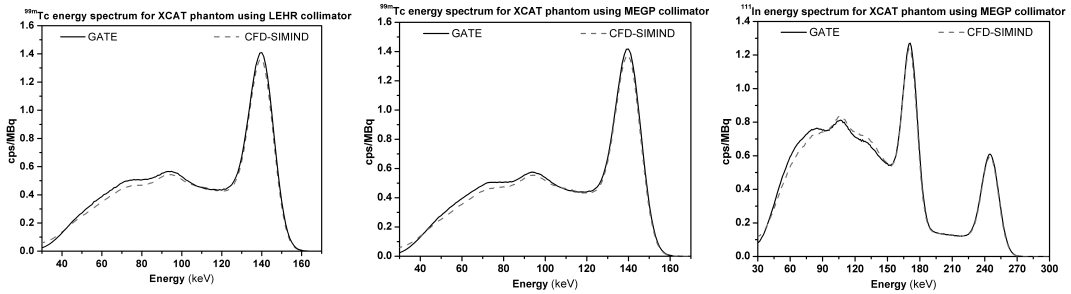

(a) ^{99m}Tc with LEHR **(b)** ^{99m}Tc with MEGP **(c)** ^{111}In with MEGP

Figure 2.9: XCAT simulations: Energy spectra for XCAT simulation of (a) ^{99m}Tc with LEHR collimator (b) ^{99m}Tc with MEGP collimator and (c) ^{111}In with MEGP collimator using GATE and CFD-SIMIND respectively.

Table 2.5: A summary of GATE and CFD-SIMIND quantitative spectral comparison for XCAT phantom simulations.

		Quantity	
		Scatter-to-total counts ratio (PEW)	**Scatter-to-PEW area ratio**
Acquisition	**MC Code**		
^{99m}Tc with LEHR collimator (PEW)	GATE	0.25	1.59
	CFD-SIMIND	0.25	1.59
^{99m}Tc with MEGP collimator (PEW)	GATE	0.25	1.60
	CFD-SIMIND	0.25	1.60
^{111}In with MEGP collimator (PEW)	GATE	0.32	2.62
	CFD-SIMIND	0.32	2.67

Table 2.6: Composition of scatter in all the acquired energy windows data for different isotope and collimator combinations used for XCAT phantom simulation.

		Percentage of total scatter					
Order of scatter		**1**	**2**	**3**	**4**	**5**	**>5**
Acquisition	**Code**						
^{99m}Tc with LEHR collimator (PEW)	GATE	84.87	13.47	1.51	0.14	0.01	0.00
	CFD-SIMIND	83.48	14.46	1.85	0.19	0.02	0.00
^{99m}Tc with MEGP collimator (PEW)	GATE	84.83	13.51	1.52	0.13	0.01	0.00
	CFD-SIMIND	83.43	14.48	1.87	0.20	0.02	0.00
^{111}In (171 keV) with MEGP collimator (PEW)	GATE	66.22	24.57	7.26	1.62	0.28	0.05
	CFD-SIMIND	66.51	24.41	7.14	1.61	0.28	0.05
^{111}In (245 keV) with MEGP collimator (PEW)	GATE	90.58	8.84	0.55	0.03	0.00	0.00
	CFD-SIMIND	90.12	9.23	0.61	0.04	0.00	0.00
^{111}In with MEGP collimator ^{99m}Tc PEW	GATE	49.01	32.65	13.07	4.00	1.02	0.25
	CFD-SIMIND	49.56	31.99	13.06	4.07	1.04	0.28

2.2.4 Uniform Sheet Source Simulations

A plot of CoV as a function of the number of detected photons for projections of a uniform sheet source is shown in Figure 2.10(a). The plot shows that GATE based CoV drops in accordance with the Poisson noise distribution with an increase in the number of counts in the projections, as expected. Comparatively, much lower and relatively constant CoV (3.13 ± 0.09 for ^{99m}Tc with LEHR, 3.86 ± 0.14 for ^{99m}Tc with MEGP and 3.83 ± 0.06 ^{111}In respectively) is seen for the CFD-SIMIND based projections, in spite of a lower number of simulated source photons. It is important to note here that CFD-SIMIND not only generated low-noise projections for each photopeak window, but also produced similar low-noise projections for ^{99m}Tc down-scatter window for ^{111}In (CoV = 3.10 ± 0.21), whereas the corresponding GATE based projection requires much larger number of detected photons to generate the projection with similar CoV. Similar results can also be seen from Figure 2.10(b), that depicts improvement in Q_{UI} with an increase in the number of counts in GATE based projections while noise properties of CFD-SIMIND based projections remain relatively constant (Figure 2.10(a)). The reduced CoV manifests itself as significantly

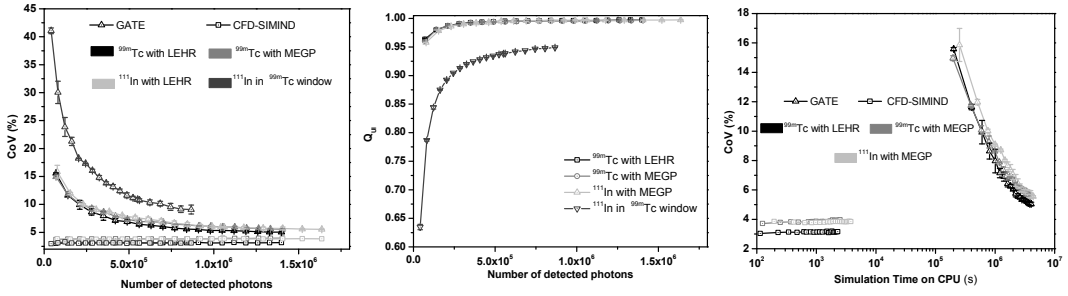

(a) Coefficient of variation versus number of detected photons

(b) Q_{UI} versus number of detected photons

(c) Coefficient of variation versus simulation time on CPU

Figure 2.10: Sheet source simulations: Comparison of different aspects for sheet source simulations between CFD-SIMIND and GATE in terms of (a) CoV and, (b) Q_{UI} as a function of number of detected photons. A plot of CoV versus simulation runtime on CPU is shown in (c).

lower simulation run-times for CFD-SIMIND compared with GATE for a given noise realization as evident from Figure 2.10(c). In round numbers, a single projection in GATE took 54 hours to generate a projection, whereas a similar, or higher quality image can be obtained in just 2-3 minutes with CFD-SIMIND.

2.3 Discussion

In this study, our accelerated CFD-SIMIND Monte Carlo program has been compared to GEANT4 based GATE for low and medium energy isotopes. Notably, CFD-SIMIND and GATE are similar in their use of Gaussian blurring for spatial resolution, but the way these blurring kernels are modeled is different for both. GATE uses real physics based probability distribution functions to model the response compared to CFD that uses modified response function and consequently different photon weight. Because once the photon leaves the phantom in CFD, it is forced to travel in a direction that is perpendicular to the detection system. It is also important to describe here that we have made no attempt to improve the intrinsic detection model in either CFD-SIMIND or GATE. Because we feel, this aspect is a minor in comparison to the geometric response and object scatter. An additional ^{99m}Tc acquisition in this study with MEGP collimator was performed to evaluate the compatibility between CFD-SIMIND and GATE for ^{99m}Tc with MEGP for possible applications of simultaneous ^{99m}Tc/^{111}In SPECT in cardiac, cancer, infection and gastric imaging ([86, 107–112]).

It is important to mention here that our implementation of CFD does not require a three dimensional sub-projection map and use of average attenuation coefficient as is the case with the CFD implementation reported by deJong *et al* [81]. This is due to the fact that in our case, a weighted copy of photon at each interaction site is directly convolved with the appropriate distance dependent Gaussian response kernel after corresponding photon energy based attenuation correction [29]. Also, CFD is implemented in such a way that the simulation is independent of a base projection and it only depends on the photon path and previous weighting.

Point source simulations in air yielded sensitivity values with percentage differences of 3−5% between CFD-SIMIND and GATE for all the isotope/collimator combinations used in this study. Slightly lower sensitivity values observed for the case of CFD-SIMIND, may be due to the absence of collimator scatter and septal penetration modeling.

It is also evident from Figure 2.3 that CFD-SIMIND has spatial resolution that is within 0.2 mm of the corresponding values for GATE at different source to collimator distances. These results are consistent with our previously reported data for CFD-SIMIND with detailed collimator scatter and septal penetration modeling [29, 82].

A comparison of image profiles, energy spectra and quantitative analysis of spectra

in terms of scatter-to-PEW area ratio, scatter-to-total counts ratio in PEW and scatter composition in the photopeak window for all the isotopes and collimator combinations used in the study indicate very good agreement between CFD-SIMIND and GATE for low and medium energy isotopes. A slight reduction in Q_{UI} values with increasing depth in water is evident from Table 3.2 and may be caused by lower counts and hence higher noise level at larger source depth in GATE based projection data. Also, slightly lower values of Q_{UI} at source depths of 5 cm in Table 3.2 may indicate a more significant contribution from collimator scatter in the overall scatter contribution detected within the photopeak at this depth. All point source simulations in water yielded an average value of 0.994 ± 0.009 for Q_{UI}. Table 3.2 also indicates an overall percent difference of 4.5 ± 0.6, 4.0 ± 0.8 and 2.4 ± 0.6 in sensitivity for ^{99m}Tc with LEHR, ^{99m}Tc with MEGP and ^{111}In respectively with CFD-SIMIND on the lower side.

In order to compare CFD-SIMIND to GATE for extended source distribution and non uniform density map, simulation studies using the XCAT phantom were performed. It is important to note here that conversion of attenuation to density, required for CFD-SIMIND simulation, is based on two distinct linear regions with inflection point at 1.0 gcm^{-3} as shown in Figure 2.2. Our previous linear conversion from attenuation coefficient to density (with body (water) density of 1 g/cm^3 $\Rightarrow$ μ = 0.1494 cm^{-1} for ^{99m}Tc) using a single slope results in about 15% and 24% lower density values for spine and rib bone respectively. Therefore, care must be taken while performing this conversion for bones or other high density materials like iodine based contrast agents [113]. A comparison in terms of a global parameter like Q_{UI} and localized comparison using line profiles shown in Figures 2.6(c), 2.7(c), 2.8(e) and 2.8(f) show a good agreement between CFD-SIMIND and GATE based projections. The data presented in Section 2.2.3 show similarity between GATE and CFD-SIMIND images with a mean Q_{UI} value of 0.988 ± 0.005 for all photopeak images. The corresponding energy spectra for all the isotope/collimator combinations used in the study appears to match well with a mean percent difference of 4.8 ± 0.8 in sensitivity with CFD-SIMIND on the lower side. The comparison of an additional down-scatter window (= ^{99m}Tc PEW) acquired for ^{111}In showed a value of 3.0% (with GATE on the lower side) and 0.983 for percent difference in sensitivity and Q_{UI} respectively. The CFD-SIMIND based XCAT images acquired for PEW shown in Figures 2.6, 2.7 and 2.8 appear to match well with corresponding GATE images possess slightly more graininess (i.e., more Poisson noise). This graininess is also evident in the GATE based image for

^{99m}Tc downscatter window in Figure 2.8(c). Notably, Figure 2.8(d) shows correlated lumpy-noise texture that is typical for CFD and indicative of insufficient number of detected photons in given energy window [81]. The main reason for this low frequency lumpy-noise is the projection of each photon as a blurring kernel. The difference in noise properties and insufficiency of detected counts could be the main causes for the visual differences between the images in Figures 2.8(c) and 2.8(d).

The results of the uniform sheet source simulation (Figure 2.10) has shown that relatively low-noise images can be acquired using CFD-SIMIND with much lower number of photon histories and with a subsequent reduction of about 5−6 orders of magnitude in simulation time compared to GATE.

2.4 Conclusion

It is evident from the point source simulation results that CFD-SIMIND agrees well with GATE with detection sensitivity differences ranging from (3−5%), resolution within 0.2 mm and overall image quality similarly, Q_{UI} value, of 0.994 ± 0.009. More complex simulations using the XCAT phantom also showed similar results. Based on the coefficient of variation measurements as a function of number of counts and simulation time, a reduction by a factor of 5−6 orders of magnitude in time can be achieved with CFD-SIMIND compared to GATE while maintaining very similar photon transport accuracy.

Chapter 3

Simultaneous ^{99m}Tc/^{111}In SPECT Reconstruction using Accelerated Convolution-based Forced Detection Monte Carlo

Published in IEEE Transactions on Nuclear Science©, Volume 62 (5), Pages 2085-2095, 2015

SIMULTANEOUS ^{99m}Tc/ ^{111}In SPECT imaging has potential applications in cardiac, cancer, infection and gastric imaging. For example, ^{99m}Tc-sestamibi and ^{111}In-labelled cardiomyoblasts have been used to simultaneously monitor myocardial perfusion and stem cell localization following cellular cardiomyoplasty [108, 109]. In prostate cancer imaging, Blend *et al* has proposed the use of ^{99m}Tc/ ^{111}In imaging to distinguish prostate and lymph node involvement from the vascular component [111, 112]. SPECT imaging using ^{99m}Tc-hydroxymethylene diphosphonate and ^{111}In-labelled white blood cells has been recently reported as a useful tool in localization of diabetic foot infection [114]. A feasibility study of gastric volume and gastric emptying measurements using ^{99m}Tc-pertechnetate and ^{111}In-DTPA respectively, have been performed by Siomonian *et al* [110].

When performing dual isotope imaging, serial imaging of ^{99m}Tc followed by ^{111}In not only prolongs imaging time but may also result in misregistration of images as a result of patient movement between scans. Therefore, in order to avoid these problems and

to improve system throughput, it is advantageous to perform simultaneous imaging of both radionuclides. The major concern in such an acquisition however, is the significant crosstalk contamination as a result of photon scatter.

Different crosstalk compensation methods developed for the precorrection of SPECT projection data typically either subtract a crosstalk estimate from the projection data prior to image reconstruction or attempt to improve projection data by means of deconvolution with a crosstalk blurring function [115–119]. Feng, *et al*, compared triple energy window (TEW) based correction method [119] to their proposed convolution based method to correct for ^{111}In down-scatter detected in the ^{99m}Tc photopeak energy window (PEW). Their study showed marked reduction in ^{111}In source intensity in the ^{99m}Tc image [118]. However, the problem with pre-reconstruction crosstalk correction methods is the *ad hoc* determination of parameters like scaling factors or blurring functions necessary for more accurate compensation.

In contrast to pre-corrective strategies, other researchers have proposed to incorporate model based crosstalk compensation during the image reconstruction process (c.f. [92–94, 120–123]). Frey, *et al* has developed and used a method of model-based crosstalk compensation known as effective source scatter estimation (ESSE) [120–123]. Song *et al*, [121], evaluated ESSE-based crosstalk compensation in simultaneous ^{99m}Tc/^{201}Tl myocardial SPECT and showed that this model yielded good estimates of crosstalk and Pb x-rays produced in the collimator.

Another modeling method has been developed by Ouyang *et al* [93]. This method initially reconstructs both isotopes without any scatter correction (NSC-OSEM) using simulated detector PSF's at 32 detector to source distances in air. The data reconstructed using five iterations of NSC-OSEM was then corrected for scatter and crosstalk using an accelerated Monte Carlo method in a joint ordered subset expectation maxmimization (JOSEM) algorithm. The Monte Carlo method employed was a modified version of the accelerated method proposed by deJong *et al* [81].

In order to evaluate the scatter and crosstalk compensation of this technique, a simulation study involving the simultaneous imaging of ^{99m}Tc/ ^{111}In of infection was performed by Cervo *et al* [94]. Results of this study indicate a bias in the range of -3.9 to 34.8% in activity quantitation with overall precision of 12.8%. deJong *et al* [92] has proposed a method for down-scatter correction in simultaneous ^{99m}Tc/^{201}Tl dual-isotope cardiac SPECT. In this approach, a stable down-scatter estimate is calculated using an accelerated Monte Carlo simulation technique along with a simulation of lead

x-ray production. From their study, they found that "Monte Carlo-based down-scatter correction recovers lesion contrast and quantitative accuracy in ^{201}Tl images almost perfectly".

More recent approaches used for crosstalk compensation in simultaneous dual-isotope SPECT, involved the use of artificial neural networks (e.g. [124, 125]) or independent component analysis [126]. In a study performed by Zheng *et al* [124], experimentally acquired projection data consisting of 24 energy windows was used to train an artificial neural network (ANN) for crosstalk correction in simultaneous ^{99m}Tc/^{123}I brain imaging. In this study they were not able to train the ANN for self scatter correction but the system was able to reduce crosstalk significantly. Chang *et al* applied independent component analysis in order to correct for the crosstalk in simultaneous ^{99m}Tc/^{123}I planar imaging [126]. This study reported a percent bias (Mean Square Error (MSE)) of <-11% (80.48) and <-18% (104.63) in ^{99m}Tc and ^{123}I respectively. These techniques are both very good at compensating for crosstalk, however, the major limitation in these methods is the requirement for a large number of energy windows, whereas many commercially available SPECT systems only provide limited numbers of energy windows.

In this work, we present an alternative method of crosstalk compensation applied to simultaneous ^{99m}Tc and ^{111}In SPECT for cancer imaging. This technique uses a Monte Carlo-based photon transport model during the reconstruction process. Monte Carlo (MC) based scatter compensation has the potential to offer the most realistic crosstalk and scatter compensation modeling compared to approximative methods. However, the inherently low detection efficiency and resultant long calculation times (often several hours or days) associated with this technique makes it unsuitable for most clinical applications [127]. As a result, previously reported methods which involved the use of MC based scatter and crosstalk estimates either used a stable estimate [92] obtained after several iterations and held constant, or applied the scatter estimate only in the latter stages of image reconstruction [93]. While the advent of increasingly fast computers has reduced computation times, we have taken an alternative approach to improve simulation times. Our group has previously incorporated convolution based forced detection (CFD) into the SIMIND Monte Carlo program (SIMIND-CFD), which has made MC modeling feasible to use in clinical time frames [29]. We have developed an iterative Monte Carlo-based image reconstruction technique that simulates the photon down-scatter from one isotope into the acquisition window of a second isotope.

By accurately modeling the photon transport through the object of interest using Monte Carlo, we can accurately estimate the amount of scatter contamination contained in a given projection view within an arbitrary energy range. Once known, we then use this information in an iterative algorithm to compensate for the photon contamination using updated scatter estimates for each image update during reconstruction. We use a modified ordered subset-expectation maximization (OS-EM) algorithm [128], named simultaneous ordered subset-expectation maximization (Sim-OSEM) to perform this step.

In this study, a comparison between the quality of images reconstructed from simulated and experimentally acquired projection data in terms of contrast, activity deposition and uniformity of background was performed. The use of MC also facilitates quantitative estimation using the method mentioned in following Section 3.1.1, although this was not the primary purpose of this study.

3.1 Methods

The main objective of this work is to evaluate our proposed reconstruction algorithm, Sim-OSEM for use in simultaneous ^{99m}Tc/^{111}In SPECT and to test the results of this method against other methods. Our approach uses the standard OSEM algorithm modified for multiple acquisition windows, along with a quantitation estimation step. The description of this technique follows.

3.1.1 The Sim-OSEM Reconstruction Method

Consider an object containing two different isotopes, x and y with differing *in vivo* distributions. The distribution of nuclide x is given by f_x and that of nuclide y by f_y. In a simultaneous acquisition, the resultant projection data acquired for each nuclide (p_x and p_y) can be represented by the linear Equations (3.1) and (3.2).

$$H_{xx}f_x + H_{yx}f_y = p_x \tag{3.1}$$

and

$$H_{xy}f_x + H_{yy}f_y = p_y \tag{3.2}$$

where H_{xx} and H_{yy} are the photopeak photon geometric system matrices for each

respective isotope, H_{yx} and H_{xy} are the scatter photon system matrices for the isotope y (or x) into the acquisition window for isotope x (or y). Note that p_x and p_y are the projections acquired in a single photopeak window for each nuclide. In the case of multiple energy photons, such as ^{111}In, p_y is the resultant sum of the individual photopeak projections. That is, for y=^{111}In,

$$\begin{aligned} p_{In} = H_{171,171} f_{In,171keV} + H_{245,171} f_{In,245keV} + ... \\ H_{245,245} f_{In,245keV} + H_{171,245} f_{In,171keV} \end{aligned} \tag{3.3}$$

Note that the scatter system matrix H_{xy} or H_{yx}, for example, can be considered comprised of two parts, i) a system matrix that models photon transport through the object, and ii) a system matrix that models photon transport through the collimator and imaging system. In the CFD-MC implementation, the former component is modeled for each isotope using standard Monte Carlo up to the last scatter location in the object. At this point, the latter component is performed using an analytical projection of the photon on to the detector surface. The geometric response projected is modeled by a depth dependant Gaussian with FWHM given by:

$$G_x(z, E) = \frac{d(l_{eff}(E) + z)}{l_{eff}(E)} \tag{3.4}$$

where d is the collimator hole diameter, l_{eff} is the effective septal length for a specific photon energy equivalent to $l_{eff} = l - 2/\mu(E)$ and z is the distance from the collimator face. It should be noted here that detailed septal penetration and collimator scatter modeling have not been implemented in CFD-MC in this study. We have used an exponential relationship for $\mu(E)$ as the attenuation coefficient for lead follows an exponential function over the range of energies appropriate for ^{99m}Tc and ^{111}In as shown in Equation 3.5. The expression shown in Equation 3.5 is the function of energy, E, in keV obtained by curve fitting the attenuation data from National Institute of Standards and Technology (NIST) website (http://www.nist.gov).

$$\mu(E) = 0.2483 \times exp\left(\frac{1233.8487}{E + 122.92}\right) \ (cm^{-1}) \tag{3.5}$$

The Sim-OSEM reconstruction algorithm for ^{99m}Tc can be written as Equations

3.6 with a similar expression for ^{111}In.

$$f_{Tc}^{new} = \frac{f_{Tc}^{old}}{\sum_{a\epsilon s} H_{a,Tc}^{T}} \sum_{a\epsilon s} H_{a,Tc}^{T} \frac{\bar{p}_{a,Tc}}{p_{a,Tc} R_{Tc}^{new} t_{acq}} \tag{3.6}$$

where $\bar{p}_{Tc}$ is the measured projection data for ^{99m}Tc and p is the Monte Carlo estimated projection data for ^{99m}Tc as per Equation 3.1. Notice that in the forward projection step (denominator), there is an additional factor, $R_i^{new} t_{acq}$. Because of the forced detection variance reduction technique used in CFD-MC, each detected count is scaled by the probability of detection in order to provide units of cps/MBq. Hence the list-mode projection data must be scaled to account for the actual acquisition times, t_{acq} and the absolute quantitative activity R_i^{new}. This scaling factor, R_i^{new} is determined through an iterative process based on the total number of counts acquired in the experimental projection data, p, and the MC simulated projection as shown in Equation (3.7) for $^{99\mathrm{m}}$Tc.

$$R_{Tc}^{new} = R_{Tc}^{old} \frac{\sum_{a\epsilon s} \bar{p}_{a,Tc}}{\sum_{a\epsilon s} (H_{a,TcTc}^{'} f_{Tc}^{old} + H_{a,InTc}^{'} f_{In}^{old}) \times t_{acq}} \tag{3.7}$$

In the backprojection step, we have implemented an analytical backprojector, H^T, that includes both energy specific attenuation and geometric collimator response compensation, but does not include scatter compensation. For each forward projection, a low noise projection consisting of 5×10^6 photon histories were simulated using the MC based forward projector. This forward projector uses intrinsic camera resolution and attenuation weighted distance dependent collimator resolution to model overall detector response [29]. As previously mentioned, we have not included the effects of septal penetration, collimator scatter or Pb x-ray production, although we have previously implemented an accelerated version of septal penetration using ray tracing [82]. In CFD, the computationally intensive task of photon transport through the object needs to be performed only once for each photon while maintaining the accuracy to an acceptable level [29, 129].

3.1.2 CFD Monte Carlo Model Validation

All subsequent experiments to test the proposed reconstruction method utilized a GE Infinia SPECT/CT camera (General Electric, USA). This camera first had to be accurately modeled with our accelerated Monte Carlo program. In order to model the geometric response of the combined camera/collimator system, point sources (<3 mm diameter) of both ^{99m}Tc and ^{111}In were used to measure the depth dependent spatial resolution of the medium energy, general purpose collimator (MEGP). For each isotope, the point source was positioned at five different distances from the collimator surface (5, 10, 15, 20, 25 cm) and low noise projection data acquired into a 1024×1024 pixel array (1.1 mm × 1.1 mm). Profiles in both X and Y directions of the obtained point spread function was measured and FWHM determined and plotted as a function of distance. A best-fit line was fit to these 5 points in order to determine the depth dependant spatial resolution.

The obtained distance-dependent resolution model described in Section 3.1.1 was then implemented into our CFD version of the SIMIND Monte Carlo program. To confirm the geometric modeling matched the actual camera, a simulation was performed using point sources of ^{99m}Tc and ^{111}In positioned at various distances from the simulated camera, emulating the experiment performed previously. Low noise Monte Carlo projections were acquired and the resultant FWHM of projection image again fit with a depth dependent Gaussian function. A comparison in terms of overall detector sensitivity was also performed. The detection efficiency (counts $s^{-1}MBq^{-1}$) was measured for projection data acquired at a source to collimator distance of 10 cm.

In addition to experimentally measured efficiency values, a comparison between SIMIND-CFD and GEANT4 Monte Carlo (i.e., GATE) [89] code was also performed in order to validate the SIMIND Monte Carlo program with another, previously validated method. GATE scatter estimates have previously been compared to experimental data for ^{111}In in a study performed by Assie *et al* [91]. In this study, a difference of 2% and 4% in spatial resolution and sensitivity values, respectively, has been reported for GATE simulation results compared to experimental data. Thus, if SIMIND-CFD projection estimates are similar to GATE, then we can assume SIMIND-CFD will provide appropriate scatter estimations for experimental data. An identical setup for the GATE simulation was used as for the experimental and SIMIND-CFD based measurements mentioned above.

In order to evaluate the ability of SIMIND-CFD to model and estimate ^{111}In downscatter in ^{99m}Tc PEW more quantitatively, a point source of activity was simulated at different depths in water using both GATE and the SIMIND Monte Carlo methods. For both simulations, the same GE Infinia gamma camera model was implemented and acquisition using ^{111}In and ^{99m}Tc point sources (4.4 mm diameter) in a cubic water bath ($56.576 \times 56.576 \times 56.576$ cm^3) was performed at 5 different depths in water (5, 10, 15, 20, 25 cm). For the case of SIMIND, a total of 1.1×10^7 photon histories were simulated, whereas GATE simulated a 10 minute acquisition of a 1MBq source, thereby approximating low-noise projection data.

It is important to note here that in the case of ^{111}In, two projection data sets are obtained: i) the summed photopeak window (i.e. 171 keV + 245 keV windows) and ii) the ^{99m}Tc downscatter energy window data. We chose to sum together the 171 and 245 keV ^{111}In photopeak data as this is identical to our clinical SPECT acquisition protocol.

Similarly, for the case of ^{99m}Tc, again, two projection images are obtained. These consist of, i) the ^{99m}Tc PEW without any ^{111}In downscatter present and ii) the ^{99m}Tc PEW with ^{111}In downscatter image added. The GATE MC and SIMIND-CFD results were then compared in terms of Normalized Mean Square Error (NMSE) for i) ^{111}In photopeak, ii) ^{99m}Tc photopeak without ^{111}In downscatter and iii) ^{99m}Tc photopeak with ^{111}In downscatter energy window projections respectively.

3.1.3 Sim-OSEM Feasibility

In order to test the feasibility of the proposed Sim-OSEM reconstruction algorithm, a phantom simulation study based on the NEMA IEC body phantom (Data Spectrum Corporation) was performed. Three of six spheres (diameter (ϕ) = 13 (S1), 22 (S3) and 37 mm (S5) respectively) were filled with 7.75 MBq of ^{99m}Tc (concentration = 0.151 MBq/ml) while the remaining three spheres (ϕ = 10 (S2), 17 (S4) and 28 mm (S6)) contained a total of 7.56 MBq of ^{111}In (concentration = 0.302 MBq/ml). The activity values were calculated to obtain an activity concentration ratio of 1:2 between ^{99m}Tc and ^{111}In respectively. For each radionuclide, a simulated SPECT acquisition was performed using 120 projections with 128×128 matrix size (4.4 mm x 4.4 mm pixels). Projection data were obtained using the CFD-MC method implemented into SIMIND. A total of 480 million photon histories were simulated for each of the isotopes, thus approximating low-noise projections. The current implementation

of CFD SIMIND provides relative projection images in units of cps/MBq, therefore scaling of the low-noise projection data to actual activity levels and acquisition time was performed and then Poisson distributed noise added. Both for acquisition and reconstructions, the attenuation map was obtained from a transmission CT scan of the phantom acquired on the GE Infinia Hawkeye 4 SPECT camera. It is noted here that while it would be preferable to utilize a different simulation method (e.g., GATE) to obtain simulated projection data, our goal at this point was to simply evaluate the application and feasibility of the proposed reconstruction method, rather than to perform a rigorous evaluation. As described below, our reconstruction technique uses a mis-matched projector/backprojector pair, of which the combined effect in the reconstruction procedure is unknown.

The simulation used an acquisition time of 15 s/projection, thus yielding 1.2 and 1.4 million counts over all ^{99m}Tc (with ^{111}In downscatter added) and ^{111}In (summed photopeak window) projections respectively. Projection data were acquired with 20% wide windows for all photopeaks, with additional 3 keV wide scatter windows adjacent to each photopeak in order to perform triple energy window (TEW) based scatter correction [119]. It should be noted that the 245 keV photopeak energy for ^{111}In utilized only a single, lower scatter window.

The Sim-OSEM based reconstructed images were compared to images obtained using i) conventional reconstruction of SPECT data without any scatter compensation, ii) data corrected using TEW compensation in the forward projection step and iii) single isotope data without any crosstalk contribution from other isotope and reconstructed without scatter compensation. In all these other cases, the image reconstruction process uses a matched projector/backprojector pair that includes both photon attenuation and geometric response compensation incorporated into the standard OSEM reconstruction algorithm. In the case of Sim-OSEM, the reconstruction algorithm produces estimates of activity concentration in units of (Bq/cc). The other reconstruction methods do not yield quantitative images unless calibrated using a standardized source. No calibration was performed for these experiments as the goal of this work was not to perform an evaluation of quantitative accuracy of each method. All the reconstructions were performed with 2 iterations and 30 subsets.

In order to evaluate and compare the improvement in contrast, the peak to valley ratios (PVR) were calculated using Equation 3.8 from the circular profiles for both

the isotopes.

$$PVR = \frac{\bar{x}_p}{\bar{x}_v} \tag{3.8}$$

where $\bar{x}_p$ and $\bar{x}_v$ are the three point average at the peak and at the bottom of valley succeeding the peak respectively. In order to compare the reduction in background scatter mean content of normalized data sets in a spherical VOI of radius 2.2 cm in the background region, away from the spheres with activity, was also compared.

After reconstruction of simulated data, while not the purpose of this work, using Sim-OSEM, a 3D volume of interest (VOI) was drawn over each phantom sphere and the mean reconstructed activity concentration (kBq/cc) was determined. In this work the VOI was selected based on the actual volume of spheres without any partial volume correction.

3.1.4 Experimental Validation of Sim-OSEM

Once evaluated for feasibility, we have performed a series of experimental dual-isotope ^{111}In/^{99m}Tc SPECT studies using a similar design to the simulation study as described in Section 3.1.3. The amount of activity used was calculated to obtain an activity concentration ratio for ^{99m}Tc : ^{111}In of 1:2. We have performed the following experiments:

i) Simultaneous ^{111}In/^{99m}Tc with non-radioactive water background.

ii) Simultaneous ^{111}In/^{99m}Tc with a ^{99m}Tc background.

Initially, ^{99m}Tc was injected into 3 spheres and SPECT projection data of these spheres was obtained. Then ^{111}In was injected into the remaining 3 spheres while the phantom was positioned on the patient bed. As the cross-contamination from ^{99m}Tc to ^{111}In is considered negligible, this permitted us to obtain both ^{99m}Tc and ^{111}In projection data essentially free of cross-talk from the other nuclide.

In the case of the warm background, ^{99m}Tc was deposited into the phantom background in order to obtain an activity concentration ratio ^{99m}Tc in background:^{99m}Tc in spheres:^{111}In as 1:20:40.

For both the experimental acquisitions, 120 projections were acquired with a matrix size of 128 × 128 pixels (pixel size = 4.4 mm) with 20 s/projection. The same energy window widths used in simulation study described in Section 3.1.3 were also used for both the experiments.

Similar to the simulation study, Sim-OSEM based reconstructed images were

compared in terms of circular profiles, PVRs and uniformity of background to images obtained using i) conventional reconstruction of SPECT data without any scatter compensation, ii) data corrected using TEW compensation in the forward projection step and iii) single isotope data without any crosstalk contribution from other isotope and reconstructed without scatter compensation. In all these other cases, the image reconstruction process used a matched projector/backprojector pair that included both photon attenuation and geometric response compensation incorporated into the standard OSEM reconstruction algorithm. In presence of warm ^{99m}Tc background, the comparison with the single isotope data without any crosstalk contribution from other isotope and reconstructed without scatter compensation was not performed, as single isotope data was not acquired in this case. All the reconstructions were performed using 2 iterations and 30 subsets in accordance with our current clinical protocol.

3.2 Results

3.2.1 Monte Carlo Validation

A comparison between experimental and simulated FWHM values, measured using the method described in Section 3.1.2, shows that the experimental and simulated FWHM values are very close and within ± 1 mm over all source distances. The results were consistent with our previously reported validation of SIMIND-CFD [29].

Table 3.1 shows the detection efficiency values for ^{111}In and ^{99m}Tc energies respectively at a source to collimator distance of 10 cm for experimental, SIMIND-CFD and GATE data. The values in Table 3.1 were used to calculate an overall efficiency correction factors of 1.06, 1.12 and 1.00 for SIMIND based projections of ^{111}In (171 kev), ^{111}In (245 keV) and ^{99m}Tc (140 kev) when modeling our Infinia camera. SIMIND-CFD based efficiency values match well with the values obtained from GATE (typically $< 5\%$ in all cases).

The NMSE values obtained for a comparison of SIMIND-CFD to GATE MC projection data at different depths in water with respect to the collimator surface are given in Table 3.2. There is a very good agreement between the SIMIND-CFD and GATE MC based ^{111}In photopeak (0.009-0.040), ^{99m}Tc photopeak without (0.015-0.045) and with ^{111}In downscatter added (0.010-0.069) energy window projections in terms of NMSE values, especially at lesser water depths (i.e., less photon scatter).

Table 3.1: Detection efficiency values for medium energy general purpose (MEGP) collimators at source to collimator distance of 10 cm in air.

	Sensitivity (cps/MBq)			
Isotope	**Head 1**	**Head 2**	**SIMIND-CFD**	**GATE MC**
^{111}In (171 keV)	69.5	68.5	65.1	64.4
^{111}In (245 keV)	45.9	45.5	40.6	42.7
^{99m}Tc (140 keV)	75.0	72.8	74.0	76.3

Figure 3.1 shows image profiles on both logarithmic and linear scales obtained from a representative SIMIND-CFD and GATE MC point source simulation in water (shown at 10 and 15 cm depths) for i) ^{111}In photopeak, ii) ^{99m}Tc photopeak without and iii) with ^{111}In downscatter added projections respectively as example. It is evident from these data that SIMIND-CFD provides very similar photon transport modeling to GATE and should be applicable to use for experimental SPECT implementation.

Table 3.2: Normalized mean square error (NMSE) at different depths in water for SIMIND-CFD compared to GATE MC.

	NMSE Value		
Depth (cm)	**^{111}In Photopeak energy window**	**^{99m}Tc Photopeak energy window**	**^{99m}Tc window with downscatter**
5	0.016	0.019	0.018
10	0.009	0.015	0.010
15	0.013	0.020	0.014
20	0.020	0.027	0.029
25	0.040	0.045	0.069

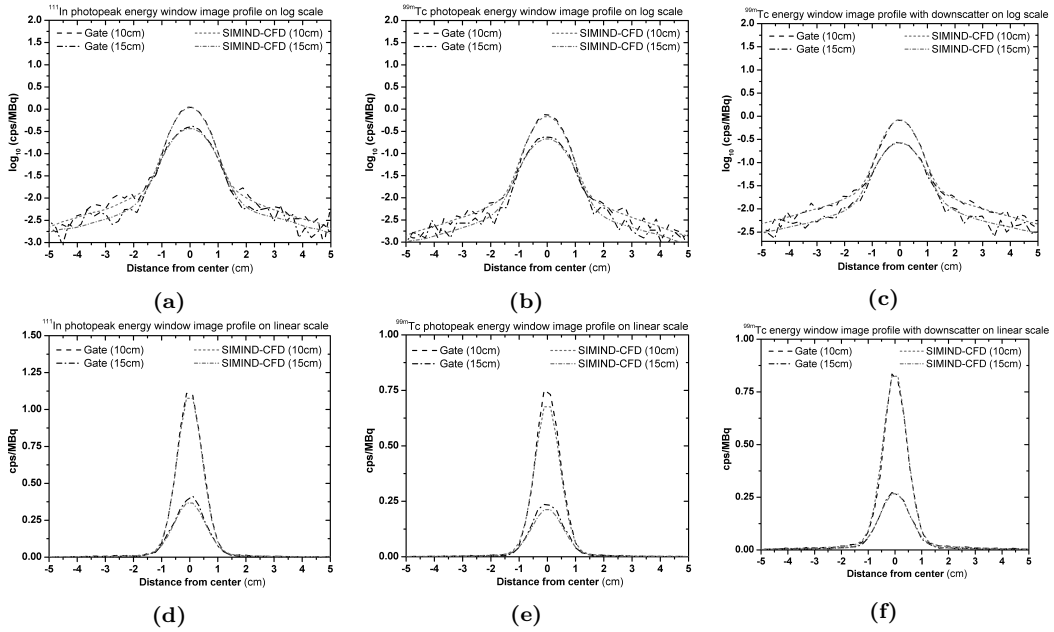

Figure 3.1: Image profiles obtained at source to collimator distance of 10 and 15 cm with GATE MC and SIMIND-CFD simulation for (a) ^{111}In photopeak, (b) ^{99m}Tc photopeak and (c) ^{99m}Tc photopeak plus ^{111}In downscatter energy window images on logarithmic scale, whereas corresponding profiles are shown in (d), (e) and (f) on linear scale respectively.

3.2.2 SPECT Simulation Results

A slice through the image reconstructed from the simulation data acquired with no background activity is shown in Figure 3.2. From Figure 3.2, it can be seen that the image reconstructed using conventional OSEM algorithm with no crosstalk compensation (Figure 3.2c) shows significant crosstalk compared to scatter compensated reconstructions (i.e., TEW (Figure 3.2d) and Sim-OSEM based dual isotope reconstructions (Figure 3.2e)). Furthermore, the proposed Sim-OSEM based dual-isotope reconstruction yields a more uniform background and improved contrast for ^{99m}Tc compared to TEW scatter compensation. Improved contrast with reduced and more uniform background is also evident for the ^{111}In image as seen in Figures 3.2.

Figure 3.3(a) and Figure 3.3(b) depict circular profiles through the central region of the ^{99m}Tc and ^{111}In images as shown in Figure 3.2. It is evident that both TEW and the proposed Sim-OSEM reconstruction methods result in less crosstalk contamination in the ^{99m}Tc image compared to no crosstalk compensation (most noticeable in spheres S2 and S4 in Figure 3.3(a)). Apparent on the log plot, the Sim-OSEM method further reduces the background scatter contamination beyond that even the no crosstalk

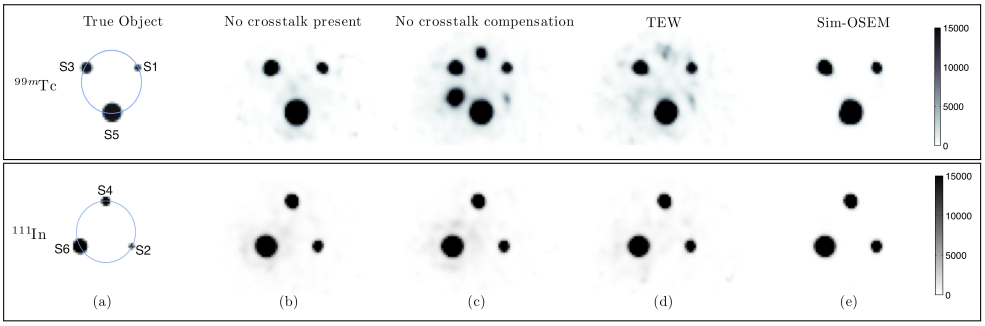

Figure 3.2: Infinia Simulation cold background: Top row) Reconstructed images for ^{99m}Tc using different reconstruction algorithms. Bottom row) Reconstructed ^{111}In images from the same reconstruction methods. (a) is the true simulated object, (b) image reconstructed using separately acquired data with no crosstalk (c) is the image reconstructed without crosstalk compensation, & (d) image reconstructed using TEW based correction of data with the help conventional analytical reconstruction method and (e) image reconstructed using Sim-OSEM. Note that images have been thresholded to accentuate the background.

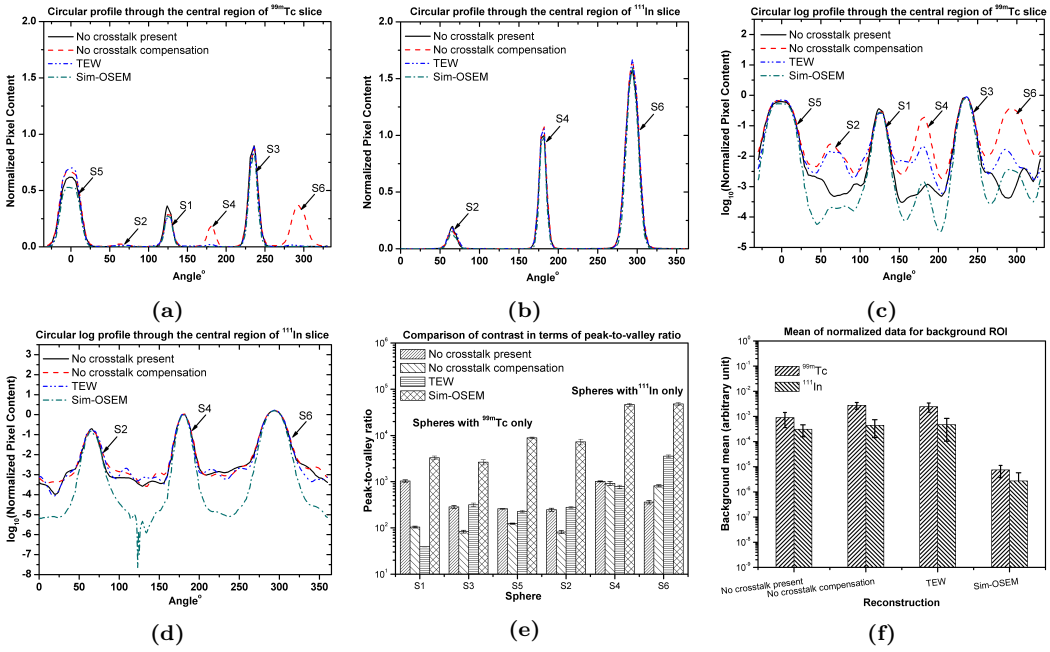

Figure 3.3: Infinia Simulation cold background: Circular profiles through the central regions (indicated by blue circles in Figure 3.2) of the reconstructed image slices shown in Figure 3.2. (a) and (b) shows the respective profiles through the central region of normalized pixel values for ^{99m}Tc and the ^{111}In image in Figure 3.2 with corresponding profiles on log scale are shown in (c) and (d). (e) and (f) show the peak-to-valley ratios and mean voxel content of background VOI for all the normalized reconstructed data sets respectively.

present method. This is likely a result of the fact that no scatter compensation was performed for the no crosstalk contamination, yet the Sim-OSEM method does model

self-scatter within each photopeak window. All data sets have been normalized with respect to their respective global maxima for comparison purpose.

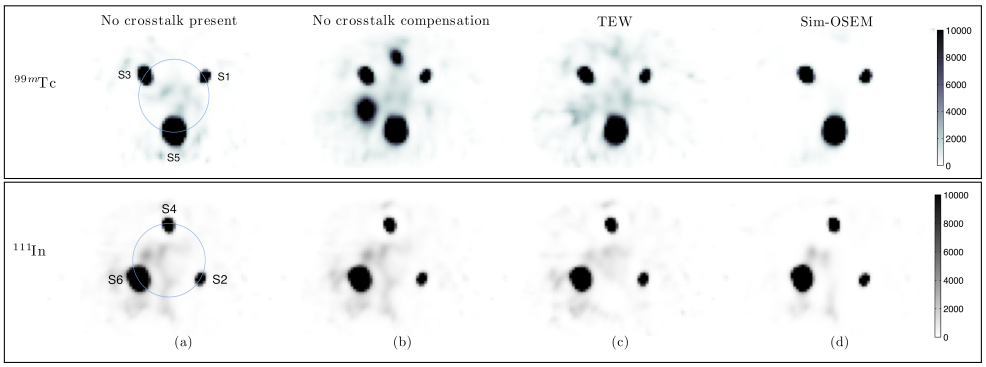

Figure 3.4: Infinia Experiment cold background: Top row) Reconstructed images for ^{99m}Tc using different reconstruction algorithms. Bottom row) Reconstructed ^{111}In images from the same reconstruction methods. (a) image reconstructed using separately acquired data with no crosstalk (b) is the image reconstructed without crosstalk compensation, & (c) image reconstructed using TEW based correction of data with the help conventional analytical reconstruction method and (d) image reconstructed using Sim-OSEM. Images have again been scaled to accentuate background activity.

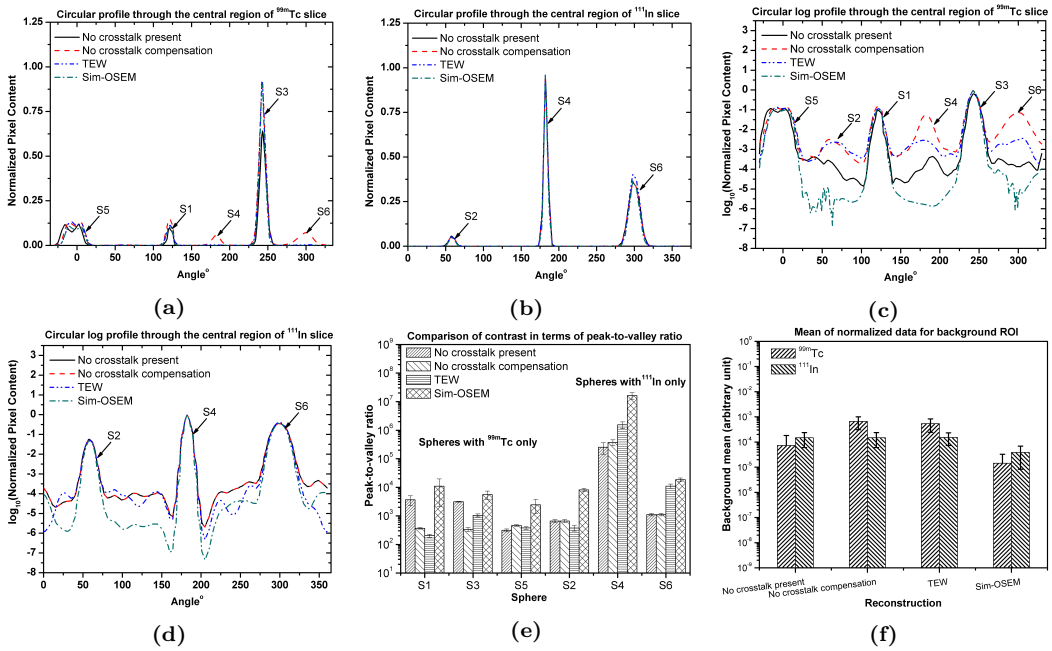

Figure 3.5: Infinia Experiment cold background: Circular profiles through the central regions (indicated by blue circles in Figure 3.4) of the reconstructed image slices shown in Figure 3.4 for experimental data in cold background. (a) and (b) shows the respective profiles through the central region of normalized pixel values for ^{99m}Tc and the ^{111}In image in Figure 3.4 with corresponding profiles on log scale are shown in (c) and (d). (e) and (f) show the peak-to-valley ratios and mean voxel content of background VOI for all the normalized reconstructed data sets respectively.

The PVR values, calculated using Equation 3.8, indicate a drastic improvement in case of Sim-OSEM (PVR (3.3 ± 0.3) $\times 10^3$ to (8.9 ± 0.4) $\times 10^3$) compared to TEW (PVR (3.92 ± 0.03) $\times 10^1$ to (2.3 ± 0.1) $\times 10^2$), no crosstalk present (PVR (2.590 ± 0.004) $\times 10^2$ to (1.04 ± 0.06) $\times 10^3$) and with no crosstalk compensation (PVR (8.3 ± 0.5) $\times 10^1$ to (1.23 ± 0.04) $\times 10^2$) ^{99m}Tc images respectively. The improvement seen with Sim-OSEM for ^{99m}Tc images is also evident for ^{111}In images. Figure 3.3(f) shows comparison of background scatter mean content of normalized data sets in spherical VOI described in Section 3.1.3. The reduction in background scatter in case of Sim-OSEM (Mean (8 ± 3) $\times 10^{-6}$ and (2.7 ± 3.0) $\times 10^{-6}$ for ^{99m}Tc and ^{111}In respectively.) compared to TEW (Mean (2.5 ± 1.0) $\times 10^{-3}$ and (4.7 ± 3.7) $\times 10^{-4}$ for ^{99m}Tc and ^{111}In respectively.), no crosstalk present (Mean (8.96 ± 5.36) $\times 10^{-4}$ and (3.1 ± 1.6) $\times 10^{-4}$ for ^{99m}Tc and ^{111}In respectively.) and no crosstalk compensation (Mean (2.76 ± 0.84) $\times 10^{-3}$ and (4.4 ± 3.0) $\times 10^{-4}$ for ^{99m}Tc and ^{111}In respectively.) based reconstructed data sets respectively is evident from the Figure 3.3(f). It also appears that the Sim-OSEM reconstruction produces a more uniform background appearance compared to TEW scatter compensation.

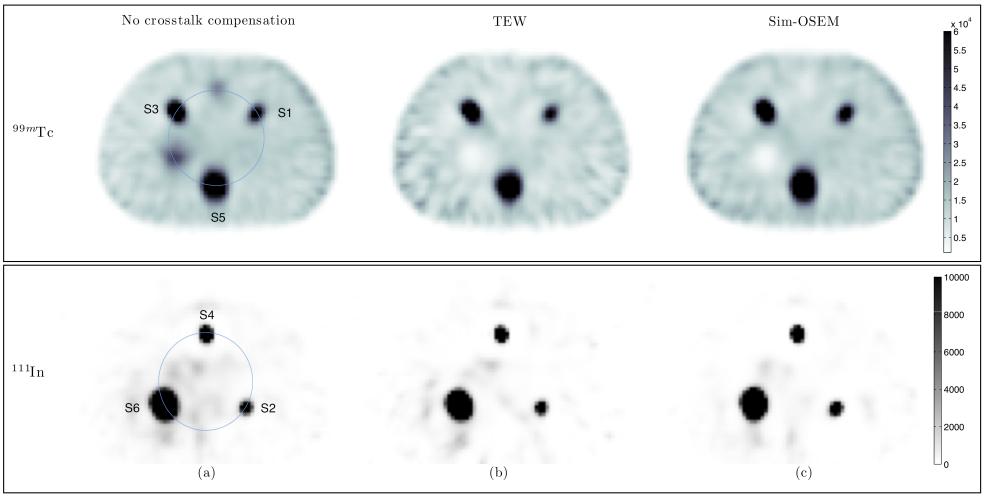

Figure 3.6: Infinia Experiment warm ^{99m}Tc background: Top row) Reconstructed images for ^{99m}Tc using different reconstruction algorithms. Bottom row) Reconstructed ^{111}In images from the same reconstruction methods. (a) is the image reconstructed without crosstalk compensation, (b) image reconstructed using TEW based crosstalk correction with the help of conventional analytical reconstruction method and (c) image reconstructed using Sim-OSEM.

3.2.3 Experimental Results

The images reconstructed from experimental phantom data acquired (hot spheres in cold background) using the GE Infinia dual head SPECT/CT camera are shown in Figure 3.4. Similar to simulation studies, improved contrast and more uniform background is observed in the ^{99m}Tc image for the Sim-OSEM based reconstruction (Figure 3.4d). Similar results can also be seen in case of ^{111}In. The results of the proposed method of reconstruction appear to be superior in terms of better contrast and more uniform background compared to reconstruction of separately acquired data for each isotope, again, likely due to the lack of scatter compensation for the alternative reconstruction processes.

For the case of warm ^{99m}Tc background, similar results can be seen in Figure 3.6. It can be seen in the bottom Figure 3.6(c) that the ^{111}In image has improved contrast and more uniform background for the case of Sim-OSEM reconstruction compared to TEW. In the case of warm ^{99m}Tc background, not only more uniform activity deposition in background and spheres as well as better contrast is evident in ^{99m}Tc image for Sim-OSEM compared to TEW, as can be seen from top Figure 3.6. Figures 3.5 and 3.7 depict circular profiles through the central region of the ^{99m}Tc and ^{111}In images shown in Figures 3.4 and 3.6 respectively on both linear and logarithmic scales. All the data sets for experimental studies, like simulation study, have been normalized with respect to their global maxima in order to compare the reconstruction results. These profiles show reduced background for Sim-OSEM compared to other methods similar to simulation results.

The PVR values were also calculated for experimental data using Equation 3.8. The PVR values for data reconstructed from acquisition in cold background are shown in Figure 3.5(e) and indicate superiority of Sim-OSEM (PVR (2.64 $\pm$ 0.13) $\times 10^3$ to (1.1 $\pm$ 0.9) $\times 10^4$) in terms of contrast to TEW (PVR (2.03 $\pm$ 0.24) $\times 10^2$ to (1.45 $\pm$ 0.13) $\times 10^3$, no crosstalk present (PVR (3.11 $\pm$ 0.36) $\times 10^2$ to (3.6 $\pm$ 1.3) $\times 10^3$) and with no crosstalk compensation (PVR (3.34 $\pm$ 0.34) $\times 10^2$ to (4.59 $\pm$ 0.31) $\times 10^2$) reconstructed ^{99m}Tc images respectively. The improvement in case of Sim-OSEM similar to ^{99m}Tc images is also evident for ^{111}In except the larger diameter sphere S6, which shows slightly better contrast in case of TEW compared to Sim-OSEM. The reduction in background scatter in terms of mean content of normalized data sets using VOI described in Section 3.2.2 was compared and shown in Figure 3.5(f). Sim-OSEM

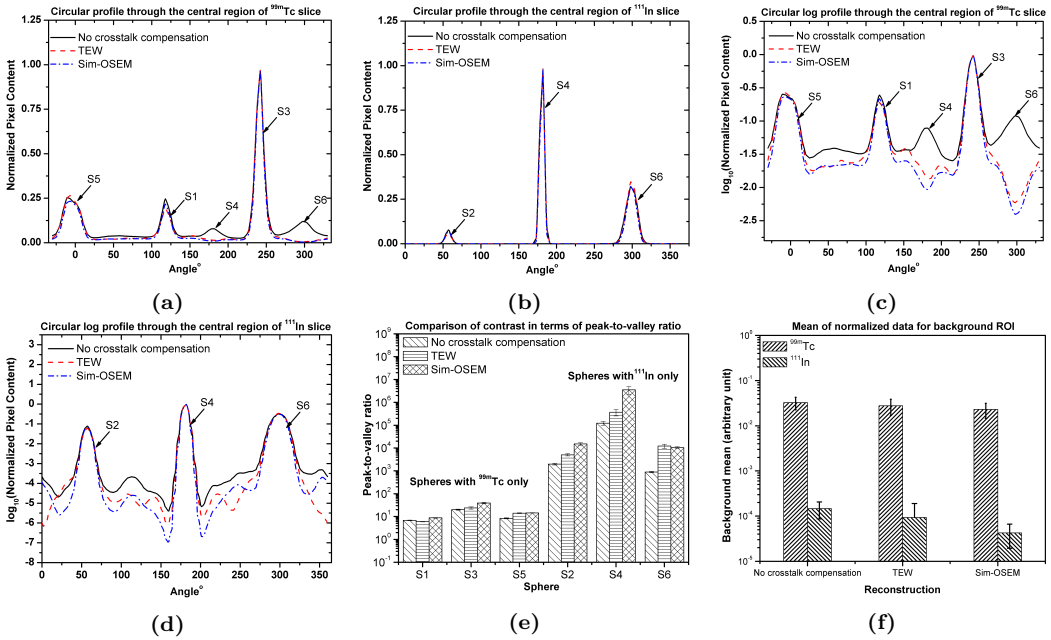

Figure 3.7: Infinia Experiment warm ^{99m}Tc background: Circular profiles through the central regions (indicated by blue circles in Figure 3.6) of the reconstructed image slices shown in Figure 3.6 for experimental data in warm ^{99m}Tc background. (a) and (b) shows the respective profiles through the central region of normalized pixel values for ^{99m}Tc and the ^{111}In image in Figure 3.6 with corresponding profiles on log scale are shown in (c) and (d). (e) shows the peak-to-valley ratios in case normalized reconstructed data sets. Top (f) depicts the standard deviation in voxel contents in background VOI in case of normalized ^{99m}Tc data sets, whereas mean voxel content in case of normalized ^{111}In data sets is shown in bottom (f).

(mean $(1.4 \pm 1.8) \times 10^{-5}$ and $(3.8 \pm 3.0) \times 10^{-5}$ for ^{99m}Tc and ^{111}In respectively.) seems superior to TEW (mean $(5.36 \pm 2.94) \times 10^{-4}$ and $(1.5 \pm 0.9) \times 10^{-4}$ for ^{99m}Tc and ^{111}In respectively.), no crosstalk present and $(1.5 \pm 0.9) \times 10^{-4}$ for ^{111}In) and no crosstalk compensation (mean $(6.6 \pm 3.5) \times 10^{-4}$ and $(1.5 \pm 0.9) \times 10^{-4}$ for ^{99m}Tc and ^{111}In respectively.) data respectively as evident from the Figure 3.5(f). Even no crosstalk present data show slightly higher background $(0.7 \pm 1) \times 10^{-4}$) compared to Sim-OSEM in case of ^{99m}Tc.

In the case of warm ^{99m}Tc background the Sim-OSEM (8.7 ± 0.3 to 39.4 ± 2.6) shows better contrast compared to TEW (5.9 ± 0.2 to 24 ± 2) and no crosstalk compensation (6.8 ± 0.2 to 20.1 ± 1.2) in case of respective ^{99m}Tc images can be seen in Figure 3.7(e). In case of ^{111}In the contrast similar to the the cold background acquisition is evident from Figure 3.7(e). The standard deviation of voxel content in normalized ^{99m}Tc reconstructed data is shown in top Figure 3.7(f). More uniform background in case of Sim-OSEM compared to other reconstructed data sets is evident

from Figure 3.7(f) for ^{99m}Tc images. The reduced background scatter in case of ^{111}In is also evident from Figure 3.7(f).

3.2.4 Activity Estimation

While not the purpose of this work, we have nevertheless determined accuracy values for activity quantitation for the simulations and experiments performed. Table 3.3 shows the total determined activity over the entire FOV for both simulation exercises and experimental data. In general, errors are within $0.1 - 7.6\%$ of the true total activity, with an apparent bias towards underestimation. However, in the experiment with warm ^{99m}Tc background, the Sim-OSEM methods tends to overestimate the amount of ^{99m}Tc present. The exact reason for this overestimation is presently under investigation.

Table 3.3: Comparison of actual injected and estimated activities using Sim-OSEM within reconstructed images.

		Activity (MBq)		
Acquisition	**Isotope**	**Deposited**	**Estimated**	**Error (%)**
MC Simulation	^{99m}Tc	7.75	7.73	-0.3
	^{111}In	7.56	7.57	0.1
^{99m}Tc/^{111}In in cold background	^{99m}Tc	5.40[a]	5.13[b]	-5.0
	^{111}In	6.70	6.19[b]	-7.6
^{99m}Tc/^{111}In in ^{99m}Tc background	^{99m}Tc	118.0[a]	131.1[b]	11.1
	^{111}In	6.70	6.57[b]	-2.0

[a] activity values after decay correction.
[b] activity values after sensitivity correction.

Reconstructed activity concentration values for the simulation study for each sphere along with percent (%) error are shown in Table 3.4. As expected, larger errors in the reconstructed activity concentration are present for smaller volumes due to the lack of partial volume correction. It should be noted that VOI selection was based on the actual volume of the spherical sources and does not take into account blurring effects in the reconstruction, thus it would be likely to underestimate activity values [107, 130].

These results indicate that, even for the case of a mis-matched projector/backprojector pair, quantitative accuracy is maintained by the Sim-OSEM method. Quantitative results were not evaluated for experimental data due to the lack of a calibration source for use with other reconstruction methods.

Table 3.4: Comparison of actual and VOI based estimation of mean activity concentration values for the images reconstructed using Sim-OSEM from simulated projection data.

Isotope	VOI	Activity Concentration (kBq/cc)			
		Volume	Actual	Reconstructed Mean	% Error
^{99m}Tc	S1	2.94 ml	151.1	56.2	-62.8
	S3	10.19 ml	151.1	118.4	-21.6
	S5	38.17 ml	151.1	148.2	-1.9
^{111}In	S2	1.55 ml	301.9	129.4	-57.1
	S4	5.53 ml	301.9	222.1	-26.4
	S6	17.96 ml	301.9	302.4	0.2

3.3 Discussion

We have developed a reconstruction method for simultaneous dual-isotope SPECT using an accelerated Monte Carlo projector. It differs from the joint iterative reconstruction method proposed by Ouyang *et al* [93] in that scatter and crosstalk estimates are obtained at each iteration in the reconstruction process, and so is continually refined throughout the reconstruction procedure. It should also be noted that compared with crosstalk correction using artificial neural networks and independent component analysis, Sim-OSEM only requires the PEW data for reconstruction rather than data acquired using multiple energy windows. Sim-OSEM took approximately 3-5 hours for reconstruction of 120 projections of size of 128×128, using 30 subsets and 2 iterations on a single CPU 2.66 GHz Intel Core i5 processor. It is expected that significant increases in speed are possible by applying further variance reduction techniques called multi-projection sampling (MPS) [29] or with relatively simple parallel processing techniques. It should also be noted that, for the simulation studies, a SIMIND-CFD based forward projector was used for both the data acquisition and subsequent reconstruction using Sim-OSEM. Even though good agreement between SIMIND-CFD and experimentally acquired data has been reported previously [29], further tests are planned in order to

validate the scatter model in SIMIND-CFD and to perform simulation studies using different MC based forward projectors such as GATE.

Differences seen between experimental and SIMIND-CFD sensitivity values seen in Table 3.1 was compensated by applying an sensitivity correction factor of 1.1 for ^{111}In to Monte Carlo projections. We expect this to be caused by septal penetration increasing the counts in experimental data. As noted, this effect has not been modeled in the present Sim-OSEM implementation, although we have developed a technique to model this effect [82]. A slight increase in the NMSE values with increasing depth of point source in water is evident from Table 3.2. This may be caused by lower counts, and hence higher noise level, at larger source depth in case of GATE based projection data due to fixed acquisition time. Also, slightly larger values of NMSE at a source depth of 5 cm in Table 3.2 may indicate a more significant contribution from collimator scatter in the overall scatter contribution detected within the PEW at this depth.

As can be seen in Figure 3.3, there appears to be a slight improvement in spatial resolution in Sim-OSEM compared to other techniques, presumably due to better correction of small angle photon scattering. These small angle scatters are detected under the PEW due to the relatively poor energy resolution of NaI(Tl) (9.8% in our case) and may result in slight spatial resolution degradation if not compensated properly. As Sim-OSEM uses a more realistic MC based scatter correction, these photons are modeled and so may be removed from the reconstructed image, thus resulting in slightly improved spatial resolution in the final reconstructed image. However, a quantitative assessment on the improvement in resolution due to improved small angle scatter and crosstalk correction is required to justify the claim.

3.4 Conclusion

In this work, we have introduced a Monte Carlo-based reconstruction method, Sim-OSEM, which has shown some promising results in separating the images in simultaneously acquired dual-isotope, namely ^{99m}Tc and ^{111}In, SPECT by correcting the crosstalk between the isotopes. While both triple energy window (TEW) and Sim-OSEM provide higher contrast and reduction of crosstalk artifacts compared to no scatter compensation, the proposed Sim-OSEM technique yields slightly better crosstalk correction compared to the TEW method. Sim-OSEM also performs reasonably accurate activity estimation, although a rigorous analysis of quantitation with multiple noise realizations

was not performed here. Further studies in order to quantitate the scatter correction and possible improvement in SNR and spatial resolution are required and are presently being performed. While it appears the Sim-OSEM method may improve image contrast and reduce crosstalk contamination, a more rigorous ROC study is planned to evaluate the exact impact of the Sim-OSEM method on lesion detection.

Chapter 4

Accelerated Monte Carlo based Simultaneous ^{99m}Tc/^{123}I SPECT Reconstruction for Molecular Breast Imaging

Published in Proceedings of IEEE Imaging Conference© 2012, Pages:3337-3343, 2012

Note: content is modified for consistency

ESTROGEN receptor (ER) status is an important parameter in prediction of patient prognosis and in decisions about hormonal treatment in patients with metastatic breast cancer. Clinical studies involving *in vivo* estrogen receptor SPECT have shown that ^{123}I labelled *cis*-11β-methyoxy-17α-iodovinyl estradiol (Z-MIVE) is a sensitive noninvasive tool for detection of ER in patients with breast cancer ([131–133]). ^{99m}Tc-sestamibi is commonly used for scintimammography with high sensitivities for benign and malignant lesions. In dual isotope SPECT studies using ^{123}I labelled Z-MIVE and ^{99m}Tc-sestamibi, ^{123}I labelled Z-MIVE not only detects the presence of ER but also thought to complement ^{99m}Tc-sestamibi in differentiating between benign and malignant breast lesions in patients with breast cancer. Scanning the two radionulides, ^{99m}Tc and ^{123}I, separately not only increases the patient discomfort but also results in the misregistration of images, caused by patient motion. Therefore in order to

improve system throughput, reduce patient discomfort and to avoid misregistration, simultaneous acquisition of both the radionuclides is the option. The major concern in simultaneous dual isotope SPECT is the significant crosstalk contamination between the two isotopes used. In order to understand the severity of cross-contamination issue in simultaneous dual isotope SPECT, 3.2×10^7 photons were simulated for a source (radius = 0.88 cm) containing ^{99m}Tc and ^{123}I in equal amounts, placed at the center of a non-radioactive water filled cylinder (radius = 14 cm, height= 28 cm). The spectrum obtained for energy resolutions of 9.8% (Thallium activated Sodium Iodide NaI(Tl) detector) and 5% (Cadmium Zinc Telluride (CZT) detector) at 140 keV respectively as shown in Figure 1. At 9.8% and 5% energy resolution about 20% and 14% of the counts collected within the ^{99m}Tc photopeak were actually down-scattered from ^{123}I respectively. However spillover was negligible that is about 0.04% at 5% energy resolution compare to about 6% at energy resolution of 9.8%. It should be noted that in order to avoid overlap of acquisition windows calculations were performed for asymmetric primary energy windows that is 126-150 keV and 151-175 keV for ^{99m}Tc and ^{123}I respectively.

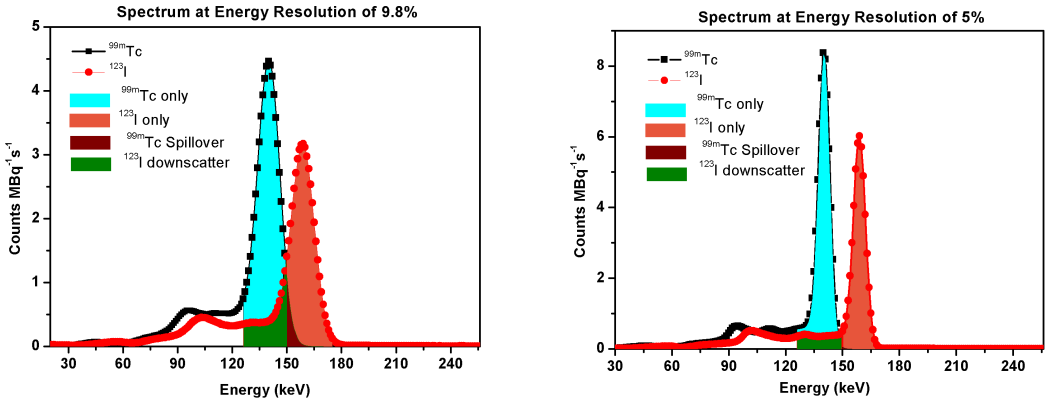

(a) (b)

Figure 4.1: Energy spectrum for ^{99m}Tc and ^{123}I. Spill over of ^{99m}Tc into ^{123}I window and contamination of ^{123}I into ^{99m}Tc at energy resolutions of (a) 9.8% (NaI(Tl)) and (b) 5% (CZT).

Many researchers have previously developed different pre-reconstruction crosstalk compensation methods, which involved subtraction of crosstalk estimate or restoration by deconvolution of crosstalk blurring function (e.g., [115–117]). Some proposed model based crosstalk compensation methods in dual isotope SPECT applied during reconstruction (e.g., [120–122]). More recent approaches used for crosstalk compensation in simultaneous mutli-isotope SPECT, involved the use of artificial neural networks (e.g.,

[124, 125]) and independent component analysis [126]. These techniques are very good at compensating for the crosstalk. However the major limitation in these methods is the large number of energy windows required, whereas commercially available systems provide only 3-8 energy windows.

The current study focuses on a method of crosstalk compensation between two isotopes in dual isotope SPECT imaging, developed by us, applied to simultaneous breast SPECT using ^{99m}Tc and ^{123}I. Monte Carlo (MC) based scatter compensation is thought to offer the most realistic crosstalk and scatter compensation modelling. However, in typical implementations, the inherent long calculation times (often several hours or days) associated with this technique makes it unsuitable for clinical applications. This is mainly due to low detection efficiency MC base SPECT simulation programs [27]. While the advent of ever increasingly fast computers has reduced the computation times, we have taken an alternative approach to improve simulation times. Our group has previously incorporated convolution based forced detection (CFD) into SIMIND Monte Carlo program which have made MC feasible to use in clinical time frames [29]. We have developed an iterative Monte Carlo-based image reconstruction technique that simulates the photon downscatter from one isotope into the acquisition window of a second isotope. By accurately modeling the photon transport through the object of interest using MC, we can accurately estimate the amount of scatter contamination contained in a given projection view. Once known, we then use this information in an iterative algorithm to compensate for the photon contamination. We use a modified ordered subset-expectation maximization (OS-EM) [128], we named it as simultaneous ordered subset-expectation maximization (Sim-OSEM) to perform this step.

4.1 Materials and Methods

MC based scatter compensation is thought to offer the most realistic crosstalk compensation was used in this study for crosstalk between the two isotope involved that is ^{99m}Tc and ^{123}I. However, in typical implementations, the inherent long calculation times (often several hours or days) associated with this technique makes it unsuitable for clinical applications. Our group has previously developed a number of different variance reduction techniques (VRT) that have made Monte Carlo-based crosstalk compensation feasible to use in clinical time frames. Accelerated SPECT Monte Carlo simulation using convolution based forced detection (CFD), is being used to accelerate

the Monte Carlo photon transport modelling [29].

4.1.1 Data acquisition

In simulation SPECT studies the projection data acquired using MC for both the isotopes (x and y) simultaneously and can be represented by the linear Equations 4.1 and 4.2.

$$H_{xx}f_x + H_{yx}f_y = p_x \tag{4.1}$$

and

$$H_{xy}f_x + H_{yy}f_y = p_y \tag{4.2}$$

where H_{xx} and H_{yy} are the photopeak photon geometric system matrices for each respective isotope, H_{yx} and H_{xy} are the scatter photon system matrices for the isotope y (or x) into the acquisition window for isotope x (or y).

In order to simulate dual-isotope imaging for breast cancer, a mathematical breast phantom was developed. Three different breast sizes, small, medium and large, were modelled. The breast soft tissue was modelled as half ellipsoid with semi spherical nipple [134] as shown in Figure 4.2. Table 4.1 shows the length of semi axis and tilt

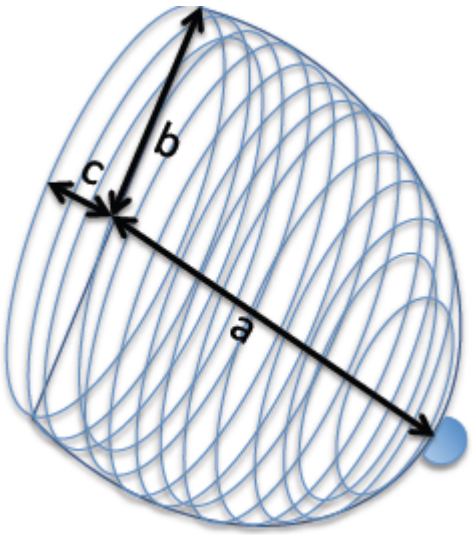

Figure 4.2: Breast shape modelling as tilted half ellipsoidal breast and semi spherical nipple

introduced in the breast phantom [135]. In this case the coordinates (x, y, z) rotated at an angle θ were calculated from the standard Cartesian coordinates (x_o, y_o, z_o) using Equation set 4.3

Table 4.1: Parameters used in pixelated breast modelling of different sizes

	Semi-axis length (cm)			
Breast Size	**a**	**b**	**c**	**Tilt (θ)**
Small	4.0	4.0	4.0	10^o
Medium	6.5	5.5	5.5	7.5^o
Large	8.0	7.0	7.0	5^o

Table 4.2: Radii of spherical lesions used for different breast size phantoms

	Lesion	
Breast Size	**Radius (mm)**	**Number**
Small	2.4	5
	4.0	4
	5.6	4
Medium	3.3	5
	5.5	4
	7.7	4
Large	4.2	4
	7.0	4
	9.8	3
	12.6	2

$$\begin{aligned} x &= x_o^2 \\ y &= (y_o \cos\theta - (z_o - z_c)\sin\theta)^2 \\ z &= (-y_o \sin\theta + (z_o - z_c)\cos\theta)^2 \end{aligned} \tag{4.3}$$

In this case the center was taken at (0, 0, z_c) where z_c was taken in the middle of the imaging grid. With (x, y, z) values calculated using Equation set 4.3 half ellipsoid satisfy conditions given in inequality 4.4.

$$\frac{x^2}{a^2} + \frac{y^2}{b^2} + \frac{z^2}{c^2} \leq 1 \text{ and } z_o \geq z_c \tag{4.4}$$

For each breast size 13 spherical lesions of different sizes were randomly generated (described in Table 4.2). From the generated lesions 10 combinations for each breast size with 3 lesions per combination were selected randomly. For each of the randomly selected set of three lesions uniform activity of ^{99m}Tc, ^{123}I and both ^{99m}Tc & ^{123}I was

deposited respectively.

In this work low noise Monte Carlo-based projection data were acquired using SIMIND and modelling a low energy high resolution (LEHR) collimator with both NaI(Tl) and CZT detectors. 120 projections at matrix size of 128×128 were acquired for a total of 5×10^6 counts per study. In order to avoid overlap of primary energy windows, asymmetric primary energy windows (126-150 keV for ^{99m}Tc and 151-174.9 keV for ^{123}I) were used. 150 MBq activity uniformly distributed in total to give specific activity ratio between ^{99m}Tc background in breast soft tissue, ^{99m}Tc in lesions and ^{123}I as 1:5:10 respectively.

4.1.2 Reconstruction and activity estimation

We have developed an iterative MC based image reconstruction technique Sim-OSEM that simulates the photon down-scatter and spillover in case of overlapping full energy peaks, from one isotope into the acquisition window of a second isotope. We use a modified ordered subset-expectation maximization, Sim-OSEM to perform this step as given in Equations 4.5 and 4.6.

$$f_x^{new} = \frac{f_x^{old}}{\sum_{a\epsilon s} H_{a,x}^T} \sum_{a\epsilon s} H_{a,x}^T \frac{\bar{p}_{a,x}}{p_{a,x} R_x^{new} t_{acq}} \tag{4.5}$$

$$f_y^{new} = \frac{f_y^{old}}{\sum_{a\epsilon s} H_{a,y}^T} \sum_{a\epsilon s} H_{a,y}^T \frac{\bar{p}_{a,y}}{p_{a,y} R_y^{new} t_{acq}} \tag{4.6}$$

where $\bar{p}_x$ and $\bar{p}_x$ are the measured projection data for isotope $X =^{99m}$Tc and $y =^{123}$I respectively with $\bar{p}_{a,x}$ and $\bar{p}_{a,y}$ as corresponding measured projections respectively. Correspondingly, $p_{a,x}$ and $p_{a,y}$ denote the estimated projections acquired using respective Monte Carlo based forward projectors. Notice that in the forward projection step (denominator), there is an additional factor, $R_i^{new} t_{acq}$ with subscript i equal to either x or y. Because of the forced detection variance reduction technique used in CFD-MC, each detected count is scaled by the probability of detection in order to provide units of cps/MBq. Hence the list-mode projection data must be scaled to account for the actual acquisition times, t_{acq} and the absolute quantitative activity R_i^{new}. This scaling factor, R_i^{new} is determined through an iterative process based on the total number of counts acquired in the measured projection data, $\bar{p}_i$, and the MC simulated projection

as shown in Equations 4.7 and 4.8.

$$R_x^{new} = R_x^{old} \frac{\sum_{a \epsilon s} \bar{p}_{a,x}}{\sum_{a \epsilon s} (H'_{a,xx} f_x^{old} + H'_{a,yx} f_y^{old}) \times t_{acq}} \tag{4.7}$$

$$R_y^{new} = R_y^{old} \frac{\sum_{a \epsilon s} \bar{p}_{a,y}}{\sum_{a \epsilon s} (H'_{a,xy} f_{Tc}^{old} + H'_{a,yy} f_{In}^{old}) \times t_{acq}} \tag{4.8}$$

Where t_{acq} is acquisition time per projection in seconds. Figure 4.3 shows the flow chart diagram of Sim-OSEM based simultaneous dual isotope reconstruction.

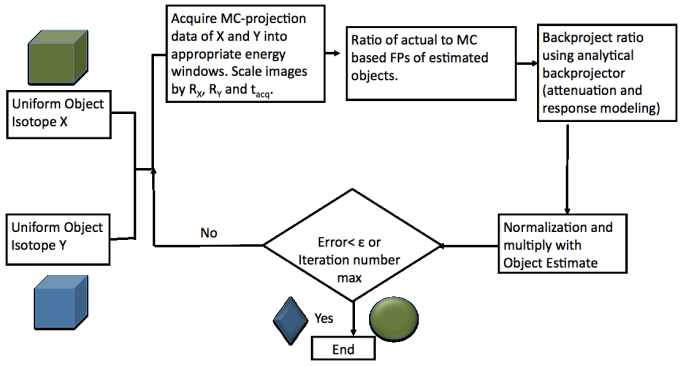

Figure 4.3: Flow chart diagram of Sim-OSEM based dual isotope image reconstruction.

Sim-OSEM based reconstructed images were compared to the images obtained using analytical attenuation based reconstruction of data uncorrected for crosstalk, and single isotope data without any crosstalk contribution from other isotope. Analytic attenuation based reconstruction uses analytical projector/backprojector pair incorporated into standard OSEM reconstruction algorithm that include attenuation and geometric collimator response modeling.

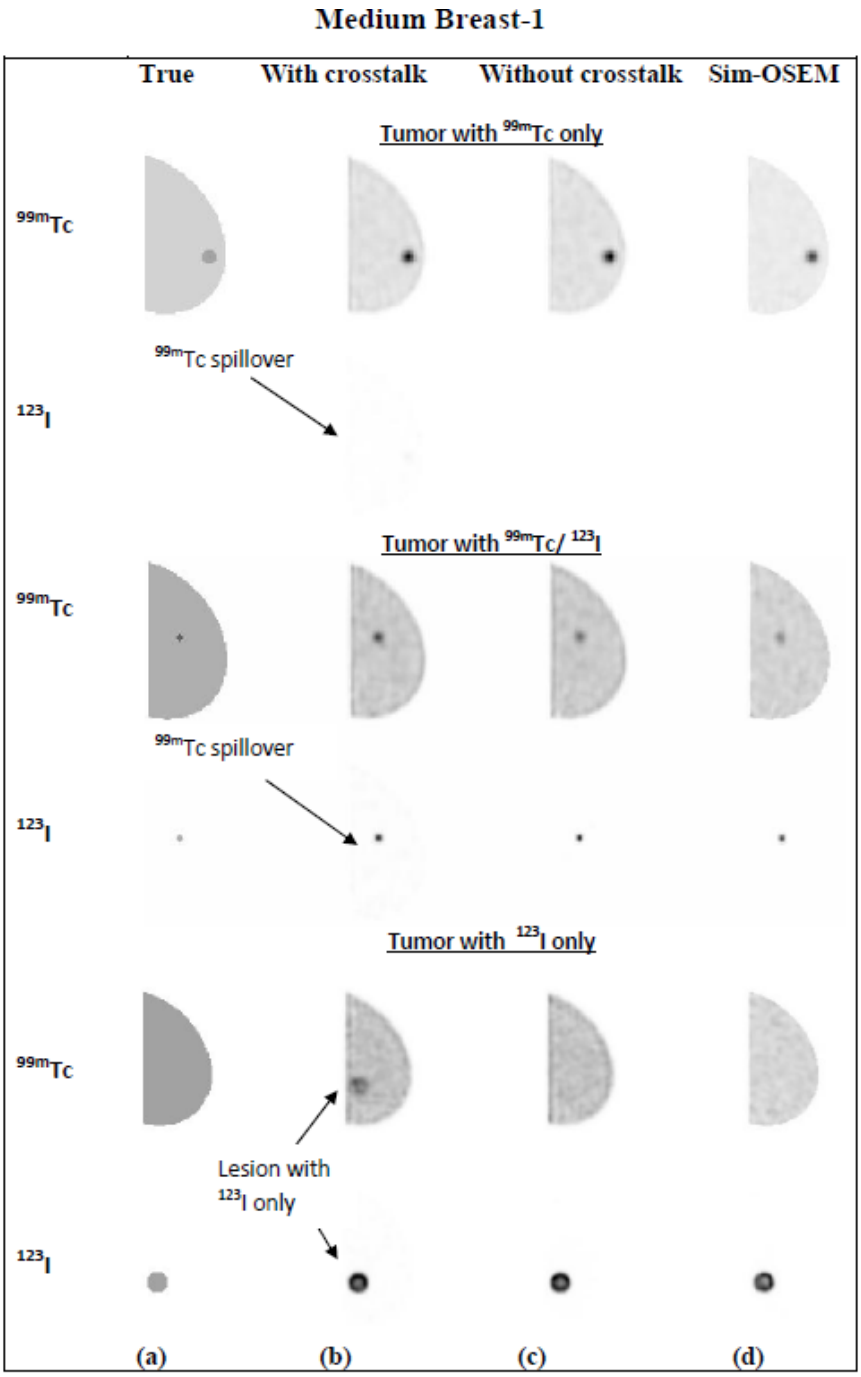

Figure 4.4: NaI(Tl) detector: At top, in the middle and at bottom are the slices through lesions with ^{99m}Tc only and with both ^{99m}Tc/^{123}I and ^{123}I only respectively (^{99m}Tc and ^{123}I shown on separate rows). (a) is the true image, (b) is the image reconstructed using conventional analytical reconstruction method without crosstalk compensation (c) image reconstructed using separately acquired data with no crosstalk using conventional reconstruction (d) image reconstructed using Sim-OSEM.

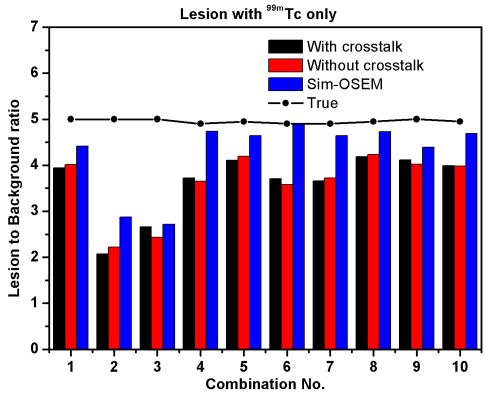

(a) Lesion to background ratios for lesions with ^{99m}Tc only

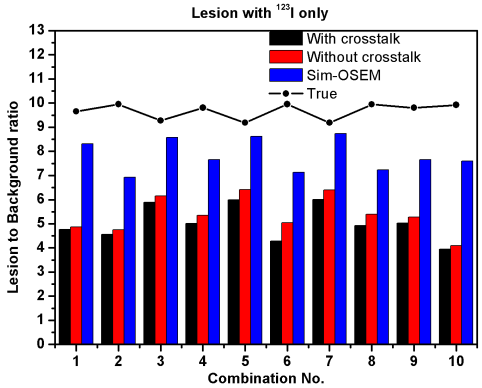

(b) Lesion to background ratios for lesions with ^{123}I only

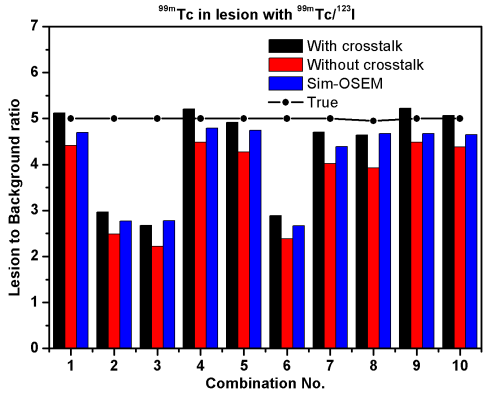

(c) ^{99m}Tc lesion to background ratios for lesions with ^{99m}Tc/^{123}I

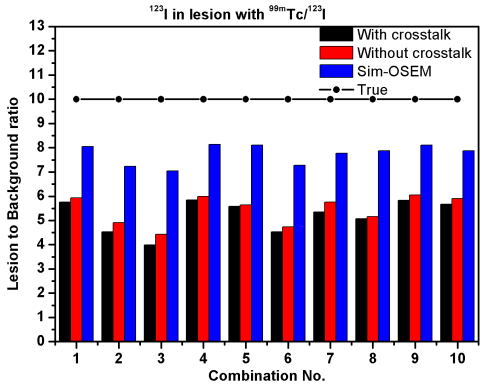

(d) ^{123}I lesion to background ratios for lesions with ^{99m}Tc/^{123}I

Figure 4.5: NaI(Tl) detector: A comparison of lesion to background ratios estimated for different reconstruction methods with the true values of lesion to background ratios in the case of small breast size.

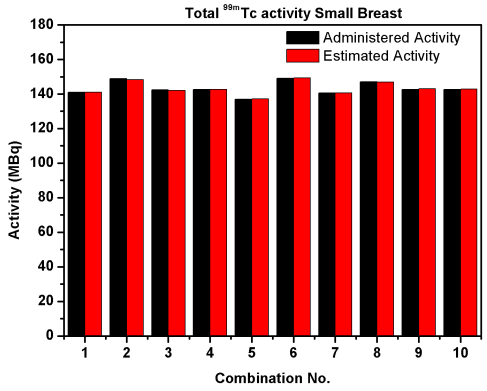

(a) Total ^{99m}Tc activity in small breast.

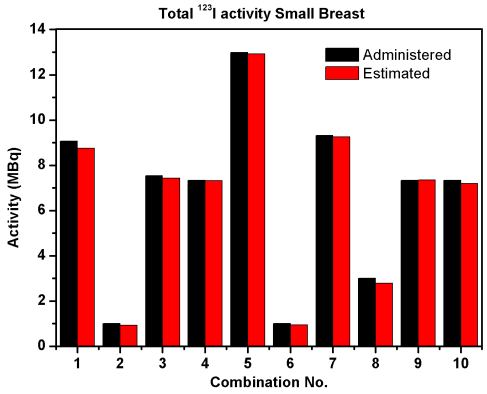

(b) Total ^{123}I activity in small breast.

Figure 4.6: NaI(Tl) detector: A comparison of total ^{99m}Tc and ^{123}I activity estimated using Sim-OSEM with actually administered activity for all the lesion combinations for small breast size.

4.2 Results

It has been mentioned previously that ^{123}I labelled Z-MIVE is thought to complement ^{99m}Tc-sestamibi in breast SPECT in order to distinguish between benign and potentially malignant lesions non-invasively [131]. In order to evaluate SPECT reconstruction of simultaneously acquired ^{99m}Tc/^{123}I projection data three different breast size phantoms with spherical lesions were designed. Details of the designed phantoms can be seen in Section 4.1.1. For each of the breast sizes (i.e. small, medium and large) three lesions were simulated with ^{99m}Tc only, both ^{99m}Tc/^{123}I and ^{123}I only respectively. Ten different combination of lesions with three lesions per combination were selected randomly for simulation of each of the breast sizes.

4.2.1 Energy Resolution 9.8% (NaI(Tl) detector)

For all the SPECT simulation studies performed in this work Sim-OSEM based reconstructed images were compared with the images obtained using analytical attenuation based reconstruction of data uncorrected for crosstalk, single isotope data without any crosstalk contribution from other isotope. In case of Sim-OSEM as well as analytical reconstruction algorithm, dual isotope reconstruction was performed using 30 subsets and 2 iterations. Figure 4.4 shows a representative example of medium breast size. The results shown in Figure 4.4 are slices through the different lesions in the images obtained from i) analytical attenuation based reconstruction of data uncorrected for crosstalk, ii) single isotope data without any crosstalk contribution from other isotope and iii) reconstruction using Sim-OSEM.

In order to compare different reconstruction methods used for breast data reconstruction, lesion to background ratios were calculated for all the lesion combinations for each of the breast sizes. Figure 4.5 shows graphical representation of lesion to background ratios for lesions with ^{99m}Tc only, ^{123}I only and both ^{99m}Tc/^{123}I respectively in the case of small breast size.

As described in Section 4.1.2 that estimation of deposited activity is also possible with our proposed Sim-OSEM based reconstruction method. Figure 4.6 shows comparison between actual administered activities to the activity values estimated using Sim-OSEM for all the lesion combinations simulated for small breast size. The percentage error in total activity values observed in case of NaI(Tl) detector was 0.02

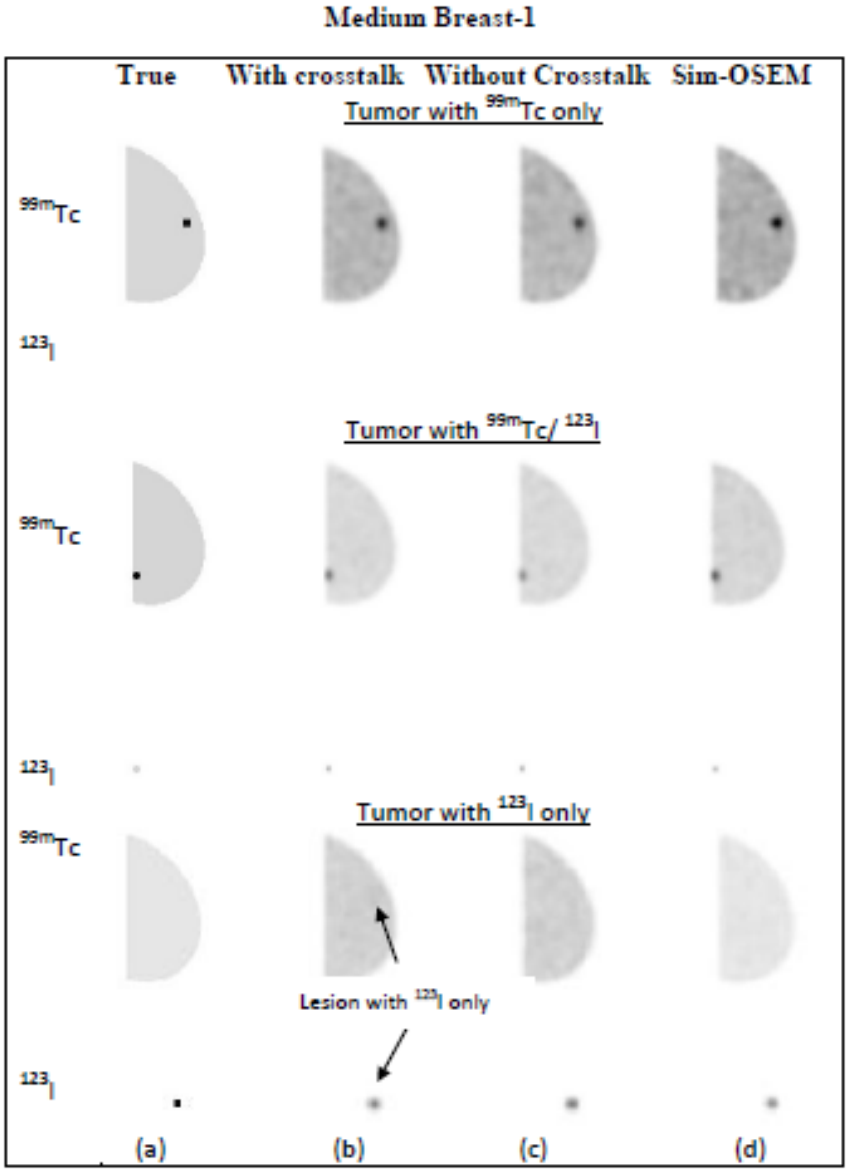

Figure 4.7: CZT Detector: At top, in the middle and at bottom are the slices through lesions with ^{99m}Tc only and with both ^{99m}Tc/^{123}I and ^{123}I only respectively (^{99m}Tc and ^{123}I shown on separate rows). (a) is the true image, (b) is the image reconstructed using conventional analytical reconstruction method without crosstalk compensation (c) image reconstructed using separately acquired data with no crosstalk using conventional reconstruction (d) image reconstructed using Sim-OSEM.

to 0.36% and 0.18 to 16.39% for ^{99m}Tc and ^{123}I respectively.

4.2.2 Energy Resolution 5% (CZT detector)

From the generated lesions 10 combinations for each of breast size with 3 lesions per combination were selected randomly for acquisition and reconstruction for each of the breast sizes in case of CZT detector. Similar reconstruction algorithms as described in case of NaI(Tl) detector in Section 4.2.1 were used in case of CZT.

A representative example of medium breast size in case of CZT detector is shown in Figure 4.7. The results shown in Figure 4.7 are slices through the different lesions in the images obtained from i) analytical attenuation based reconstruction of data uncorrected for crosstalk, ii) single isotope data without any crosstalk contribution from other isotope and iii) reconstruction using Sim-OSEM.

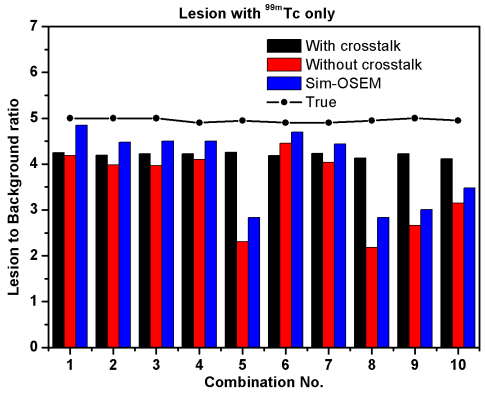

(a) Lesion to background ratios for lesions with ^{99m}Tc only

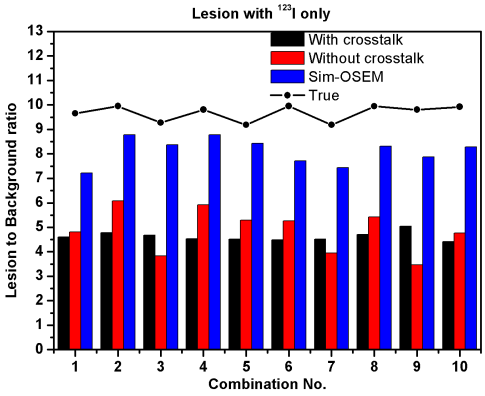

(b) Lesion to background ratios for lesions with ^{123}I only

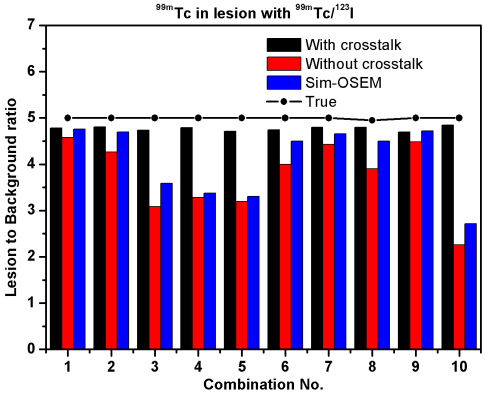

(c) ^{99m}Tc lesion to background ratios for lesions with ^{99m}Tc/^{123}I

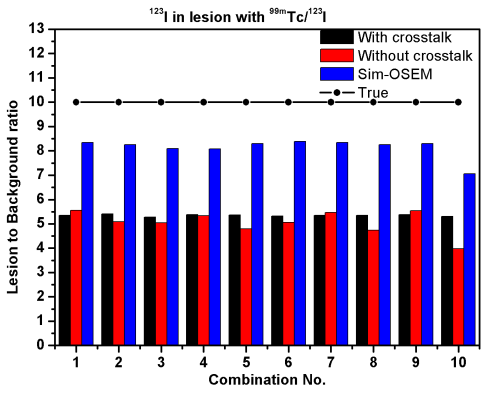

(d) ^{123}I lesion to background ratios for lesions with ^{99m}Tc/^{123}I

Figure 4.8: CZT Detector: A comparison of lesion to background ratios estimated for different reconstruction methods with the true values of lesion to background ratios in the case of small breast size.

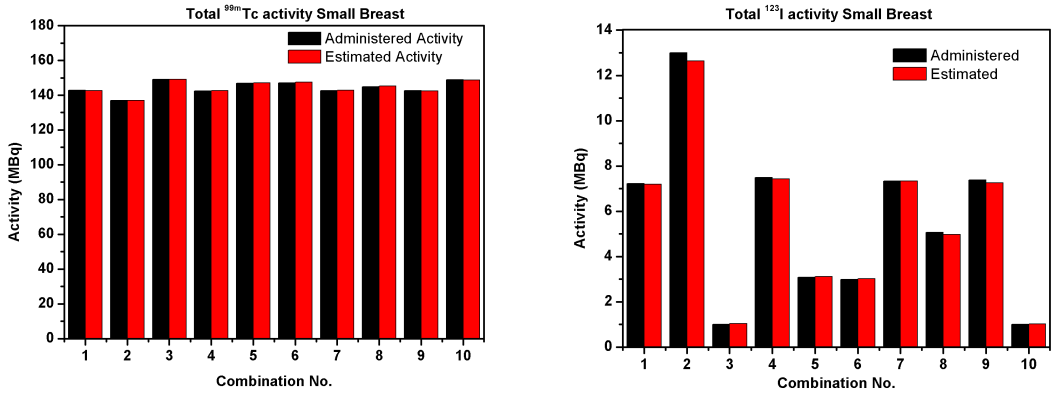

(a) Total ^{99m}Tc activity in small breast.

(b) Total ^{123}I activity in small breast.

Figure 4.9: CZT Detector: A comparison of total ^{99m}Tc and ^{123}I activity estimated using Sim-OSEM with actually administered activity for all the lesion combinations for small breast size.

Figure 4.8 shows comparison of different reconstruction methods in terms of lesion to background ratios, calculated for all the lesion combinations for each of the breast sizes in case of CZT.

A comparison between administered and estimated total activities using Sim-OSEM in case of CZT is shown in Figure 4.9. The percentage error in activity values observed in this case was 0.03-0.26% and 0.41-14.23% for ^{99m}Tc and ^{123}I respectively.

4.3 Discussion

We have developed a reconstruction method, which realistically corrects for crosstalk as well as scatter in simultaneous multi-isotope SPECT different from fast Monte Carlo based joint iterative reconstruction method used by Ouyang *et al* [93]. In the method proposed by Ouyang *et al* scatter and crosstalk corrections applied on the images reconstructed using standard OS-EM for number of iteration without scatter correction at first, then on images reconstructed with scatter correction and finally on images reconstructed jointly using joint OS-EM (JOSEM). It should also be noted that compare to crosstalk correction using artificial neural networks and independent component analysis, Sim-OSEM requires only primary energy window data for reconstruction rather than data acquired using multiple energy windows.

It can be seen from Figure 4.4 that Sim-OSEM based reconstruction gives images comparable to crosstalk-free single isotope reconstructed images. In most of the cases Sim-OSEM based reconstruction gives even better images when compared

with crosstalk-free single isotope images reconstructed using analytical attenuation correction based reconstruction method. This may be due to the fact that the MC based forward projector corrects for the photons scattered at small angles and detected under the photo peak.

From Figure 4.5 and Figure 4.8 it can be seen that the Sim-OSEM gives much better and much more realistic lesion to background ratios when compared with those for images reconstructed using attenuation based analytical reconstruction. It should also be noted from the Figure 4.5(c) and Figure 4.8(c) that in case of lesion with both ^{99m}Tc/^{123}I show higher lesion to background ratios for ^{99m}Tc when images reconstructed without crosstalk correction. This may be due to downscatter from ^{123}I. This is also evident from Figure 4.8(c) where ^{99m}Tc lesion to background ratios are comparatively lower than those shown in Figure 4.5(c) for NaI(Tl) detector when images reconstructed without crosstalk correction. It can also be seen from the Figure 4.6 and Figure 4.9 that the Sim-OSEM gives quite accurate estimates of total activities. However, due to the involvement of smaller activities relatively larger percentage error in activity values for ^{123}I was observed in case of both NaI(Tl) and CZT. It can also be seen from Figure 4.7, which shows an example of medium breast size that the effect of downscatter is reduced by the use of better energy resolution detector like CZT but still needs to be corrected using Sim-OSEM in order to get crosstalk-free images.

4.4 Conclusion

In this work, we have introduced a MC based reconstruction method, Sim-OSEM. The simulation studies performed in this work have shown that Sim-OSEM not only corrects the crosstalk between the isotopes in simultaneous ^{99m}Tc and ^{123}I SPECT but performs activity estimation as well. It has also been shown that using the higher resolution detector like CZT reduces the crosstalk between the isotopes significantly in case of simultaneous ^{99m}Tc/^{123}I SPECT but downscatter from ^{123}I still needs to be corrected using Sim-OSEM.

Chapter 5

Quantitative Maximum A-Posteriori SPECT Reconstruction using Accelerated Convolution-based Forced Detection Monte Carlo and CT-based Anatomical Prior

Submitted for publication in IEEE Transactions on Nuclear Science©, 2016

SINGLE photon emission computed tomography (SPECT) imaging has always been regarded as a highly sensitive modality with a limited quantification accuracy and relatively poor image quality. The image quality and quantification accuracy is affected by physical factors like a) a loss of photons due to photoelectric absorption and scatter within the patient's body (i.e. attenuation), b) contamination of the detected photons due to the scattered photons, either emitted from the patient's body or scattered within the collimator, that remain available for detection, and c) spatial resolution or partial volume effects (caused either by the detection system and collimator or limited voxel size in the image domain). Therefore, correction of these factors is necessary for obtaining better image quality and improved quantification [37,

38].

Considerable effort has been made to develop methods that perform attenuation compensation either a) in the image domain or b) during the analytical or iterative reconstruction process. The Chang algorithm [51], once the most commonly used attenuation correction method clinically [37, 38], is used to perform post filtered backprojection reconstruction attenuation correction. In this method an attenuation correction factor (ACF) averaged over number of projections is used to perform attenuation compensation on the image reconstructed using FBP. An analytic solution of the attenuated Radon transform in case of non uniform attenuation has also been proposed. A description of these FBP based attenuation correction methods is beyond the scope of this article and related references can be found in [37].

Accurate determination of the attenuation map is critical in performing the attenuation correction. With the availability of hybrid SPECT/CT systems, CT-based attenuation map determination is now becoming a standard clinical protocol [38]. However, comparatively much shorter CT data acquisition times, the presence of metal implants and/or CT contrast agents may affect the accuracy of these attenuation maps [37, 38].

Among many advantages of iterative reconstruction methods is the flexibility to involve attenuation modeling and other image degradation effects into the transition system matrix [37, 52].

Due to the limited energy resolution of the most commonly used NaI(Tl) detector ($\approx$10%) in gamma camera, significant image degradation is caused by the scattered photons detected in the photopeak energy window (PEW) [37]. The methods to correct for scatter detected under PEW can be categorized as a) Energy spectrum based methods, b) Scatter distribution based scatter estimation and correction and c) Reconstruction based scatter correction methods [37, 38, 58]. Scatter compensation in the projection or the image domain can be performed either by subtraction of a scatter estimate or restoration through deconvolution of an approximate spatial scatter distribution function.

The energy-distribution based methods involve scatter estimation in a pixel and subsequent subtraction from photopeak data that generally requires acquisition of additional energy windows (e.g. [59–62]). The triple energy window (TEW) based scatter compensation method is an example of these methods [60, 61]. The TEW based compensation method uses two narrow energy windows adjacent to each of the

PEW's in order to determine scatter contribution within the PEW. In order to obtain the scatter contribution S_j in a given PEW for the jth pixel Equation 5.1 can be used.

$$S_j = \left(\frac{C_{l,j}}{W_l} + \frac{C_{u,j}}{W_u}\right) \frac{W_l + W_u}{2} \tag{5.1}$$

where, W_l and W_u are the window widths of scatter windows below and above the PEW respectively, and $C_{l,j}$ and $C_{u,j}$ are the total number of counts collected in the jth pixel of corresponding scatter windows respectively. The energy window based scatter correction methods have the advantage of being simple, speedy and easy to implement [37, 58]. An undesired noise amplification and approximative scatter estimation are the disadvantages that may be associated with these methods [37, 58].

More recent spectral distribution based scatter correction methods involve spectral fitting (e.g. [63]), factor analysis (e.g. [64, 65]) and the use of artificial neural networks (e.g. [64, 66, 67]). These methods offer to provide accurate scatter compensation but, require either a list mode or multiple-energy window (often $\geq$10) based data acquisition [37, 58, 68]. Neither access to the list mode data nor required number of multiple-energy window acquisition facilities are currently available on most of the commercially available SPECT imaging systems [37, 58].

Modeling of the scattered photons within the PEW by some scatter function based either on a line source measurements (e.g. [69, 70]) or an individualized patient based transmission point spread function (PSF) through the attenuation map (e.g. [71, 72]) form the basis of convolution-subtraction methods.

The methods that involve inclusion of a scatter model into the system matrix can be categorized as reconstruction based scatter correction methods (RBSC) (e. g. [79, 80]). These methods make use of all the detected photons and therefore result in a lesser noise compared to convolution subtraction and energy window based methods [37]. Effective scatter source estimation (ESSE) method that has been refined for Compton scatter correction is an example of RBSC methods [74, 77, 78]. The Monte Carlo (MC) methods are expected to provide accurate estimates of the scatter compared to other more approximative methods. Individualized patient-based scatter estimation, using MC, has always been considered computationally too demanding to be practical with iterative RBSC methods [58]. The problem with these notoriously slow MC methods is their inherent low detection efficiency in SPECT simulation studies [27]. In order to address this issue, a variance reduction technique (VRT), known as convolution forced

detection (CFD) [81], has previously been incorporated into SIMIND Monte Carlo Program (CFD-SIMIND) by our group with [29] and without [82] detailed collimator scatter and septal penetration modeling. CFD implementation generates low-noise projections often within a minute of acquisition time [29, 81]. In this VRT, a weighted copy of each photon at each interaction site is forced in a direction that is perpendicular to the gamma camera head while convolving it with a distance-dependent collimator response kernel modeled as Gaussian [29, 81]. We have shown very good agreement between our simulation methods and experimental data for simple phantoms [29, 82]. A systematic study to evaluate the accuracy of our approach compared to GEANT-4 based MC code GATE has also been performed [136]. The study has shown that the GATE and CFD-SIMIND match well (with sensitivity difference of $3-5\%$ and spatial resolution within 0.2 mm for point source depth of $0-250$ mm) for the isotopes with low and medium energy gamma emissions.

This CFD-based accelerated MC forward projector has successfully incorporated previously into an iterative reconstruction framework to correct for scatter and crosstalk between the isotopes in simultaneous dual-isotope SPECT [83–86]. With the inclusion of attenuation-map information, CFD-SIMIND based forward projector performs accurate compensation of the attenuation and scatter during reconstruction [85, 86].

Figure 5.1 depicts the effect of geometric response of the collimator on a 40 cm wide rectangular activity profile that is spread over several pixels/sampling bins. This effect causes spill-in and spill-out effect among the neighboring voxels. Depending on the size of the object, relative activity concentration and sampled voxel size in the image either spill-out or spill-in effect becomes dominant. It is important to note in this depiction that both the profiles have same area under the curve. The correction or compensation of collimator response effects can broadly be divided into three possible categories as, a) image enhancement (during or post reconstruction) with resolution modeling and/or anatomical priors, b) image domain-based e.g. [48] and c) projection domain-based methods (e.g. [49, 50]).

The image enhancement based methods rely on the resolution recovery using emission data and/or anatomical information. One such method that performs image enhancement during the image reconstruction using higher resolution MRI data has been developed by [44]. This algorithm promotes smoothing among nearby voxels that have similar MR image intensity. This method has recently been used in cardiac SPECT using a CT-based anatomical prior within the Green's one-step-late algorithm

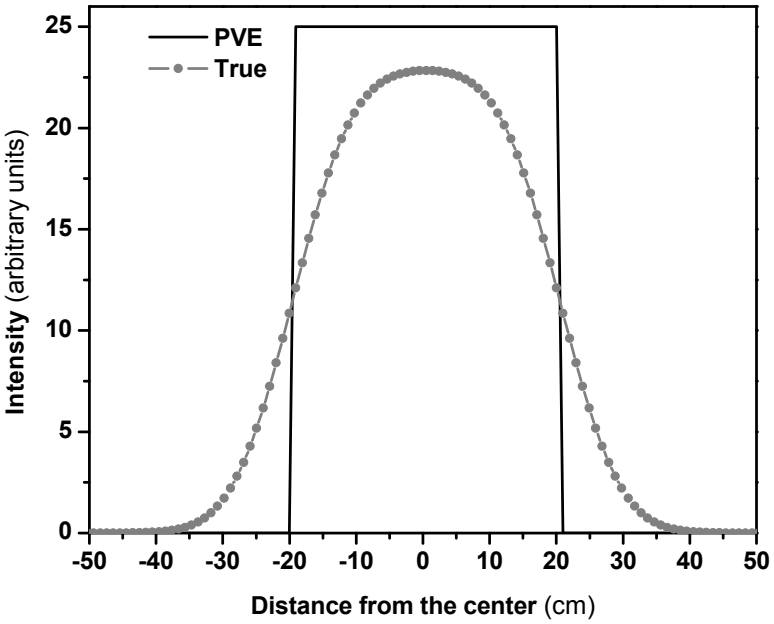

Figure 5.1: A depiction of geometric collimator response on a 40 cm wide rectangular activity profile (black) is shown in form of a curve (gray) caused mainly by spill-in and spill-out effect. Both the profiles have same area under the curve.

to suppress noise in the reconstructed image [45]. One major advantage of using this method is that it does not require segmentation of the anatomical image (i.e. CT or MRI). A more detailed description of these spatial resolution enhancement methods in emission tomography and related references can be found in [43].

The *maximum a-posteriori* (MAP) algorithm with a CT based anatomical prior, in one-step late framework, has previously been proposed to compensate for noise in cardiac SPECT [45]. This reconstruction algorithm with an analytical forward projector has been reported to produce visually striking results but, with limited quantitative accuracy. The current study focuses on the development of a quantitative MAP SPECT reconstruction algorithm that uses a CT based anatomical prior and CFD-SIMIND as a forward projector for image reconstruction. With the inclusion of CFD-SIMIND and the CT-based anatomical prior, this algorithm is expected to provide quantitatively accurate (due to CFD-SIMIND) SPECT images with an improved spatial resolution (because of CT-based anatomical prior).

5.1 Material and Methods

5.1.1 Reconstruction Algorithm

In this study, we propose to use an anatomical prior based *maximum a-posteriori* (AMAP) algorithm with accelerated convolution-based forced detection Monte Carlo as a forward projector (CFD-AMAP). This ordered subset expectation maximization (OSEM) algorithm uses the Green's one-step-late approach to find a new estimate f_j^{n+1} using the current estimate f_j^n of activity distribution in a voxel j using Equation 5.2.

$$f_j^{n+1} = \frac{f_j^n}{\sum_{a\epsilon s} H_a^T + \beta \frac{\partial}{\partial f_j^n} V(f_j^n)} \sum_{a\epsilon s} H_a^T \frac{\bar{p}_{ij}}{p_{ij}^{'} R^n t_{acq}} \tag{5.2}$$

where H_a^T is the analytical backprojector, $\bar{p}_{ij}$ and $p_{ij}^{'}$ are the measured and CFD Monte Carlo based projections of voxel j in ith bin respectively. R^n and t_{acq}, are the activity factor and acquisition time per projection respectively (required due to current implementation of MC based forward projector). $V(f_j^n)$, is the Gibbs energy function defined for a neighborhood size of N_j in Equation 5.3 [45].

$$V(f_j^n) = \sum_j \sum_{k\epsilon N_j} d_{jk} s_{jk} \left(f_j^n - f_k^n\right)^2 \tag{5.3}$$

here d_{jk} is the distance dependent weighting factor for neighboring voxels $k\epsilon N_j$ that is set equal to 1 for approximately spherical neighborhood of size 18 voxels. As depicted in Equation 5.2, the tuning of reconstruction algorithm is limited to varying weight of the prior β. In order to incorporate CT based anatomical information, a segmentation-free Bowsher's prior was used [44]. The essential parameters for Bowsher's prior include a) a definition of neighborhood (N_j), b) anatomical image based similarity metric, s_{jk} (either 0 or 1) and c) the number of neighbors, b, that must be selected for each voxel j. In this study, an approximately spherical neighborhood, consisted of $N_j = 18$ closest neighbors in a $3 \times 3 \times 3$ neighborhood, was used [45, 137]. The similarity metric, s_{jk} was based on the absolute intensity difference between the neighborhood voxels and a voxel j in the CT image. Based on the similarity metric either $b = 4$ or $b = 6$ was used respectively for the prior calculation. It is important to mention here that the choice of number of most similar neighbors, b, in the study is purely subjective and based on the studies reported previously (e.g [137]).

5.1.2 CFD-AMAP Feasibility

A simulation study using an analytic phantom with six spheres of different radii within a cylindrical background was performed to test the feasibility of CFD-AMAP. The radii and placement of spheres (diameters (ϕ) = 37 mm (S1), 28 mm (S2), 22 mm (S3), 17 mm (S4), 13 mm (S5) and 10 mm (S6)) were adapted from the NEMA IEC body phantom® (Data Spectrum Corporation) with external body replaced by a cylindrical background. An activity concentration of about 10:1 was achieved by simulating 227.7 kBq/cc and 22.8 kBq/cc of ^{99m}Tc (PEW width of 126−154 keV) in the spheres and the background respectively. A simulated SPECT acquisition, consisted of 120 projections (about 3.3×10^7 counts in total) with 128 × 128 matrix size (4.42 × 4.42 mm pixels), was performed using the GEANT-4 based MC code, GATE. A GE Infinia® SPECT/CT camera (General Electric, USA) with low-energy high resolution (LEHR) collimator was modeled for this study. The use of GATE for data acquisition is based on our previous study described earlier in beginning of this chapter [136]. Twenty noise realizations, with an acquisition time of 30 s per projection, were reconstructed using CFD-AMAP. The CFD-AMAP algorithm used a voxelized attenuation map (128 × 128 × 128, 4.42 mm isotropic) and CT image (512 × 512 × 512, 1.105 mm isotropic) for the reconstruction (Figure 5.2).

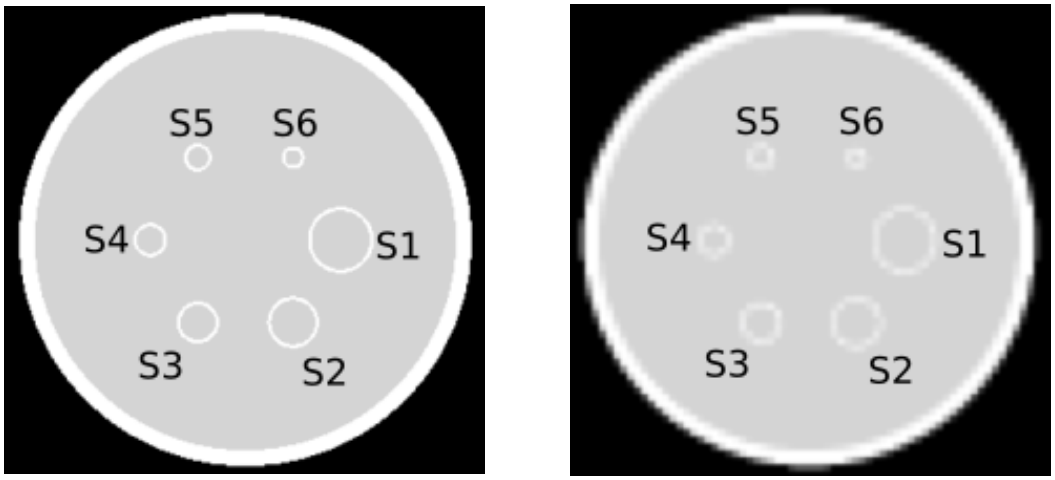

(a) Voxelized CT image (512 × 512 × 512, 1.105 mm isotropic)

(b) Voxelized attenuation map (128 × 128 × 128, 4.42 mm isotropic)

Figure 5.2: Simulation study: Voxelized (a) CT image and (b) attenuation map (obtained through linear interpolation of (a)) used respectively for prior determination and as the attenuation map in CFD-AMAP based reconstruction of simulation data.

Reconstruction of data with our proposed CFD-AMAP algorithm was performed using four prior weights, β = 0.0, $1{\times}10^{-6}$, $5{\times}10^{-6}$, $1{\times}10^{-5}$ respectively, and five iterations. The choice of the prior weight, β, was based on the non-negativity constraint in the image estimate. A value of $\beta = 0.0$ implies simple OSEM-based reconstruction with no prior included within the reconstruction algorithm. The algorithm used 30 subsets (i.e. 30 image updates per iteration) for the reconstruction.

5.1.3 CFD-AMAP Validation

After feasibility evaluation, we performed a SPECT/CT acquisition with NEMA IEC body phantom® on GE Infinia® SPECT/CT system with LEHR collimator to validate the CFD-AMAP. An activity concentration ratio of about 11.5:1 is obtained by depositing approximately 260 kBq/cc and 22.7 kBq/cc of ^{99m}Tc in the spheres and the background respectively. Twenty noise realizations, each with a set of 120 projections (acquisition time of 30 s/projection and about $2.3{\times}10^7$ counts in total) were acquired. An attenuation map (128 × 128 × 128, 4.42 mm isotropic) was calculated by the system using CT image (512 × 512 × 128, 1.105 mm × 1.105 mm × 4.42 mm) for the reconstruction. The same CT image was used for the anatomical prior calculations in CFD-AMAP. Four values of the prior weights, β =0.0, $1{\times}10^{-7}$, $5{\times}10^{-7}$, $1{\times}10^{-6}$ respectively, were used for the reconstruction. The reconstruction parameter values, except the prior weight, were similar to those used for simulated data reconstruction (described in Section 5.1.2). It is important to mention here that the CT image obtained from the system was aligned to the SPECT data manually using the system based attenuation map as a reference.

5.1.4 Data Analysis

In order to assess the bias and the effect of inclusion of Bowsher's prior on Monte Carlo based activity estimation, percent total activity ratio ($PTAR$) in the spherical ROI was determined using the true object ROI as follows [138]:

$$PTAR = 100 \times \left(\frac{\sum\limits_{j \epsilon Sphere} A_j^o}{\sum\limits_{j \epsilon Sphere} A_j^t \times w_j} \right) \tag{5.4}$$

here, A_j^o and A_j^t, denotes observed and true activity in jth voxel. Figure 5.3 shows the true spherical ROI's used in the experimental study. A weighting factor w_j (Equation 5.5) is used to account for the partially occupied voxels at the boundary or edges (i.e. tissue fraction) of the sphere for a given voxel size.

$$w_j = \frac{\text{True counts in voxel } j}{\text{True maximum counts in sphere}} \tag{5.5}$$

It should noted here that this partial counting of the edge voxels may lead to an underestimation as geometric response of the collimator is not included [139].

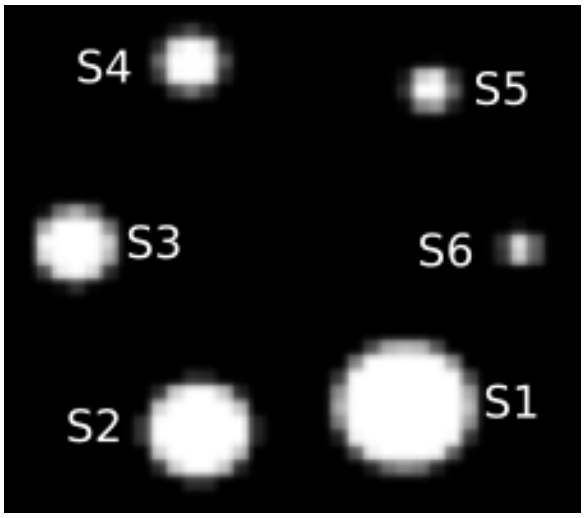

Figure 5.3: Experimental study: True object masks determined using Equations 5.4 and 5.5 for spherical ROI's in simulation study.

To assess the improvements in noise properties, effect on the Gibbs artifact and precision of the estimates, the coefficient of variation (CoV) was determined within each sphere using the above-mentioned mask.

This study also presents a comparison in terms of contrast (Equation 5.6) in order to evaluate the effect of inclusion of Bowsher's prior. For this purpose two spherical ROI's in the background were selected away from the central region with the hot spherical ROI's.

$$C = 100 \times \left(\frac{m_s/m_b - 1}{TR - 1} \right) \tag{5.6}$$

where m_s and m_b are the mean activity in the spherical and and background ROI's respectively. TR defines true activity ratio in the true object ROI's shown in Figure 5.3.

A visual comparison between center slice images for one of the noise realizations,

in the feasibility and validation studies, is also presented to see the effect of parameter β and the number of iterations on the reconstructed images.

A comparison of the inter-noise realizations variability or precision is presented in terms of an overall mean values of ensemble standard deviation images calculated using all the noise realizations in the study. This comparison is performed for all the simulation and experimental studies included in this work.

5.2 Results

5.2.1 Simulation Study

Figures 5.4(a) and 5.4(c) depict the plots of $PTAR$ as a function of number of iterations for the spheres S1 (ϕ = 37 mm), S3 (ϕ = 22 mm), S5 (ϕ = 13 mm) and S6 (ϕ = 10 mm) with the prior calculation using i) 4 and ii) 6 nearest neighbors out of 18 respectively. The figures show $PTAR$ values that are within $\pm$5%, for each spherical ROI in the plots, for all the prior weights after a given number of iterations. This number (i.e. $\pm$5%) holds for all the spherical ROI's including spheres S2 (ϕ = 28 mm) and S3 (ϕ = 22 mm) that show relatively larger reduction of $PTAR$ with increase in β.

A significant reduction of CoV over each spherical ROI in the plots with increase in prior weight, β, for a given number of iterations is evident from the Figures 5.4(b) and 5.4(d) representing i) and ii) respectively. Figures 5.4(b) and 5.4(d) show a more or less uniform CoV after the first iteration for each non-zero value of β. A simple OSEM based reconstruction (i.e. $\beta = 0.0$) is the only exception that shows an increase in CoV with number of iterations for all the ROI's (except sphere S1) in both the cases. Table 5.1 depicts a comparison between CoV values obtained after 2 and 5 iterations for all the prior weights for i). A trend similar to Figure 5.4(b) is evident from the Table 5.1.

A more uniform activity distribution over the spherical ROI's (i.e. better noise regularization) and a better depiction of the boundaries with increase in the value of β is evident from the Figures 5.5 and 5.6. Figures 5.5 and 5.6 show a noticeable change in contrast with increase in the prior weight for a given number of iterations. This reduction is also depicted in the Figure 5.7 for i) and ii) respectively.

Figure 5.7 shows a loss of contrast with increase in β that is less than 5% for larger

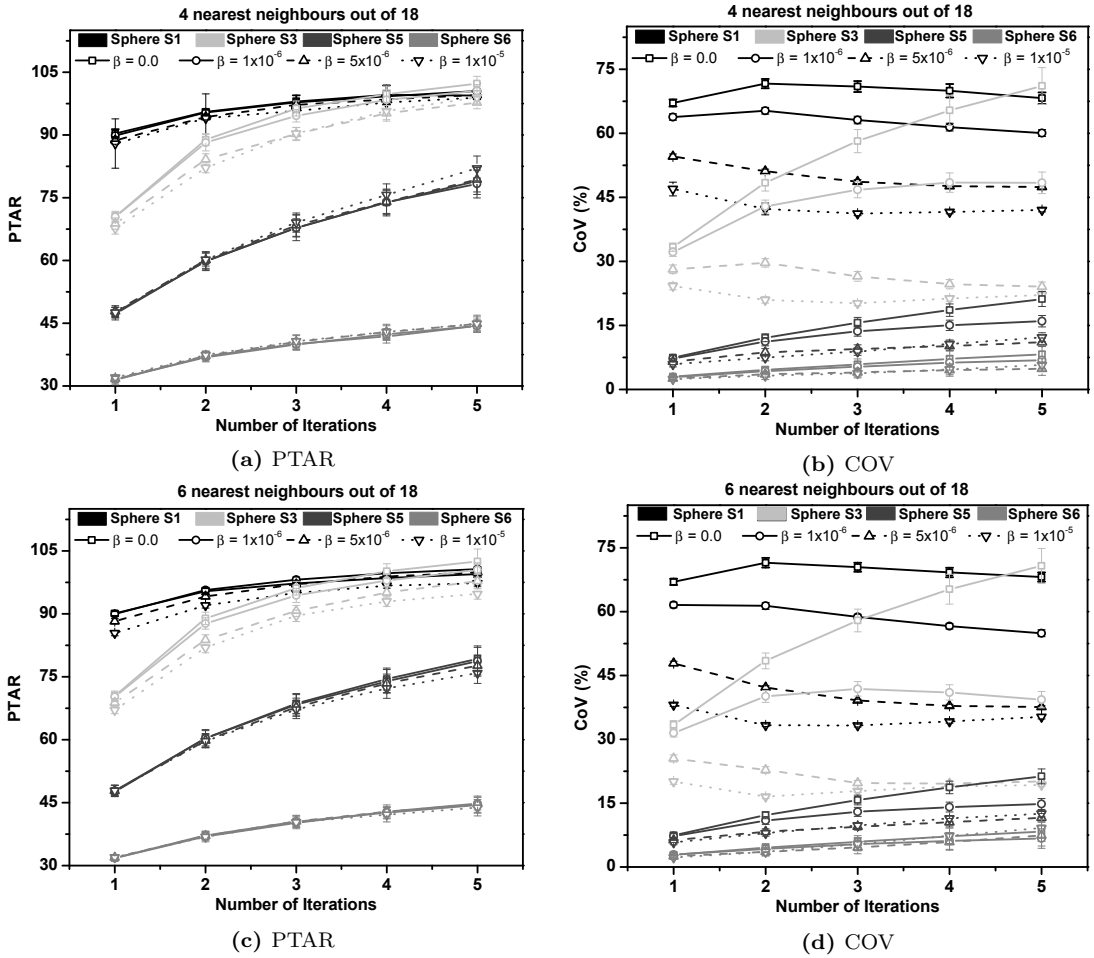

(a) PTAR **(b)** COV

(c) PTAR **(d)** COV

Figure 5.4: Simulation Study: A comparison of CFD-AMAP with different prior weights in terms of (a), (c) percent total activity ratio ($PTAR$) and (b), (d) coefficient of variation (CoV) for spheres S1 ($\phi = 37$ mm), S3 ($\phi = 22$ mm), S5 ($\phi = 13$ mm) and S6 ($\phi = 10$ mm) as a function of number of iterations for prior determination with 4 and, 6 nearest neighbors out of 18 respectively.

spheres (i.e. S1 ($\phi = 37$ mm) and S3 ($\phi = 22$ mm)) accompanied by corresponding gain in contrast for the smaller spheres (i.e. S5 ($\phi = 13$ mm) and S6 ($\phi = 10$ mm)). This implies that the CFD-AMAP provides percentage contrast within $\pm$ 5% for each sphere for all the prior weights after a given number of iterations. This is also evident from Table 5.2 for the case i). Table 5.2 shows a comparison of contrast for all the spherical ROI's after two and five iterations. Both Figure 5.7 and Table 5.2 show a significant gain in contrast, especially for spherical regions other than S1 ($\phi = 37$ mm) and S2 ($\phi = 28$ mm) after five iterations compared to two for a given value of β.

As an example, circular profiles obtained after five iterations for one of the noise realizations are depicted in Figure 5.8. Figure 5.8 indicates a more uniform activity

Table 5.1: Simulation: *CoV* for all the spheres and background with prior weight β for 2 and 5[a] iterations of CFD-AMAP (4 out of 18 neighbors).

	CoV			
Region\β-value	**0.0**[b]	$\mathbf{1 \times 10^{-6}}$	$\mathbf{5 \times 10^{-6}}$	$\mathbf{1 \times 10^{-5}}$
S1	71.6 ± 1.1	65.3 ± 0.8	51.1 ± 0.6	42.3 ± 1.4
	(68.2 ± 1.4)	(60.0 ± 0.8)	(47.4 ± 0.5)	(42.0 ± 0.4)
S2	69.8 ± 1.4	59.8 ± 1.0	39.8 ± 0.5	27.8 ± 0.5
	(84.3 ± 2.6)	(58.6 ± 1.4)	(31.7 ± 0.6)	(30.4 ± 0.6)
S3	48.4 ± 1.9	42.9 ± 1.5	29.7 ± 1.0	21.0 ± 0.7
	(71.1 ± 4.3)	(48.4 ± 2.5)	(24.1 ± 1.1)	(22.1 ± 0.6)
S4	25.5 ± 1.0	22.7 ± 0.9	16.4 ± 0.5	13.8 ± 0.6
	(42.8 ± 2.1)	(28.9 ± 1.0)	(19.8 ± 1.1)	(21.3 ± 0.9)
S5	12.1 ± 0. 9	11.2 ± 1.0	8.7 ± 0.9	7.5 ± 0.8
	(21.2 ± 1.8)	(16.0 ± 1.3)	(11.1 ± 1.0)	(12.2 ± 1.1)
S6	4.6 ± 0. 9	4.3 ± 0.8	3.6 ± 0.7	3.2 ± 0.9
	(8.2 ± 2.2)	(6.8 ± 2.0)	(4.9 ± 1.5)	(5.7 ± 1.5)
Background	5.4 ± 0.9	5.2 ± 0.7	5.0 ± 0.7	4.9 ± 0.6
	(10.6 ± 1.4)	(10.1 ± 1.2)	(8.7 ± 1.1)	(7.5 ± 0.9)

[a] *CoV* values for 5^{th} iteration are within parenthesis. [b] A prior weight, $\beta = 0.0$, indicates simple OSEM based reconstruction.

and hence better boundary delineation with increase in the prior weight, β. A more gradual decrease in activity away from the center of ROI in case of simple OSEM based reconstruction is again evident in the Figure 5.8. Figure 5.8 shows a slightly better spatial resolution enhancement in the case of ii) compared to i) for a given value of the prior weight and the number of iterations. This is also evident from Figure 5.9 that shows a comparison between i) and ii) for $\beta = 1 \times 10^{-5}$ as magnified images. A slightly better boundary definition in corresponding images, when the 6 most similar neighbors are selected, indicates relatively more speedy enhancement in spatial resolution in this case.

A comparison of inter-noise realizations dispersion is presented in Figure 5.10. The figure shows mean of ensemble standard deviation images in simulation study for i) and ii). A relatively higher precision with increase in the prior weight for i) and ii) for a given number of iterations is evident from the figure. Correspondingly, lower values of mean standard deviation in the case of ii) compared to i) are also visible in 5.10(a) and 5.10(b) respectively.

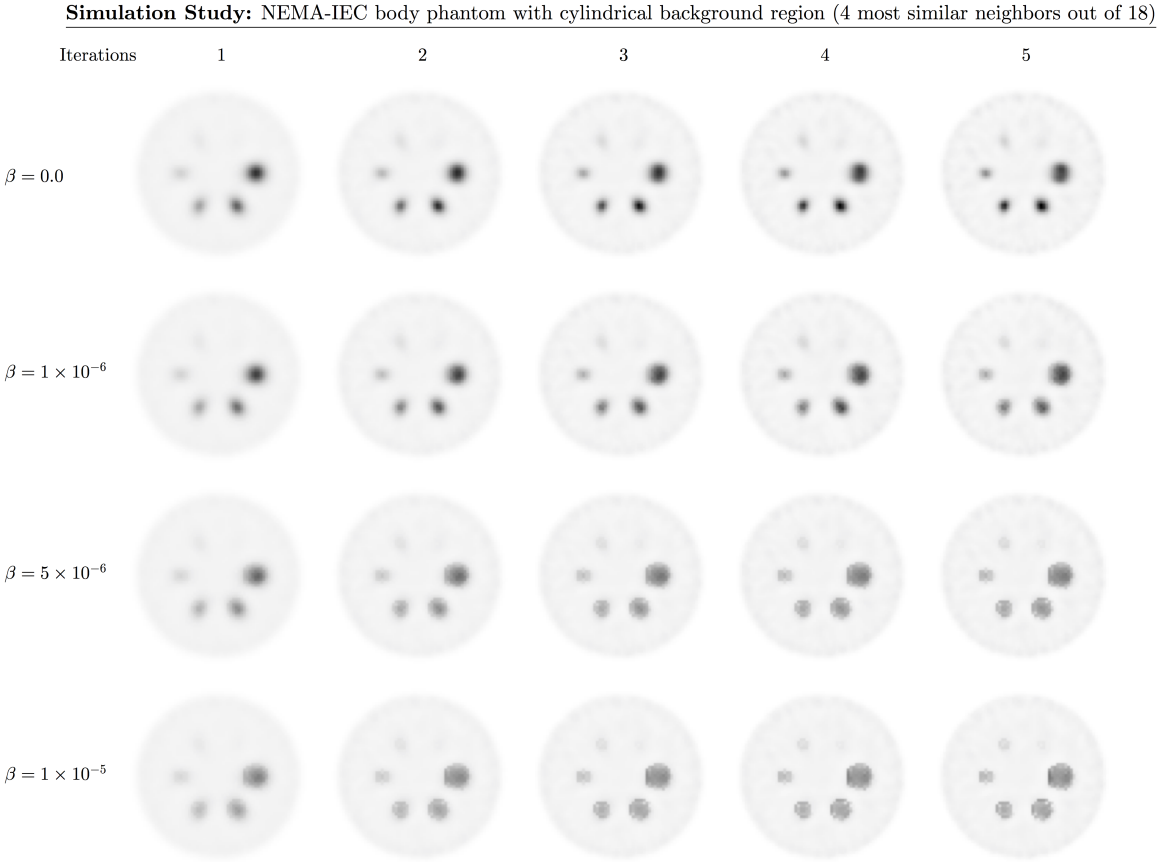

Figure 5.5: Simulation Study (4 out of 18 Neighbors): Depiction of images for one of the noise realizations an an example. The figure show the variation in visual perception of images with number of iterations (horizontal) and the prior weight, β (vertical).

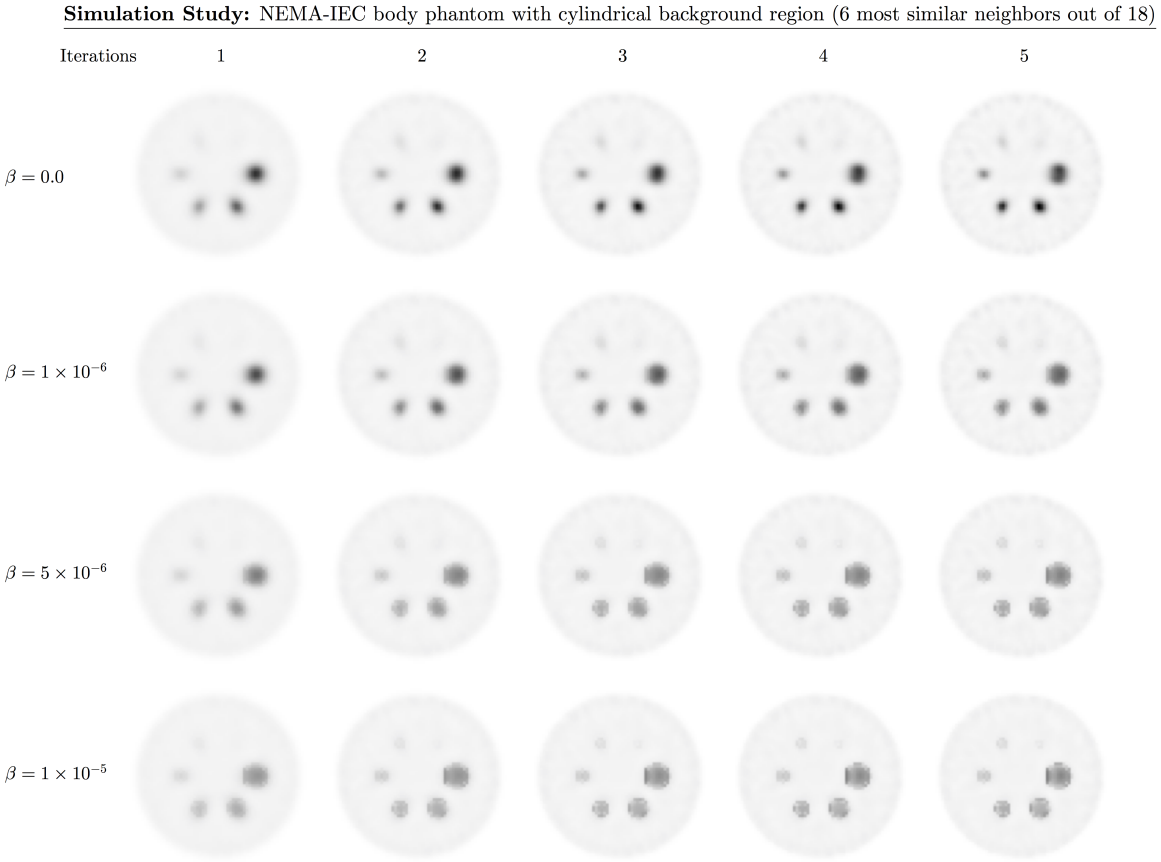

Figure 5.6: Simulation Study (6 out of 18 Neighbors): Depiction of images for one of the noise realizations an an example. The figure show the variation in visual perception of images with number of iterations (horizontal) and the prior weight, β (vertical).

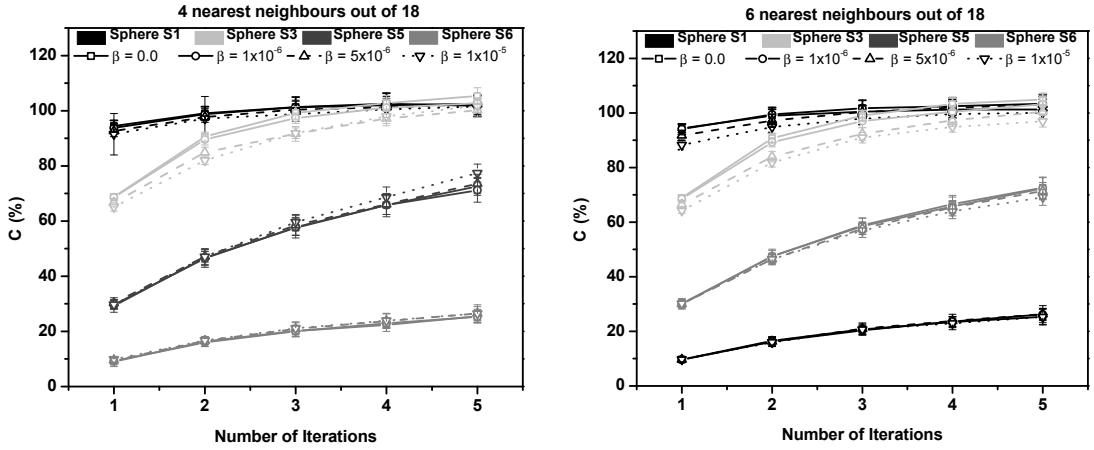

(a) 4 nearest neighbors out of neighborhood **(b)** 6 nearest neighbors out of neighborhood

Figure 5.7: Simulation Study: A comparison of CFD-AMAP with different prior weights in terms of contrast as a function of number of iterations for spherical ROI's, S1 ($\phi = 37$ mm), S3 ($\phi = 22$ mm), S5 ($\phi = 13$ mm) and S6 ($\phi = 10$ mm) in the case of (a) 4 and (b) 6 nearest neighbors out of 18 respectively.

Table 5.2: Simulation: Contrast, C (%) for all the spheres and background with prior weight β for 2 and 5* iterations of CFD-AMAP (4 out of 18 neighbors).

	C (%)			
Region\β-value	**0.0†**	**1×10^{-6}**	**5×10^{-6}**	**1×10^{-5}**
S1	99.1 ± 2.1	98.8 ± 2.1	97.7 ± 1.9	97.2 ± 8.0
	(101.8 ± 3.8)	(102.6 ± 3.3)	(102.4 ± 2.8)	(101.6 ± 2.8)
S2	98.4 ± 2.1	97.0 ± 2.1	91.5 ± 1.7	87.1 ± 1.9
	(103.9 ± 3.4)	(103.1 ± 2.6)	(100.1 ± 2.4)	(96.7 ± 2.4)
S3	90.6 ± 1.7	89.6 ± 2.0	84.9 ± 1.9	82.0 ± 1.5
	(105.3 ± 3.1)	(102.7 ± 2.1)	(100.2 ± 2.4)	(101.7 ± 2.2)
S4	71.2 ± 3.7	69.7 ± 4.7	69.8 ± 3.2	69.1 ± 4.4
	(98.3 ± 5.7)	(95.6 ± 5.3)	(95.9 ± 4.8)	(98.3 ± 4.9)
S5	46.7 ± 2.8	46.5 ± 3.3	47.1 ± 2.9	47.1 ± 1.9
	(72.6 ± 3.3)	(71.2 ± 4.3)	(73.5 ± 3.5)	(77.4 ± 3.3)
S6	16.4 ± 1.7	16.0 ± 1.5	16.6 ± 1.3	16.8 ± 1.4
	(25.5 ± 2.5)	(25.3 ± 2.0)	(26.4 ± 2.5)	(26.5 ± 3.1)

* Values of contrast for 5^{th} iteration are within parenthesis. † A prior weight, $\beta = 0.0$, indicates simple OSEM based reconstruction.

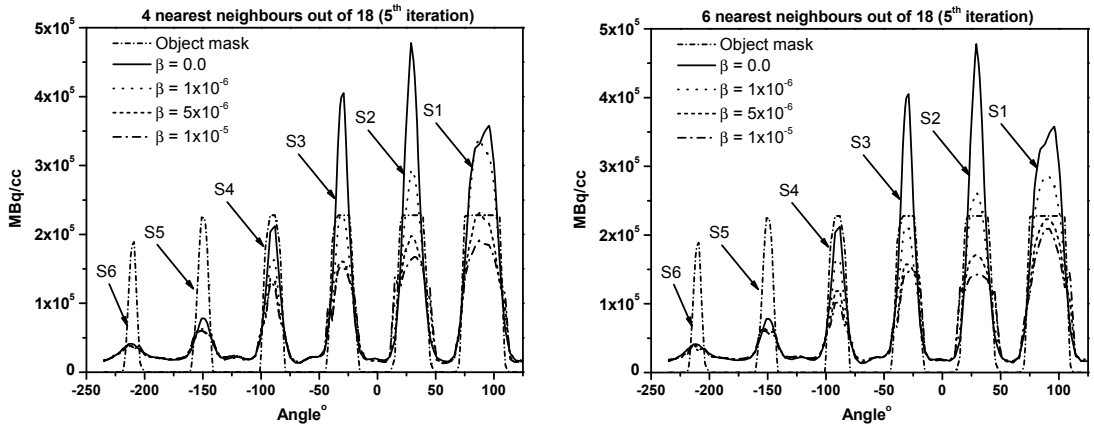

Figure 5.8: Simulation Study: A comparison of circular profiles, at 5^{th} iteration, through the spherical ROI's for the images reconstructed with selection of (a) 4 and (b) 6 nearest neighbors in CFD-AMAP.

Simulation Study: Comparison between 4 and 6 out of 18 neigbors ($\beta = 1 \times 10^{-5}$)

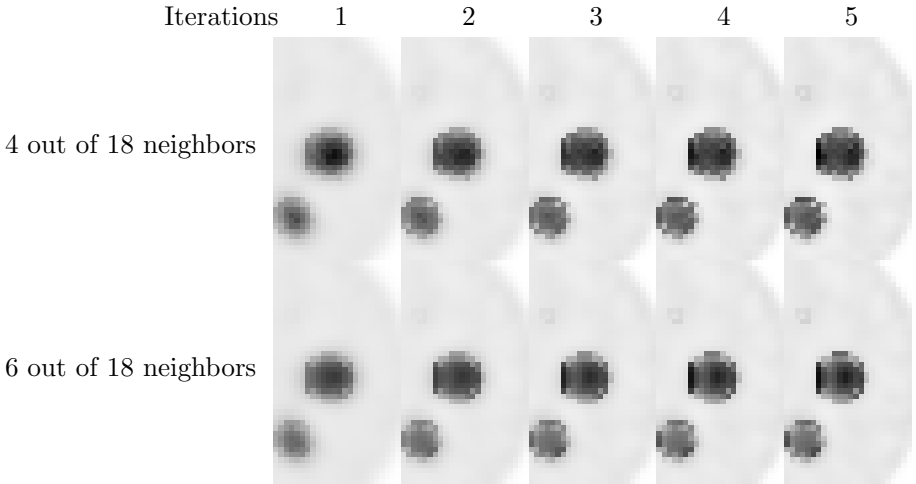

Figure 5.9: Simulation Study: Difference in image perception due to choice of either 4 or 6 out 18 most similar neighbors, for spheres S1 ($\phi = 37$ mm) and S2 ($\phi = 28$ mm), shown through the magnification of images.

5.2.2 Experimental Evaluation

An analysis similar to simulation study described in Section 5.2.1 was also performed for experimental data. Figures 5.11(a) and 5.11(c) depict plots of $PTAR$ as a function

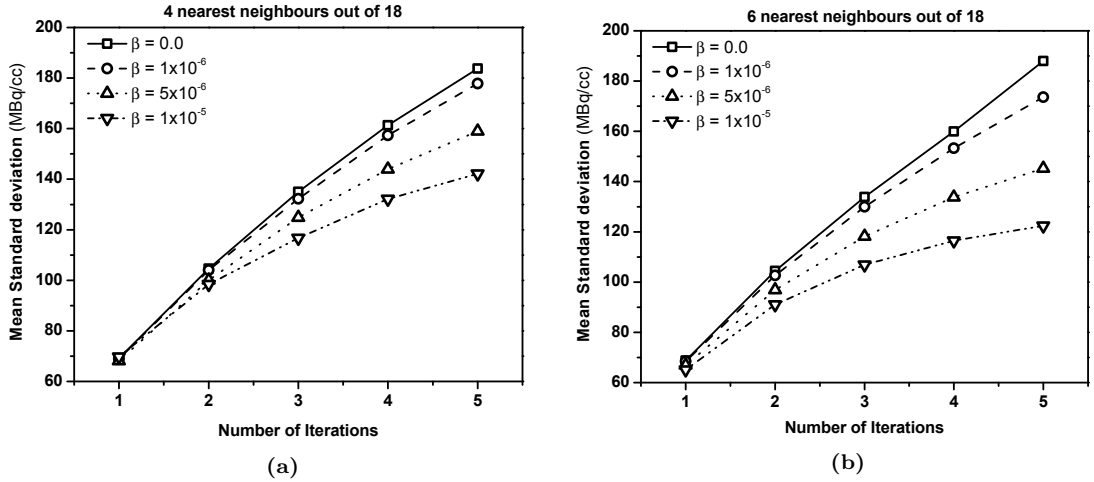

Figure 5.10: Simulation Study: A comparison of mean of the ensemble standard deviation images of 20 noise realizations for (a) 4 and (b) 6 nearest neighbors in CFD-AMAP.

of number of iterations for the spheres S1 ($\phi = 37$ mm), S3 ($\phi = 22$ mm), S5 ($\phi = 13$ mm) and S6 ($\phi = 10$ mm) respectively with prior calculation using i) 4 and ii) 6 nearest neighbors. After a given number of iterations, the figures show $PTAR$ values for all the prior weights that are within ±8%. Based on the error bars, a $PTAR$ of within ±8% applicable to all the spherical ROI's including spheres S2 ($\phi = 28$ mm) and S3 ($\phi = 22$ mm) as these ROI's show relatively larger reduction of $PTAR$ with an increase in the value of β for a given number of iterations.

A significant reduction of CoV with increase in the prior weight, β, for a given number of iterations is evident from the Figures 5.11(b) and 5.11(d) representing i) and ii) respectively. An overall rising trend in CoV with number of iterations is visible in the Figures 5.11(b) and 5.11(d). However, Figures 5.11(b) and 5.11(d) depict a reduction is steepness of the CoV curves with increase in importance of the prior, β, in CFD-AMAP. Table 5.3 depicts a comparison in terms of CoV for different regions including the background ROI as a function of prior weight, β obtained after 2 and 5 iterations for ii). A trend similar to Figure 5.11(d) is evident from the Table 5.3.

Figures 5.12 and 5.13 depict a slightly more uniform activity distribution over spherical ROI's and better boundary delineation with increase in the value of β. A slight

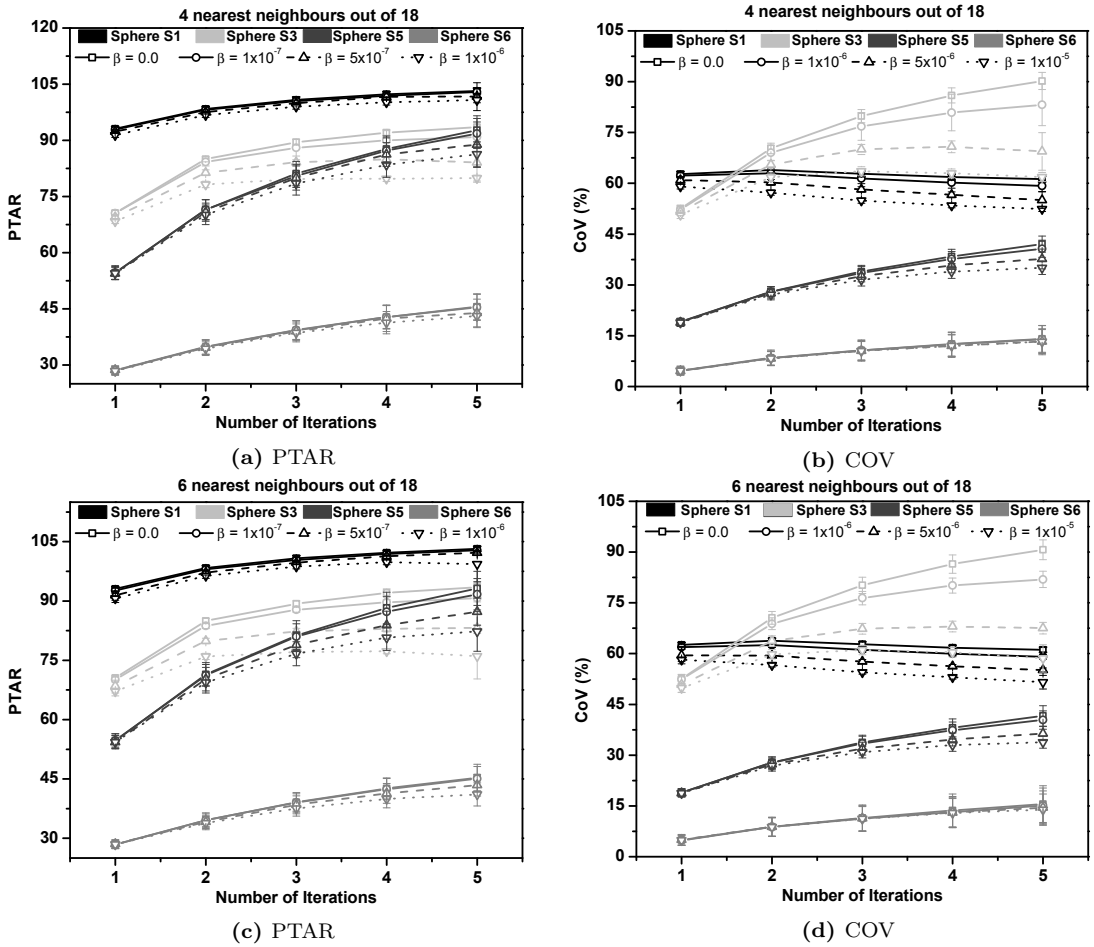

(a) PTAR **(b)** COV

(c) PTAR **(d)** COV

Figure 5.11: Experimental Study: A comparison of CFD-AMAP with different prior weights in terms of (a), (c) percent total activity ratio ($PTAR$) and (b), (d) coefficient of variation (CoV) for spheres S1 ($\phi = 37$ mm), S3 ($\phi = 22$ mm), S5 ($\phi = 13$ mm) and S6 ($\phi = 10$ mm) as a function of number of iterations for prior determination with 4 and, 6 nearest neighbors out of 18 respectively.

loss of contrast with increase in the prior weight for a given number of iterations is also evident from the Figures 5.12 and 5.13 representing i) and ii) respectively. Figure 5.14 also depicts this reduction in contrast for i) and ii) respectively. Figure 5.14 shows a loss of contrast with increase in β-value with largest reduction of about 8% for the spheres S1 ($\phi = 37$ mm), S3 ($\phi = 22$ mm), S5 ($\phi = 13$ mm) and S6 ($\phi = 10$ mm) respectively after a give number of iterations. In short, CFD-AMAP provides percentage contrast within $\pm$ 8% for all the prior weights for a given number of iterations. Table 5.4 shows a comparison of contrast for all the ROI's after two and five iterations for ii). Both Figure 5.14 and Table 5.4 indicates a significant gain in contrast after five iterations for a given value of β compared to two.

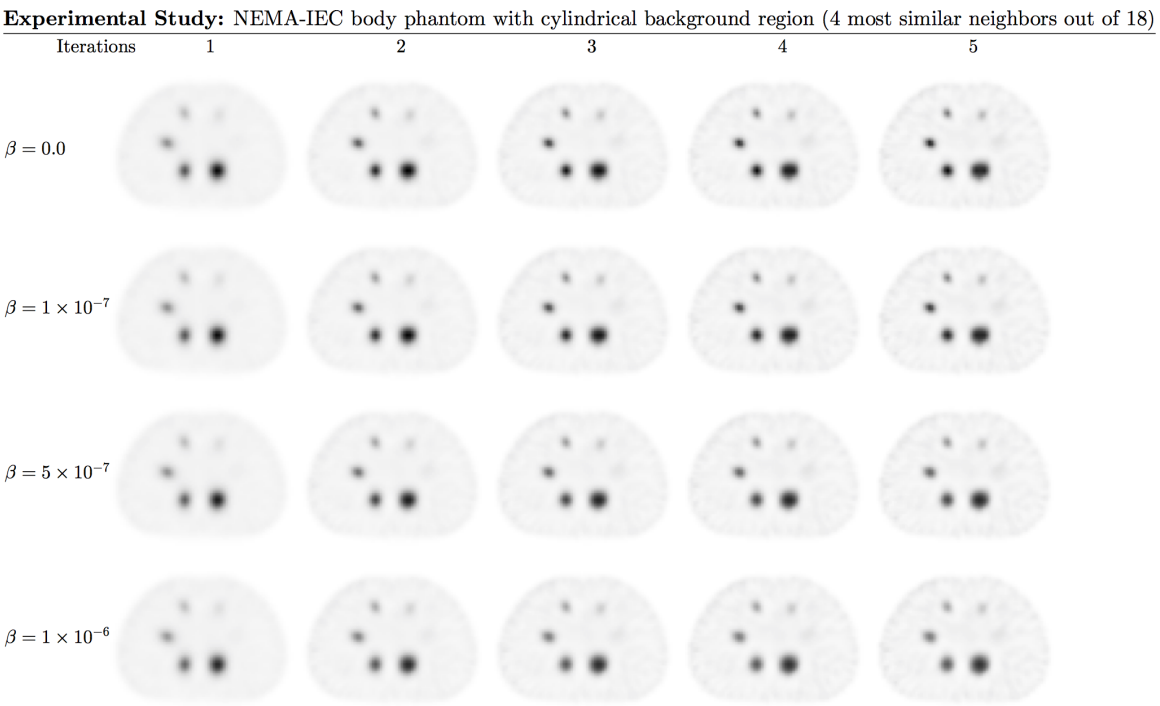

Figure 5.12: Experimental Study (4 out of 18 Neighbors): Depiction of images for one of the noise realizations an an example. The figure show the variation in visual perception of images with number of iterations (horizontal) and the prior weight, β (vertical).

Circular profiles obtained after five iterations for one of the noise realizations are depicted in Figure 5.15. Figure 5.15 indicates a more uniform activity and better boundary depiction with increase in value of β. Figure 5.15 also shows a slightly better enhancement of spatial resolution in the case of six most similar neighbors for corresponding prior weights compared to four most similar neighbors.

A comparison of inter-noise realizations dispersion is presented in Figure 5.16. The figure shows mean of ensemble standard deviation images in simulation study for i) and ii). A noticeable increase in the precision with increase in the prior weight in only evident for i) with $\beta = 1.0 \times 10^{-6}$ and ii) for a given number of iterations. Correspondingly, lower values of mean standard deviation in the case of ii) compared to i) are also visible in 5.16(a) and 5.16(b) respectively.

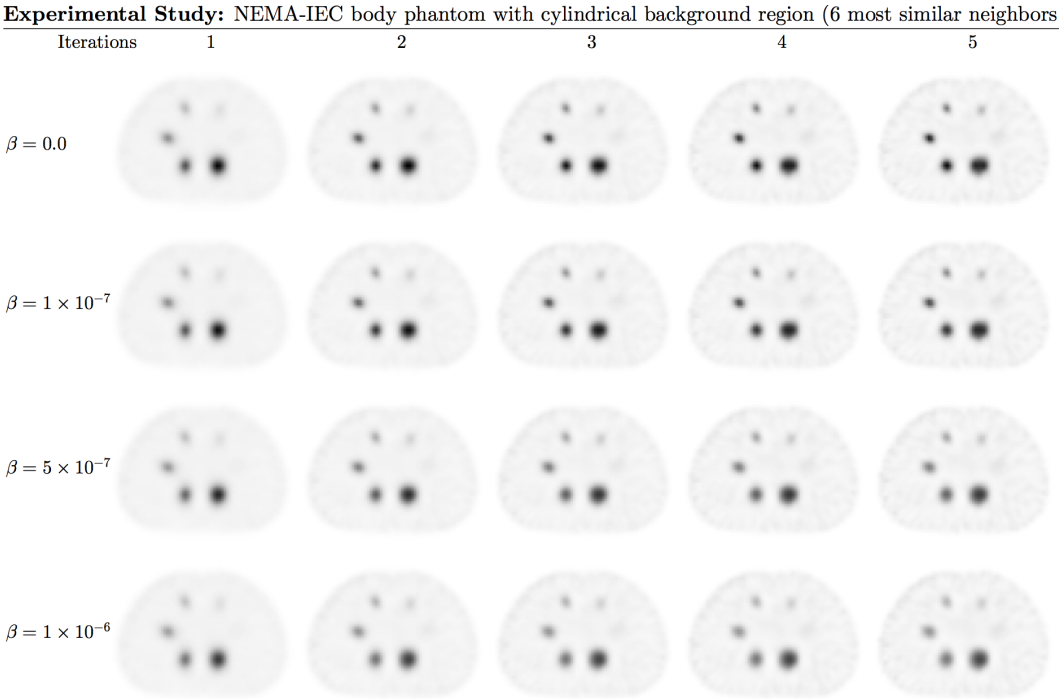

Figure 5.13: Experimental Study (6 out of 18 Neighbors): Depiction of images for one of the noise realizations an an example. The figure show the variation in visual perception of images with number of iterations (horizontal) and the prior weight, β (vertical).

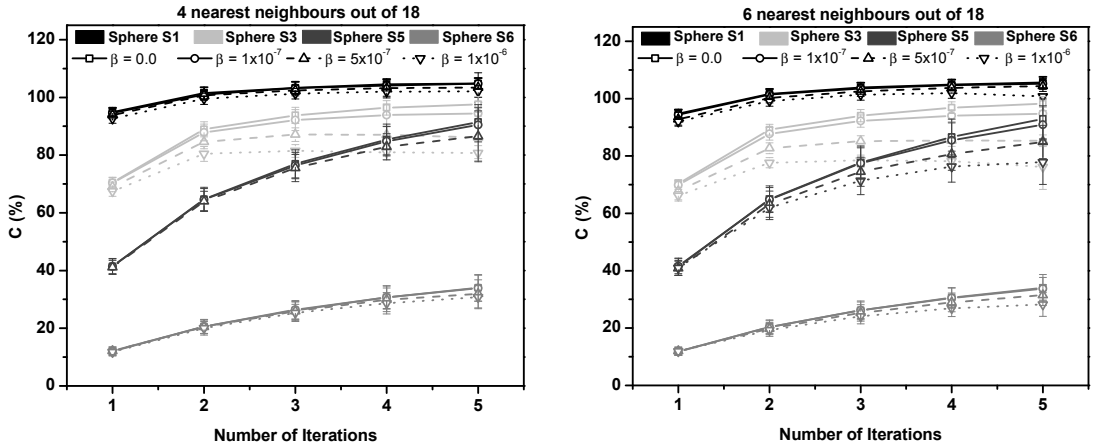

(a) 4 nearest neighbors out of neighborhood **(b)** 6 nearest neighbors out of neighborhood

Figure 5.14: Experimental Study: A comparison of CFD-AMAP with different prior weights in terms of contrast as a function of number of iterations for spherical ROI's, S1 ($\phi = 37$ mm), S3 ($\phi = 22$ mm), S5 ($\phi = 13$ mm) and S6 ($\phi = 10$ mm) in the case of (a) 4 and (b) 6 nearest neighbors out of 18 respectively.

Table 5.3: Experimental: *CoV* for all the spheres and background with prior weight β for 2 and 5[a] iterations of CFD-AMAP (6 out of 18 neighbors).

	CoV			
Region\β-value	**0.0**[b]	$\mathbf{1 \times 10^{-6}}$	$\mathbf{5 \times 10^{-6}}$	$\mathbf{1 \times 10^{-5}}$
S1	63.8 ± 0.8	62.5 ± 0.7	59.4 ± 0.6	56.6 ± 0.5
	(61.1 ± 0.7)	(59.0 ± 0.7)	(55.2 ± 0.6)	(51.5 ± 2.0)
S2	82.9 ± 1.3	81.2 ± 1.2	76.1 ± 1.2	71.7 ± 1.2
	(90.1 ± 2.0)	(85.5 ± 2.0)	(75.5 ± 1.7)	(67.2 ± 4.5)
S3	70.6 ± 1.9	68.8 ± 1.7	63.7 ± 1.5	59.8 ± 1.4
	(90.7 ± 2.9)	(81.9 ± 2.4)	(67.5 ± 1.7)	(58.6 ± 4.0)
S4	59.9 ± 1.9	59.2 ± 1.8	56.7 ± 1.9	54.1 ± 1.8
	(81.82 ± 2.4)	(76.8 ± 2.3)	(65.5 ± 2.3)	(58.0 ± 3.4)
S5	27.9 ± 1.6	27.8 ± 1.7	27.3 ± 1.6	26.1 ± 1.9
	(41.6 ± 3.0)	(40.4 ± 2.7)	(36.4 ± 2.1)	(33.8 ± 1.8)
S6	8.9 ± 2.8	8.8 ± 2.7	8.8 ± 2.9	8.8 ± 2.7
	(15.5 ± 5.4)	(15.1 ± 5.2)	(14.5 ± 4.9)	(13.9 ± 4.6)
Background	9.6 ± 1.0	9.5 ± 1.0	9.4 ± 1.1	9.3 ± 1.2
	(17.5 ± 1.2)	(17.2 ± 1.1)	(16.5 ± 1.1)	(15.8 ± 1.3)

[a] *CoV* values for 5^{th} iteration are within parenthesis. [b] A prior weight, $\beta = 0.0$, indicates simple OSEM based reconstruction.

Table 5.4: Experimental: Contrast, C (%) for all the spheres and background with prior weight β for 2 and 5[*] iterations of CFD-AMAP (6 out of 18 neighbors).

	C (%)			
Region\β-value	**0.0**[†]	$\mathbf{1 \times 10^{-6}}$	$\mathbf{5 \times 10^{-6}}$	$\mathbf{1 \times 10^{-5}}$
S1	101.7 ± 1.7	101.4 ± 1.8	100.3 ± 1.7	99.1 ± 1.8
	(105.6 ± 2.0)	(105.2 ± 2.0)	(104.4 ± 1.9)	(100 ± 6.2)
S2	86.9 ± 2.0	86.0 ± 1.8	83.1 ± 1.8	80.0 ± 1.9
	(91.2 ± 2.5)	(89.7 ± 2.7)	(85.6 ± 2.1)	(80.5 ± 6.3)
S3	89.2 ± 1.9	87.7 ± 2.2	82.7 ± 1.9	77.7 ± 1.8
	(98.2 ± 2.4)	(94.8 ± 2.2)	(85.3 ± 2.0)	(76.2 ± 7.8)
S4	80.8 ± 1.9	79.7 ± 1.6	76.5 ± 1.8	72.7 ± 1.6
	(96.3 ± 2.3)	(93.3 ± 2.3)	(84.6 ± 1.9)	(75.7 ± 8.2)
S5	64.9 ± 4.6	64.8 ± 4.3	63.2 ± 4.6	61.8 ± 4.1
	(92.9 ± 6.9)	(90.9 ± 6.6)	(84.9 ± 5.8)	(77.8 ± 5.4)
S6	20.4 ± 2.4	20.4 ± 2.2	19.8 ± 2.1	19.3 ± 2.2
	(34.0 ± 4.6)	(33.7 ± 3.9)	(31.5 ± 3.6)	(28.2 ± 4.1)

[*] Values of contrast for 5^{th} iteration are within parenthesis. [†] A prior weight, $\beta = 0.0$, indicates simple OSEM based reconstruction.

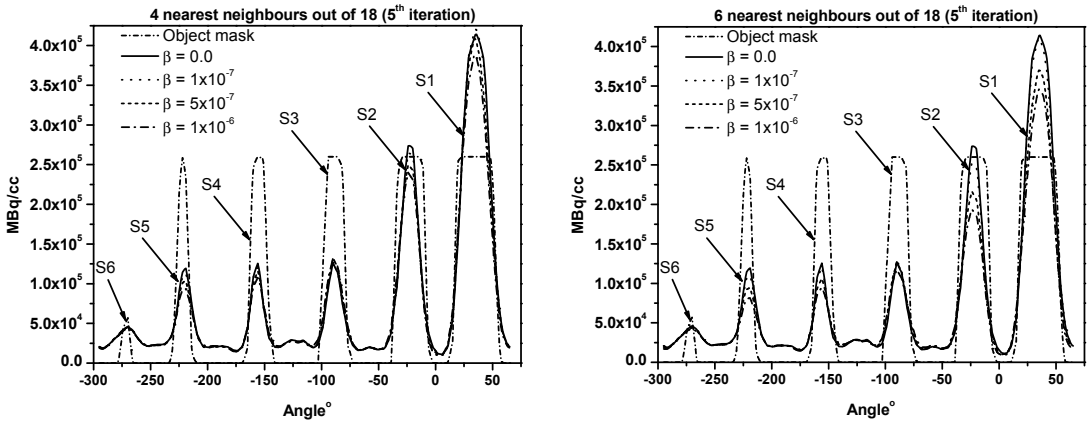

(a) (b)

Figure 5.15: Experimental Study: A comparison of circular profiles, at 5^{th} iteration, through the spherical ROI's for the images reconstructed with selection of (a) 4 and (b) 6 nearest neighbors in CFD-AMAP.

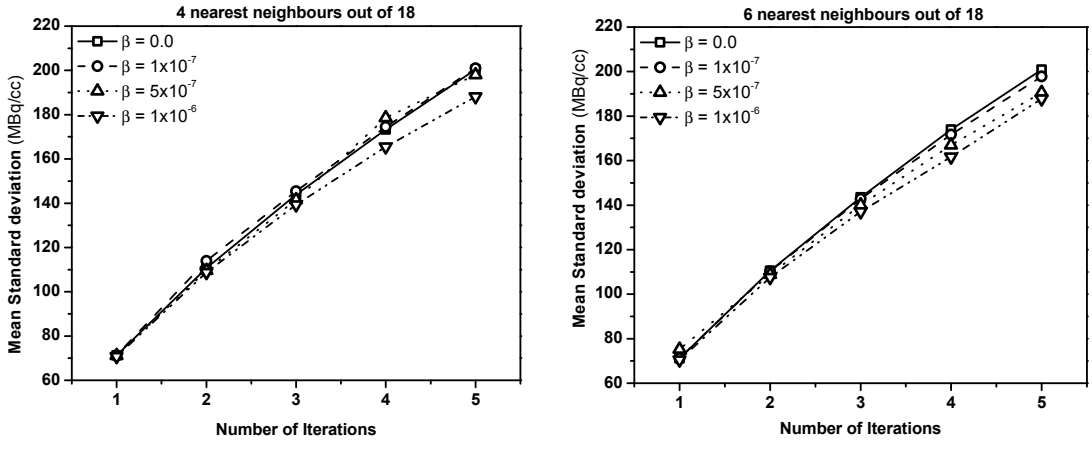

(a) (b)

Figure 5.16: Experimental Study: A comparison of mean of the ensemble standard deviation images of 20 noise realizations for (a) 4 and (b) 6 nearest neighbors in CFD-AMAP.

5.3 Discussion

Experimental study uses relatively smaller values of prior weight, β, compared to simulations (given in Sections 5.2.1 and 5.2.2) based on the non-negativity constraint. The choice of β limits the enhancement of the spatial resolution and noise regularization that can be achieved in both the cases. Even though this *adhoc* determination of β-value is a well-known issue with Green's OSL algorithm [140], the study uses this algorithm due to ease of implementation and to evaluate the interplay between mismatched forward/backprojector pair (i.e. CFD-SIMIND based forward projector and analytical backprojector with attenuation and the geometric collimator response modeling) and, quantification capabilities of CFD-SIMIND and the CT based anatomical prior. For the reason described latter, relatively low-noise projection data (about 3.3×10^7 and 2.3×10^7 total counts in simulation and experimental study respectively) were acquired in both the studies.

A slight reduction of $PTAR$, depicted in Figures 5.4 and 5.11 with increase in the prior weight (especially, for spherical ROI's S2, S3 and S4) may indicate the limitation of proposed true object mask as mentioned in Section 5.1.4. Despite of a sincere efforts to include partially occupied boundary pixels into the object mask, the blurring caused by geometric response of the collimator was not included in the mask. This under-estimation of volume of ROI's by the mask (depicted in circular profiles shown in Figures 5.8 and 5.15) and more uniform activity distribution over the blurred ROI's with increase in β may be the main causes of this reduction of $PTAR$.

The main reasons for increase in CoV as depicted in Figures 5.4 and 5.11 for simulation and experimental studies respectively, in particular for OSEM (i.e. $\beta = 0.0$) based reconstruction, with number of iterations may include, a) a typical noise amplification with increase in number of iterations, associated with maximum likelihood expectation maximization based algorithms [19] and b) Gibbs artifact (loss of apparent activity in the central region of the spheres) indicated in Figure 5.17 for a simulation study. A slightly reduction (i.e. a more or less uniform trend) in CoV depicted in Figures 5.4(b) and 5.4(d) in simulation and reduction in steepness of the curve with increase in value of β for experimental study (Figures 5.11(b) and 5.11(d)) depicts improved noise regularization and compensation of the Gibbs artifact.

This trend for OSEM based reconstruction is also evident from the Tables 5.1 and 5.3. Both the tables indicate that the inclusion of the anatomical prior in the CFD-AMAP

Simulation Study: Magnified image of sphere S1 (ϕ=37mm) with no prior

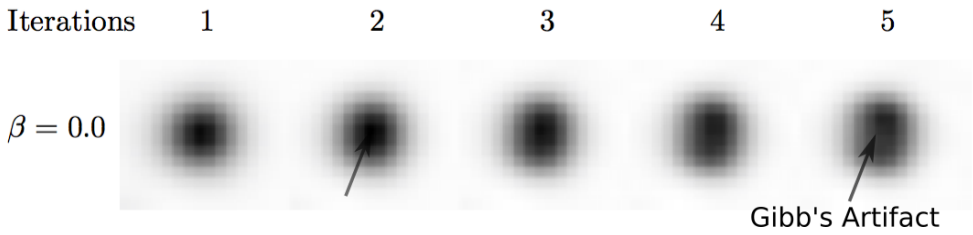

Figure 5.17: Simulation Study: Magnified image of sphere S1 ($\phi = 37mm$) showing Gibbs artifact.

not only provides a mean for noise regularization but, also performs compensation of Gibbs artifact. A reduction in CoV with increase in β, as previously shown in Figures 5.4 and 5.11, with relatively uniform background is also depicted in Tables 5.1 and 5.3 respectively. This reduction of CoV and relatively negligible impact ($\pm$5% and $\pm$8% for each spherical ROI in simulation and experimental studies respectively) on quantification capabilities of CFD MC indicate a better noise regularization, an improved boundary delineation and a relatively good activity quantification with CFD-AMAP based reconstruction.

Comparatively higher CoV and lower $PTAR$ in experimental study may be caused by the much lower number of counts (about 10 million less counts) in this case.

In simulation study, the enhancement of spatial resolution (as indicated by reduction of CoV) with CFD-AMAP is evident from the Figures 5.5 and 5.6 for i) and ii) respectively. This improvement in boundary delineation is also evident from the circular profiles shown in Figure 5.8. Figure 5.8 depicts a better uniformity within the spherical ROI's and a more rapid fall of the activity at the edges with increase in β. This indicates a better spatial resolution with increase in β. Corresponding Figures 5.12, 5.13 and 5.15 for experimental study show results that are very similar to simulation study except, the extent of noise regularization and enhancement of spatial resolution is slightly less due to reasons described at the beginning of this section. A comparatively better boundary depiction for ii) compared to i), for a give value of β and number of iterations, is also depicted in Figures 5.8 and 5.15.

It is important to note here that in simulation study the sphere S1 (ϕ=37mm) shows a relatively flat inner (left) edge. The reason for this flatness is the boundary wall definition (2.210 mm thick) in the presumed noise-free CT image (Figure 5.2(a)). The same side also appears slightly flat in Figure 5.2(a). This problem could easily be tackled by using the real CT image of a non-voxelized phantom rather than writing

a MATLAB code to create a barely 2-pixels thick spherical boundary wall. This also implies that the attainable spatial resolution in the reconstructed image for CFD-AMAP is defined by the spatial resolution of the anatomical prior.

In simulation study, a small gain in uniformity with CFD-AMAP (i.e. reduction of CoV) for the bigger spheres, S1, S2 and S3 is accompanied by corresponding loss in the smaller spheres, S4, S5 and S6 in case of five compared to two iterations as depicted in Table 5.1. Correspondingly, Table 5.3 shows a slight loss of CoV for five iterations of CFD-AMAP compared to two in experimental study. Therefore, based on the data presented in these tables, it may be concluded that there is no significant difference between the images reconstructed using two or five iterations in terms of CoV. In other words two iterations of CFD-AMAP may be suffice to provide an acceptable image in terms of uniformity. Each iteration usually takes 2-4 hours on a dual core CPU (2.66 GHz Intel Core i5 processor), thus implying significant reduction in reconstruction time with two iterations. However, this reduction in the number of iterations (i.e. two compared to five) and hence a gain in terms of time comes at the cost of loss of contrast as depicted in Tables 5.2 and 5.4 for the simulation and experimental study respectively.

Figures 5.10 and 5.16 depict plots of mean of the ensemble standard deviation images as a function of number of iteration for simulation and experimental studies respectively. Based on the data presented in these figures two important observations can be made a) a much less improvement in the inter-noise realizations variability or precision for experimental data compared to the simulation study and b) both the studies show a slightly more precision for ii) compared to i) for a given value of the prior weight and the number of iterations. The use of relatively lower prior weight in the experimental study may be the reason behind observation a).

5.4 Conclusion

In this work, we proposed a MAP reconstruction algorithm that uses CFD Monte Carlo as a forward projector and a CT-based anatomical prior for accurate quantification and, noise regularization respectively. Even though *adhoc* determination of the prior weight to avoid negative voxel values in the reconstructed image and possible divergence are the major limitations of this algorithm, this work uses the algorithm due to ease of implementation and to study the interplay between quantification capabilities of

CFD-SIMIND based forward projector and the anatomical prior. The proposed CFD-AMAP algorithm generates images that are spatially better resolved with comparable quantitative accuracy (within ±5% and ±8% for simulation and experimental studies respectively) to simple OSEM based reconstruction (i.e. $\beta = 0.0$). The use of six compared to four most similar neighbors in the neighborhood for the prior calculation has resulted in a better boundary depiction. The choice of number of iterations in CFD-AMAP is based on the trade-off between the time taken for image reconstruction and an acceptable contrast in the image. A study with CFD MC incorporated into a better Bayesian reconstruction algorithm (e.g. [140]) to overcome major limitations of CFD-AMAP is planned in the near future.

Chapter 6

Conclusion and Future Work

IN this work, we performed a detailed comparison between previously reported CFD implementation into SIMIND Monte Carlo program (i.e. CFD-SIMIND) and GEANT-4 based MC code GATE. The study was intended to perform an exhaustive comparison between CFD-SIMIND and a well-known standard MC code like GATE as i) such study has not been reported earlier and ii) in order to see whether the CFD-SIMND can be replaced or used in conjunction with GATE in the studies where collimator interactions are not important (e.g. for isotopes with low and medium energy gamma emissions like ^{99m}Tc and ^{111}In). It is evident from the point source simulation results presented in Chapter 2 of this work that CFD-SIMIND agrees well with GATE with detection sensitivity difference ranging from 3−5%, spatial resolution within 0.2 mm and overall image quality similarly, Q_{UI} value, of 0.994 ± 0.009. More complex simulations using the XCAT phantom also showed similar results. A reduction by a factor of 5−6 orders of magnitude in time can be achieved with CFD-SIMIND compared to GATE while maintaining very similar photon transport accuracy.

In Chapters 3 and 4 of this work, we have introduced a Monte Carlo-based reconstruction method, Sim-OSEM that has shown some promising results in separating the corresponding isotope images in simultaneously acquired ^{99m}Tc/^{111}In and ^{99m}Tc/^{123}I projection data. This is achieved through crosstalk compensation by incorporating accelerated CFD-SIMIND MC as a forward projector into iterative reconstruction algorithm. It is evident from the results shown in Chapter 3 that while both triple energy window (TEW) and Sim-OSEM provide higher contrast and reduction of crosstalk

artifacts compared to no scatter compensation, the proposed Sim-OSEM technique yields slightly better crosstalk correction compared to the TEW method. The study shows that Sim-OSEM performs reasonably accurate activity estimation, although a rigorous analysis of quantitation with multiple noise realizations was not performed. In Chapter 4, we have presented our perceived application of simultaneous ^{99m}Tc/^{123}I SPECT in breast imaging that has not yet been reported in patients. We believe that this kind of dual-isotope SPECT imaging can help in distinguishing between benign, malignant and potentially malignant lesions in breast. The simulation studies presented in Chapter 4 yielded promising results in terms of accurate quantitation for simultaneous ^{99m}Tc/^{123}I SPECT.

Simulation and experimental studies in order to quantify possible improvement in SNR and spatial resolution are presented in Chapter 5. The study shows that the inclusion of CT-based anatomical prior (i.e. Bowsher's prior) in Sim-OSEM [44] using one-step-late approach, improve boundary delineation without interfering too much with quantification ability of CFD-SIMIND based forward projector. It is important to mention here that the prior weight, β limits amount of spatial resolution enhancement achieved through this algorithm. This limit on the maximum possible value of β in the algorithm is due to the non-negativity constraint on a voxel content in the image and to avoid divergence.

6.1 Future Work

The recommendations for future work can be based on the existing shortcomings of the studies presented in this work and the ideas to remedy them. These may include i) more studies to further evaluate the current work ii) receiver operating characteristics (ROC) analysis, iii) further acceleration of CFD-SIMIND and iv) use of better image reconstruction algorithms.

6.1.1 Studies to Evaluate the Current Work

So far, simulation and experimental evaluations have been performed using a uniform attenuation map in form of a point source and NEMA IEC body phantom set for ^{99m}Tc/^{111}In simultaneous SPECT. In the future, some additional experiments using more complex phantoms with non-uniform attenuation may be performed to further

elaborate on the strength and effectiveness of Sim-OSEM.

In the study involving simultaneous ^{123}I/^{99m}Tc, experimental validation of Sim-OSEM has yet to be performed. The reason for the absence of experimental results in the study was unavailability of the breast phantom at our department. We initially planned to design and print these phantoms for all the breast sizes using a 3-D printer for experimental validation. However, due to diversion to another isotope duo that is ^{99m}Tc/^{111}In, this plan could not be followed.

It should be noted that simulations described in both of above-mentioned studies were done using a non-uniform attenuation map in the form of the XCAT phantom. The strength of the simulation studies can be further improved by performing acquisition on an independent MC code like GATE because in these simulation studies the same forward projector (i.e. CFD-SIMIND) was used for acquisition and subsequent Sim-OSEM based reconstruction.

Similar studies may also be performed for other candidates of simultaneous multi-isotope SPECT imaging. One of the prime example of such isotope duos is ^{201}Tl/^{99m}Tc which, is used in cardiac imaging (e.g. [83, 121]). It has been reported earlier in Chapters 3 and 4 that Sim-OSEM based reconstruction provides quantitatively accurate images with possible improvements in SNR and resolution. This implies simultaneous ^{201}Tl/^{99m}Tc cardiac SPECT reconstruction using Sim-OSEM promises not only to improve ^{201}Tl based quantitation, but may also be able to generate better resolved ^{99m}Tc images.

One of the main goals of this work was to use and separate images from simultaneously acquired dual-isotope data using NaI(Tl)-PMT based gamma cameras. Currently, Cadmium Zinc Telluride (CZT) based dedicated cardiac and scintimammography scanners are becoming popular. The costly CZT scanners (e.g. D-SPECT®) provide list-mode data that can be corrected for scatter and crosstalk [141] and believed to provide simultaneous dual-radionuclide images comparable to those obtained from reconstruction of separately acquired data as described by Haim et.al. [142] in cardiac SPECT. In future, a study can be performed to compare the quality of images obtained using CZT scanners to the NaI(Tl) based images reconstructed using Sim-OSEM. Such studies would provide an objective tool to see if standard gamma cameras (with no access to list-mode data) in combination with Sim-OSEM can provide simultaneously acquired multi-isotope SPECT images comparable to dedicated and expensive CZT-based systems.

In order to improve the accuracy and performance of the proposed algorithms (i.e. Sim-OSEM), experiments to optimize acquisition parameters for different simultaneous dual-isotope SPECT candidates as, described by Wang et.al. [143] and Du et.al. [144], may also be performed.

One of the ultimate goals and tests of strength of any reconstruction algorithm would be the real patient data. Real patient studies may be possible in the future after a rigorous task-based ROC analysis of Sim-OSEM, described briefly in Section 6.1.2.

6.1.2 Receiver operating characteristics (ROC) Analysis

The assessment of image quality is an important tool in medical imaging research. This tool can be used to compare two competing systems or image processing algorithms. The most useful, meaningful and reproducible way to evaluate image quality either on a detection or detection plus localization task performed by a human observer is **receiver operating characteristic** (ROC) or **localization based receiver operating characteristic** (LROC) analysis respectively. In ROC analysis a plot between true positive (i.e. sensitivity) as a function of false positive (i.e. 1-specificity) is used to compare different systems, protocols or image processing algorithms. ROC analysis of task based image quality assessment for Sim-OSEM based reconstruction compared to other dual isotope reconstruction algorithms may also be performed in future.

Rather than using human observer, a mathematical observer, implemented in the form of a computer algorithm, can also be used to perform the image quality assessment task. After establishing the accuracy and applicability of the proposed reconstruction method, mathematical observer studies may also be performed as done by Song et.al. [145]. In this work by Song et.al., mathematical observer studies were performed for evaluation of their model-based crosstalk compensation method in simultaneous ^{99m}Tc/^{201}Tl myocardial perfusion SPECT. The image quality assessment tasks should be performed for all the different isotope combinations, which are either being used or are potential candidates for multi-isotope SPECT in future.

The work presented in Chapter 5 depicts an improvement in spatial resolution that may not be helpful in the imaging tasks related to lesion detection as this compensation may result in an overall reduction in contrast due to noise regularization. However, enhancement in the spatial resolution plays an important role in the studies that require accurate boundary delineation and quantitation. Quantitative simultaneous ^{99m}Tc/^{201}Tl myocardial perfusion SPECT [120, 145] and the recent studies involving

targeted radionuclide therapy with ^{177}Lu-DOTATATE (for neuroendocrine tumors) [146, 147] and ^{177}Lu-PSMA (for prostate cancer) are the examples of such studies [148]. In these studies target delineation and accurate quantitation (e.g. accurate depiction and amount of perfusion in myocardium in simultaneous ^{99m}Tc/^{201}Tl cardiac SPECT imaging or accurate quantification and boundary depiction of the target in ^{177}Lu therapy) are of prime importance. Therefore, a task-based LROC analysis of CFD-AMAP based image reconstruction may prove helpful in these applications.

6.1.3 Further Acceleration of CFD-SIMIND

Sim-OSEM based dual-isotope reconstruction takes 3-5 hrs for 2 iterations and 30 subsets. Therefore, there is clearly a room for improvement in terms of speed. Kinsman and Nicolici [149] have able to double the speed of SPECT simulations using a modestly sized FPGA compared with a 2 GHz Intel Core 2 Duo Processor. This implies that CFD-SIMIND could be accelerated further by implementation on a newer and better version of FPGA and that a collaboration with Dr. Nicolici's group in future could be a great help in this regard.

6.1.4 Better Image Reconstruction Algorithms

The study presented in Chapter 5 of this work, simply incorporates anatomical information into OSEM algorithm in one-step-late (OSL) framework. One major limitation as described in Section 1.3.2.3, is the conservative choice of prior weight to avoid possible negative value in the denominator or even divergence [140]. Alternatively, in order to handle this OSL-trick better, a gradient ascent algorithm with block or patchwork structure can be used [150]. Vunckx et.al. [140] have recently proposed a novel, simple and flexible approach to handle prior weight called balanced update steps MAP (BUS-MAP) reconstruction. In this algorithm the new estimate f_j^{new} can be found using the separate current estimate for data, $f_j^{old,DATA}$ and the prior, $f_j^{old,PRIOR}$ as:

$$f_j^{new} = f_j^{old} + (1-\alpha) \triangle f_j^{old,DATA} + \alpha \triangle f_j^{old,PRIOR} \tag{6.1}$$

with quadratic energy function used in the study (Chapter 5), $0 \leq \alpha \leq 1$ and

$$\triangle f_j^{old,DATA} = \frac{f^{old}}{\sum_i H_{ij}^T} \sum_i H_{ij}^T \left(\frac{p_i}{\sum_j H_{ij} f^{old}} - 1 \right) \tag{6.2}$$

also

$$\triangle f_j^{old,PRIOR} = \frac{f_j^{old} + \sum_k f_k^{old}}{K+1} - f_j^{old} \tag{6.3}$$

here K is the number of similar neighbors compared with voxel j. It is important to mention here that even though the algorithm promises more flexibility on choice of prior term weight, α in this case, but tuning of this parameter still has to be performed by the user.

6.2 Summary and Outlook

In summary, we were able to perform a comprehensive comparison between CFD-SIMIND and GATE for low and medium energy isotopes. This study could be used as an objective tool to choose either between or both the codes depending on the nature of the study. We were also able to successfully incorporate CFD-SIMIND into OSEM based iterative reconstruction algorithms to correct for crosstalk between simultaneously acquired ^{111}In/^{99m}Tc and ^{123}I/^{99m}Tc SPECT data respectively. The proposed reconstruction algorithm performs a reasonably accurate activity quantification. A study presented in this work uses a CT-based anatomical prior for noise regularization and compensation of PVE incorporated into a *maximum a-posteriori* (MAP) algorithm that uses CFD-SIMIND (for quantification) as the forward projector. The proposed algorithm generates quantitatively accurate images that has been compensated for PVE. It is important to describe here that the choice of prior weight, β, based on the non-negativity constraint on the voxel content, limits the PVC attainable through this algorithm.

Further studies with more complex phantoms and real patient data, task-based ROC studies, improvement in CFD-SIMIND in terms of speed and use of better Bayesian image reconstruction algorithms are needed to elaborate on the strengths and weaknesses of this proposed MC based forward projector and to pave the way for

CFD-SIMIND based image reconstruction algorithms from research to clinic.

Bibliography

[1] A. B. Brill and R. N. Beck. "Evolution of Clinical Emission Tomography". In: *Emission Tomography: The Fundamentals of PET and SPECT*. Ed. by M. N. Wernick and J. N. Aarsvold. First. Nashville, Tennesee: Elsevier Academic Press, 2004, pp. 25–52 (cit. on pp. 1–3).

[2] S. Vallabhajosula. "Molecular Imaging: Radiopharmaceuticals for PET and SPECT". In: Berlin Heidelberg: Springer-Verlag, 2009. Chap. Radiopharmaceuticals, pp. 133–150 (cit. on pp. 2, 3).

[3] S. R. Cherry, J. A. Sorenson, and M. E. Phelps. "Physics in Nuclear Medicine". In: Fourth. Elsevier Science (USA), 2012. Chap. Radionuclide and Radiopharmaceutical Production, pp. 43–61 (cit. on pp. 2, 3, 5–9).

[4] A. Rahmim and H. Zaidi. "PET versus SPECT: strengths, limitations and challenges". In: *Nucl. Med. Comm.* 29.3 (2008), pp. 193–207 (cit. on pp. 5, 6).

[5] D. L. Gunter. "Collimator Design for Nuclear Medicine". In: *Emission Tomography: The Fundamentals of PET and SPECT*. Ed. by M. N. Wernick and J. N. Aarsvold. First. Nashville, Tennesee: Elsevier Academic Press, 2004, pp. 153–168 (cit. on pp. 6, 7).

[6] G. L. Zeng, J .R. Galt, M. N. Wernick, R. A. Mintzer, and J. N. Aarsvold. "Single Photon Emission Computed Tomography". In: *Emission Tomography: The Fundamentals of PET and SPECT*. Ed. by M. N. Wernick and J. N. Aarsvold. First. Nashville, Tennesee: Elsevier Academic Press, 2004, pp. 127–152 (cit. on p. 6).

[7] T. E. Peterson and L. R. Furenlid. "SPECT detectors: the Anger Camera and beyond". In: *Phys. Med. Biol.* 56 (2011), R145–R182 (cit. on pp. 7, 9).

[8] Glenn F. Knoll. "Radiation Detection and Measurement". In: 4th. John Wiley & Sons, 2010. Chap. Photomultiplier Tubes and Photodiodes, pp. 275–320 (cit. on pp. 7, 9).

[9] D. M. Khan and T. H. Farncombe. "Multiplexing Silicon Photomultiplier (SiPM) arrays for SPECT". In: *Proc. 2014 IEEE Medical Imaging Conf* (2014) (cit. on p. 9).

[10] P. Busca, M. Occhipinti, P. Trigilio, G. Cozzi, C. Fiorini, C. Piemonte, A. Ferri, A. Gola, K. Nagy, T. Bukki, and J. Rieger. "Experimental Evaluation of a SiPM-Based Scintillation Detector for MR-Compatible SPECT Systems". In: *Proc. 2015 IEEE Medical Imaging Conf* 62.5 (2015), pp. 2122–2128 (cit. on p. 9).

[11] D. J. Wagenaar. "CdTe and CdZnTe Semiconductor Detectors for Nuclear Medicine Imaging". In: *Emission Tomography: The Fundamentals of PET and SPECT*. Ed. by M. N. Wernick and J. N. Aarsvold. First. Nashville, Tennesee: Elsevier Academic Press, 2004, pp. 269–291 (cit. on pp. 9, 10).

[12] E. G. DePuey. "Advances in SPECT camera software and hardware: Currently available and new on the horizon". In: *J Nucl Card* Published online (2012), pp. 1071–3581 (cit. on p. 10).

[13] S. Surti. "Radionuclide Methods and Instrumentation for Breast Cancer Detection and Diagnosis". In: *Semin Nucl Med* 43 (2013), pp. 271–280 (cit. on p. 10).

[14] G. K. von Schulthess. "Positron emission tomography versus positron emission tomography/computed tomography: From "unclear" to "new-clear" medicine". In: *Mol Imaging Biol* 6.4 (2004), pp. 183–187 (cit. on p. 11).

[15] C. N. Patel, F. U. Chowdhury, and A. F. Scarsbrook. "Hybrid SPECT/CT: The end of "unclear" medicine". In: *Postgrad Med J.* 85.1009 (2009), pp. 606–613 (cit. on p. 11).

[16] S. R. Cherry, J. A. Sorenson, and M. E. Phelps. "Physics in Nuclear Medicine". In: Fourth. Elsevier Science (USA), 2012. Chap. Hybrid Imaging: SPECT/CT and PET/CT, pp. 345–360 (cit. on p. 11).

[17] G. Wells. "CT-SPECT/CT-PET". In: *Medical Imaging: Technology AND Applications*. Ed. by T. H. Farncombe and K. Iniewski. Devices, Circuits, and Systems. CRC Press: Taylor & Francis Group, Florida, USA, 2014, pp. 335–358 (cit. on p. 11).

[18] T. H. Farncombe. "Multimodality Imaging with MR/PET and MR/SPECT". In: *Medical Imaging: Technology AND Applications*. Ed. by T. H. Farncombe and K. Iniewski. Devices, Circuits, and Systems. CRC Press: Taylor & Francis Group, Florida, USA, 2014, pp. 359–402 (cit. on p. 11).

[19] Gengsheng L. Zeng. *Medical Image Reconstruction: A Conceptual Tutorial*. Third. Berlin, Heidelberg: Springer-Verlag, 2003 (cit. on pp. 13, 14, 111).

[20] P. E. Kinahan, M.Defrise, and R. Cackdoyle. "Analytical Image Reconstruction Methods". In: *Emission Tomography: The Fundamentals of PET and SPECT*. Ed. by M. N. Wernick and J. N. Aarsvold. First. Nashville, Tennesee: Elsevier Academic Press, 2004, pp. 421–442 (cit. on p. 14).

[21] L A Shepp and Y Vardi. "Maximum likelihood estimation for emission tomography". In: *IEEE Trans. Med. Imaging* 1 (1982), pp. 113–121 (cit. on p. 15).

[22] K Lange and R. Carson. "EM reconstruction for emission and transmission tomography". In: *IEEE Trans. Med. Imaging* 8 (1984), pp. 306–316 (cit. on p. 15).

[23] H M Hudson and R S Larkin. "Accelerated image reconstruction using ordered subsets of projection data". In: *IEEE Trans. Med. Imaging* 13 (1994), pp. 601–609 (cit. on p. 16).

[24] D S Lalush and B M W Tsui. "Performance of ordered-subset reconstruction algorithm under attenuation and truncation in myocardial SPECT". In: *J. Nucl. Med.* 41 (2000), pp. 737–744 (cit. on p. 16).

[25] W. E. Bolch. "The Monte Carlo Method in Nuclear Medicine: Current Uses and Future Potential". In: *J Nucl Med* 51.3 (2010-02), pp. 337–339. ISSN: 0161-5505. DOI: 10.2967/jnumed.109.067835 (cit. on pp. 18, 21, 33).

[26] E. R. Stan Ulam and J. V. Neumann. "and the Monte Carlo Method". In: *Los Almos Sci* 15 (1987), pp. 131–136 (cit. on p. 18).

[27] M. Ljungberg. "Simulation Techniques and Phantoms". In: *Emission Tomography: The Fundamentals of PET and SPECT*. Ed. by M. N. Wernick and J. N. Aarsvold. First. Nashville, Tennesee: Elsevier Academic Press, 2004, pp. 551–563 (cit. on pp. 18, 19, 30, 77, 91).

[28] M. Ljungberg, S. Strand, and M. A. King. *Monte Carlo Calculations in Nuclear Medicine: Applications in Diagnostic Imaging*. 2nd. Series in Medical Physics and Biomedical Engineering. CRC Press: Taylor & Francis Group, Florida, USA, 2012 (cit. on pp. 18, 33).

[29] S. Liu, M. A. King, A. B. Brill, M. G. Stabin, and T. H. Farncombe. "Accelerated SPECT Monte Carlo simulation using multiple projection sampling and convolution based force detection". In: *IEEE Trans in Nucl Sci* 55.1 (2008), pp. 560–567 (cit. on pp. 19, 21, 30, 34, 35, 50, 55, 58, 63, 72, 77, 78, 92).

[30] H. Zaidi. "Monte Carlo Modeling in Nuclear Medicine Imaging". In: *Quantitative Analysis in Nuclear Medicine Imaging*. Ed. by H. Zaidi. Springer-Verlag, Berlin, 2006, pp. 358–390 (cit. on p. 21).

[31] W. R. Nelson, H. Hirayama, and D. W. O. Rogers. "The EGS4 code system". In: *Stanford Linear Accelerator Center, Report SLAC-256* (1985) (cit. on p. 22).

[32] N. J. Carron. *An Introduction to the Passage of Energetic Particles Through Matter*. Taylor and Francis Group, New York, 2007 (cit. on p. 22).

[33] Brian C. Franke, Ronald P. Kensek, T. W. Laub, and Martin J. Crawford. "ITS Version 6: The Integrated TIGER Series of Coupled Electron/Photon Monte Carlo Transport Code." In: *Revision 4 SAND2008-3331* (2009) (cit. on p. 22).

[34] Briesmeister J. F. "MCNP - A general Monte Carlo N-particle transport code. version 4C." In: *Los Alamos National Laboratory, NM; Report LA-13709-M* (2000) (cit. on p. 22).

[35] A. Fasso, A. Ferrari, and P. R. Sala. "Electron-photon transport in FLUKA: status". In: *Proceedings of the Monte Carlo 2000 Conference*. Ed. by A. Kling, F. Barao, M. Nakagawa, and L Tavora. Springer-Verlag, Berlin, 2001, pp. 159–164 (cit. on p. 22).

[36] Agostinelli S., J. Allison, and K. Amako. "GEANT4- a simulation toolkit". In: *Nucl Instrum Methods A* 506 (2003), pp. 250–303 (cit. on p. 22).

[37] M. A. King, S. J. Glick, P. H. Pretorious, R. G. Wells, H. C. Gifford, M. V. Narayanan, and T. H. Farncombe. "Attenuation, scatter, and spatial resolution compensation in SPECT". In: *Emission Tomography: the fundamentals of PET and SPECT*. Ed. by M. N. Wernick and J. N. Aarsvold. 1st. Elsevier Inc., 2004, pp. 473–498 (cit. on pp. 22, 25–27, 29, 30, 89–91).

[38] F. Buther. "Corrections for Physical Factors". In: *Correction Techniques in Emission Tomography*. Ed. by M. Dawood, X. Jiang, and K. Schafers. Series in Medical Physics and Biomedical Engineering. Boca Raton, Florida: CRC Press, 2012, pp. 67–95 (cit. on pp. 22, 25, 27, 89, 90).

[39] M. Ljungberg and S. E. Strand. "A Monte Carlo Program for the simulation of scintillation camera characteristics". In: *Comput. Methods Programs Biomed.* 29 (1989), pp. 257–272 (cit. on pp. 23, 36).

[40] R. L. Harrison and T. K. Lewellen. "The SimSET Program". In: *Monte Carlo Calculations in Nuclear Medicine: Applications in Diagnostic Imaging*. Ed. by M. Ljungberg, S. Strand, and M. A. King. Second Edition. CRC Press: Taylor & Francis Group, Florida, USA, 2012, pp. 77–92 (cit. on p. 23).

[41] M. F. Smith. "Vectorized Monte Carlo code for modeling photon transport in nuclear medicine". In: *Monte Carlo Calculations in Nuclear Medicine: Applications in Diagnostic Imaging*. Ed. by M. Ljungberg, S. E. Strand, and M. A. King. Institute of Physics Publishing, London, 1998, pp. 93–110 (cit. on p. 23).

[42] J. van den Hoff and J. Langner. "Handbook of Particle Detection and Imaging". In: ed. by C. Grupen and I. Buvat. Springer-Verlag, Berlin, 2012, pp. 1008–1042 (cit. on p. 23).

[43] K. Erlandsson, I. Buvat, P. H. Pretorious, B. A. Thomas, and B. F. Hutton. "A review of partial volume correction techniques for emission tomography and their applications in neurology, cardiology and oncology". In: *Phys. Med. Biol.* 57 (2012), R119–R159 (cit. on pp. 24, 25, 93).

[44] J. E. Bowsher, H. Yuan, L. W. Hedlund, T. G. Turkington, G. Akabani, A. Badea, W. C. Kurylo, C. T. Wheeler, G. P. Cofer, M. W. Dewhirst, and G. A. Johnson. "Utilizing MRI information to estimate F18-FDG distributions in

rat flank tumors". In: *IEEE Nuclear Science Symposium Conference Record* (2004), pp. 2488–2492 (cit. on pp. 24, 92, 94, 116).

[45] C. Chan, H. Liu, Y. Grobshtein, M. R. Stacy, A. J. Sinusas, and C. Liu. "Simultaneous Partial Volume Correction and Noise Regularization for Cardiac SPECT/CT". In: *IEEE Nuclear Science Symposium Conference Record* 1-6 (2013) (cit. on pp. 24, 93, 94).

[46] D. L. Barbee, R. T. Flynn, J. E. Holden, R. J. Nickles, and R. Jeraj. "A method for partial volume correction of PET imaged tumor heterogeneity using expectation maximization with a spatially varying point spread function". In: *Phys. Med. Biol.* 55 (2010), pp. 221–236 (cit. on p. 24).

[47] M. Shidahara, C. Tsoumpas, A. Hammers, N. Boussion, D Visvikis, T. Suhara, I. Kanno, and F. E. Turkheimer. "Functional and structural synergy for resolution recovery and partial volume correction in brain PET". In: *NeuroImage* 44 (2009), pp. 340–348 (cit. on p. 25).

[48] S. Shcherbinin and A. Celler. "Assessment of the severity of partial volume effects and the performance of two template-based correction methods in a SPECT/CT phantom experiment". In: *Phys Med Biol* 56 (2011), pp. 5355–5371 (cit. on pp. 25, 92).

[49] S. C. Moore, S. Southekal, M. A. Park, S. J. McQuaid, M. F. Kijewski, and S. P. Muller. "Improved regional activity quantitation in nuclear medicine using a new approach to correct for tissue partial volume and spillover effects". In: *IEEE Trans Med Imaging* 31 (2012), pp. 405–416 (cit. on pp. 25, 92).

[50] K. Erlandsson. "Basic Sciences of Nuclear Medicine". In: ed. by M. M. Khalil. Heidelberg: Springer, 2011, pp. 333–351 (cit. on pp. 25, 92).

[51] L. T. Chang. "A method for attenuation correction in radionuclide computed tomography". In: *IEEE Trans in Nucl Sci* 25 (1978), pp. 638–643 (cit. on pp. 25, 90).

[52] H. Zaidi and B. Hasegawa. "Determination of the Attenuation Map in Emission Tomography". In: *J Nucl Med* 44.2 (2003), pp. 291–315 (cit. on pp. 26, 27, 90).

[53] M. T. Madsen, P. T. Kirchner, J. P. Edlin, M. A. Nathan, and D. Kahn. "An emission-based technique for obtaining attenuation correction data for myocardial SPECT studies". In: *Nucl. Med. Comm.* 14 (1993), pp. 689–697 (cit. on p. 27).

[54] J. W. Wallis, T. R. Miller, and P. Koppel. "Attenuation correction in cardiac SPECT without a transmission measurement". In: *J Nucl Med* 36 (1995), pp. 506–512 (cit. on p. 27).

[55] T. S. Pan, M. A. King, D. S. Luo, S. T. Dahlberg, and B. J. Villegas. "Estimation of attenuation maps from scatter and photopeak window single photon emission computed tomographic images of technetium-99m labeled sestamibi". In: *J Nucl Card* 4 (1997), pp. 42–51 (cit. on p. 27).

[56] S. H. Manglos and T. M. Young. "Constrained IntraSPECT reconstruction from SPECT projections". In: *Proc. 1993 IEEE Medical Imaging Conf* (1994), pp. 1605–1609 (cit. on p. 27).

[57] J. Nuyts, P. Dupont, S. Stroobans, R. Benninck, L. Mortelmans, and P. Suetens. "Simultaneous maximum a posteriori reconstruction of attenuation and activity distributions from emission sinograms". In: *IEEE Trans Med Imaging* 18 (1999), pp. 393–403 (cit. on p. 27).

[58] B. F. Hutton, I. Buvat, and F. J. Beekman. "Review and current status of SPECT scatter correction". In: *Phys. Med. Biol.* 56 (2011), R85–R112 (cit. on pp. 27, 29, 30, 90, 91).

[59] R. J. Jaszczak, K. L. Greer, C. E. Jr. Floyd, C. C. Harris, and R. E. Coleman. "Improved SPECT quantitation using compensation for scattered photons". In: *J Nucl Med* 25 (1984), pp. 893–900 (cit. on pp. 28, 90).

[60] K. Ogawa, Y. Harata, T. Ichihara, A. Kubo, and S. Hasimoto. "A practical method for position-dependent Compton-scatter correction in single photon emission CT". In: *IEEE Trans Med Imaging* 10 (1991), pp. 408–412 (cit. on pp. 28, 90).

[61] T. Ichihara, K. Ogawa, N. Motomura, A. Kubo, and S. A. Hashimoto. "Compton scatter correction using tripple-energy window method for single and dual isotope SPECT". In: *J Nucl Med* 34 (1993), pp. 2216–2221 (cit. on pp. 28, 90).

[62] M. Y. Paek, J. S. Lee, D. S. Lee, J. K. Chung, and M. C. Lee. "Crosstalk and scatter correction in simultaneous dual isotope SPECT imaging using four energy window method". In: *IEEE Nuclear Science Symposium Conference Record* 2 (2000), pp. 13/153–13/156 (cit. on pp. 28, 90).

[63] K. F. Koral, X. Wang, W. L. Rogers, N. H. Clinthorne, and X. Wang. "Compton scattering correction by analysis of energy spectra". In: *J Nucl Med* 29 (1988), pp. 195–202 (cit. on pp. 29, 91).

[64] G. El Fakhri, P. Maksud, M.F. Kijewski, M.O. Habert, A. Todd-Pokropek, A. Aurengo, and S.C. Moore. "Scatter and Cross-Talk Corrections in Simultaneous Tc-99m/I-123 Brain SPECT using Constrained Factor Analysis and Artificial Neural Networks". In: *IEEE Trans in Nucl Sci* 47.4 (2000), pp. 1573–1580 (cit. on pp. 29, 91).

[65] S. Hapdey, M. Soret, and I. Buvat. "Quantification in simultaneous ^{99m}Tc/^{123}I brain SPECT using generalized spectral factor analysis: a Monte Carlo study". In: *Phys. Med. Biol.* 51 (2006), pp. 6157–6171 (cit. on pp. 29, 91).

[66] M X Zheng, I G Zubal, J P Seibyl, and M A King. "Correction for crosstalk contamination in dual radionuclide ^{99m}Tc and ^{123}I images using artificial neural network". In: *IEEE Trans. Nucl. Sci.* 51.5 (2004), pp. 2649–2653 (cit. on pp. 29, 91).

[67] J Bai, J Hashimoto, K Ogawa, T Nakahara, T Suzuki, and A Kubo. "Scatter correction based on an artificial neural network for ^{99m}Tc and ^{123}I dual isotope SPECT in myocardial and brain imaging". In: *Ann. Nucl. Med.* 21.1 (2007), pp. 25–32 (cit. on pp. 29, 91).

[68] I. Buvat, M. Rodriguez-Villafuerte, A. Todd-Pokropek, H. Benali, and R. Di Paola. "Comparative assessment of nine scatter correction methods based on spectral analysis using Monte Carlo simulations". In: *J Nucl Med* 36 (1995), pp. 1476–1488 (cit. on pp. 29, 91).

[69] B. Axelson, P. Msaki, and Israelson. "Subtraction of Compton Scatter photons in single-photon emission computed tomography". In: *J. Nucl. Med.* 25 (1984), pp. 490–494 (cit. on pp. 30, 91).

[70] P. Msaki, B. Axelsson, C. M. Dahl, and S. A. Larsson. "Generalized scatter correction method in SPECT using point scatter distribution functions". In: *J Nucl Med* 28.1861-1869 (1987) (cit. on pp. 30, 91).

[71] S. R. Meikle, B. F. Hutton, and D. L. Bailey. "A transmission dependent method for scatter correction in SPECT". In: *J Nucl Med* 35 (1994), pp. 360–367 (cit. on pp. 30, 91).

[72] B. F. Hutton, A. Osieck, and S. R. Meikle. "Transmission-based scatter correction of 180^o myocardial single-photon emission tomographic studies". In: *Eur J Nucl Med* 23 (1996), pp. 1300–1308 (cit. on pp. 30, 91).

[73] F. J. Beekman, J. M. den Harder, M. A. Viergever, and P. P. van Rijk. "SPECT scatter modeling in non-uniform attenuating objects". In: *Phys. Med. Biol.* 42 (1997), pp. 1133–1142 (cit. on p. 30).

[74] E. C. Frey and B. M. W. Tsui. "A practical method for incorporating scatter in a projector-backprojector for accurate scatter compensation in SPECT". In: *IEEE Trans in Nucl Sci* 40 (1993), pp. 1107–1116 (cit. on pp. 30, 91).

[75] D. J. Kadrmas, E. C. Frey, S. S. Karimi, and B. M. W. Tsui. "Fast implementations of reconstruction-based scatter compensation in fully 3D SPECT image reconstruction". In: *Phys. Med. Biol.* 43 (1998), pp. 857–873 (cit. on p. 30).

[76] F. J. Kamphuis C. Beekman, P. P. van Rijk, and M. A. Viergever. "Dual matrix ordered subsets reconstruction for accelerated 3D scatter compensation in single-photon emission tomography". In: *Eur J Nucl Med* 25 (1998), pp. 8–18 (cit. on p. 30).

[77] T. H. Farncombe, H. C. Gifford, M. V. Narayanan, P. H. Pretorius, E. C. Frey, and M. A. King. "Assessment of scatter compensation strategies for (67)Ga SPECT using numerical observers and human LROC studies". In: *J Nucl. Med.* 45 (2004), pp. 802–812 (cit. on pp. 30, 91).

[78] Y. Du, B. M. W. Tsui, and E. C .Frey. "Model-based compensation for quantitative ^{123}I brain SPECT imaging". In: *Phys. Med. Biol.* 51 (2006), pp. 1268–1282 (cit. on pp. 30, 91).

[79] I. Laurette, G. L. Zeng, A. Welch, P. E. Christian, and G. T. Gullberg. "A three-dimensional ray-driven attenuation, scatter and geometric response correction technique for SPECT in inhomogeneous media". In: *Phys. Med. Biol.* 45 (2000), pp. 3459–3480 (cit. on pp. 30, 91).

[80] D. Lazaro, Z. El Bitar, V. Breton, D. Hill, and I. Buvat. "Fully 3D Monte Carlo reconstruction in SPECT: a feasibility study". In: *Phys. Med. Biol.* 50 (2005), pp. 3739–3754 (cit. on pp. 30, 91).

[81] H.W.A.M. deJong, E. T. P. Slijpen, and F.J. Beekman. "Acceleration of Monte Carlo SPECT simulation using convolution-based forced detection". In: *IEEE Trans Nucl Sci* 48 (2001), pp. 58–64 (cit. on pp. 30, 35, 50, 52, 54, 92).

[82] S. Liu, M. A. King, A. B. Brill, M. G. Stabin, and T. H. Farncombe. "Convolution-Based Forced Detection Monte Carlo Simulation Incorporating Septal Penetration Modeling". In: *IEEE Trans in Nucl Sci* 55.3 (2008), pp. 967–974 (cit. on pp. 30, 34, 35, 50, 58, 73, 92).

[83] H. W. A. M. deJong, F J Beekman, M A Viergever, and P. P. vanRijk. "Simultaneous ^{99m}Tc/^{201}Tl dual-isotope SPET with Monte Carlo-based down-scatter correction". In: *Eur. J. Nucl. Med.* 28.8 (2002), pp. 1063–1071 (cit. on pp. 30, 92, 117).

[84] J Ouyang, G. EL Fakhri, and S C Moore. "Fast Monte Carlo based joint iterative reconstruction for simultaneous ^{99m}Tc/^{123}I SPECT imaging". In: *Med. Phys.* 34.8 (2007), pp. 3263–3272 (cit. on pp. 30, 92).

[85] M. I. Karamat and T. H. Farncombe. "Accelerated Monte Carlo based Simultaneous ^{99m}Tc/^{123}I SPECT Reconstruction". In: *Proc. 2012 IEEE Medical Imaging Conf* (2012), pp. 3337–3343 (cit. on pp. 30, 34, 92).

[86] M. I. Karamat and T. H. Farncombe. "Simultaneous ^{99m}Tc/^{111}In SPECT Reconstruction using Accelerated Convolution based Forced Detection Monte Carlo". In: *IEEE Trans in Nucl Sci* 62.5 (2015), pp. 2085–2095 (cit. on pp. 30, 34, 35, 50, 92).

[87] I. Buvat and D. Lazaro. "Monte Carlo simulations in emission tomography and GATE: An overview". In: *Nucl Instrum Methods A* 569 (2006), pp. 323–329 (cit. on p. 33).

[88] X Song, W P Segars, Y Du, B M W Tsui, and E C Frey. "Fast modelling of the collimator-detector response in Monte Carlo simulation of SPECT imaging using the angular response function." In: *Phys Med Biol* 50.8 (2005-04), pp. 1791–804. ISSN: 0031-9155 (cit. on p. 33).

[89] S. Jan, G. Santin, D. Strul, S. Staelens, and K. Assie*et al.* "GATE: a simulation toolkit for PET and SPECT". In: *Phys Med Biol* 49 (2004), pp. 4543–4561 (cit. on pp. 33, 59).

[90] K. Assie, V. Breton, I. Buvat, C. Comtat, and *et al.* "Monte Carlo simulation in PET and SPECT instrumentation using GATE". In: *Nucl Instrum Methods A* 527 (2004), pp. 180–189 (cit. on p. 33).

[91] K. Assie, I. Gardin, P. Vera, and I. Buvat. "Validation of Monte Carlo simulator GATE for indium-111 imaging". In: *Phys Med Biol* 50 (2005), pp. 3113–3125 (cit. on pp. 34, 36, 59).

[92] H.W.A.M. deJong, F.J. Beekman, M.A. Viergever, and P.P. van Rijk. "Simultaneous ^{99m}Tc/^{201}Tl dual-isotope SPET with Monte Carlo-based down-scatter correction". In: *Eur J Nucl Med* 29 (2002), pp. 1063–1071 (cit. on pp. 34, 54, 55).

[93] J. Ouyang, G. El Fakhri, and C. S. Moore. "Fast Monte Carlo based joint iterative reconstruction for simultaneous ^{99m}Tc/^{123}I SPECT imaging". In: *Med Phys* 34.8 (2007), pp. 3263–3272 (cit. on pp. 34, 35, 54, 55, 72, 87).

[94] M. Cervo and S. C. Moore. "Evaluation of Monte Carlo-based compensation for scatter and crosstalk in simultaneous In-111/Tc-99m SPECT-CT imaging of infection". In: *Proc. 2011 IEEE Medical Imaging Conf* (2011), pp. 3804–3806 (cit. on pp. 34, 54).

[95] T. H. Farncombe, S. Liu, M. A. King, A. B. Brill, and M. G. Stabin. "Accelerated SPECT Monte Carlo simulation using convolution-based forced detection". In: *Proc. Soc. Nuclear Med. Annu. Conf.* 2006 (cit. on p. 34).

[96] X. He, E. C. Frey, M. Links, X. Song, and B. M. W. Tsui. "Comparison of Penetration and Scatter Effects on Defect Contrast for GE and Siemens LEHR Collimators in Myocardial Perfusion SPECT—A Simulation Study". In: *IEEE Trans. Nucl. Sci.* 52.5 (2005), pp. 1359–1364 (cit. on p. 34).

[97] G. El Fakhri, M. F. Kijewski, P. Maksud, and S. C. Moore. "The effects of compensation for scatter, lead X-rays, and high-energy contamination on tumor detectability and activity estimation in Ga-67 imaging". In: *IEEE Trans. Nucl. Sci.* 50.3 (2003), pp. 439–445 (cit. on p. 34).

[98] Y. Du, E. C. Frey, W. T. Wang, C. Tocharoenchai, W. H. Baird, and B. M. W. Tsui. "Combination of MCNP and SimSET for Monte Carlo simulation of SPECT with medium- and high-energy photons". In: *IEEE Trans. Nucl. Sci.* 49.3 (2002), pp. 668–674 (cit. on p. 34).

[99] S. Staelens, T. de Wit, and F. Beekman. "Fast hybrid SPECT simulation including efficient septal penetration modelling (SP-PSF)". In: *Phys Med Biol* 52 (2007), pp. 3027–3043 (cit. on p. 35).

[100] X. Song, E C Frey, W T Wang, Y Du, and B. M. W. Tsui. "Validation and evaluation of model-based crosstalk compensation method in simultaneous ^{99m}Tc stress and ^{201}Tl rest myocardial perfusion SPECT". In: *IEEE Trans. Nucl. Sci.* 51.1 (2004), pp. 72–79 (cit. on p. 35).

[101] M. Ljungberg. *The SIMIND Monte Carlo Program*. URL: `http://www2.msf.lu.se/simind/` (cit. on p. 36).

[102] I. Buvat and S. Jan. *Users Guide V7.2: From GATE collaborative documentation wiki*. URL: `http://www.opengatecollaboration.org/` (cit. on p. 36).

[103] M. Holstensson, M. Partridge, S. E. Buckley, and G. D. Flux. "The effect of energy and source location on gamma camera intrinsic and extrinsic spatial resolution: an experimental and Monte Carlo study". In: *Phys. Med. Biol.* 55 (2010), pp. 1735–1751 (cit. on p. 36).

[104] Z. Wang and A. C. Bovik. "A universal Image qulaity index". In: *IEEE Signal Process. Lett.* 9.3 (2002), pp. 81–84 (cit. on pp. 37, 38).

[105] Z. Wang, A. C. Bovik, H. R. Sheikh, and E. P. Simoncelli. "Image Quality Assessment: From Error Visibility to Structural Similarity". In: *IEEE Trans Image Proc* 13.4 (2004), pp. 600–612 (cit. on p. 38).

[106] W. P. Segars, G. Sturgeon, S. Mendonca, J. Grimes, and B. M. W. Tsui. "4D XCAT phantom for multimodality imaging research". In: *Med Phys* 37.9 (2010), pp. 4902–4915 (cit. on p. 38).

[107] S. Shcherbinin, S. Chamoiseau, and A. Celler. "Simulation-based reconstruction of absolute activities from the ^{99m}Tc/^{111}In dual-isotope SPECT/CT: phantom experiments and imaging of neuroendocrine tumors". In: *Phys Med Biol* 58 (2013), pp. 3339–3357 (cit. on pp. 50, 71).

[108] R. Zhou, D. H. Thomas, H. Qiao, H. S. Bal, S. R. Choi, A. Alavi, V. A. Ferrari, H. V. Kung, and P.D. Acton. "In vivo detection of stem cells grafted in infarcted rat myocardium". In: *J. Nucl. Med.* 46 (2005), pp. 816–822 (cit. on pp. 50, 53).

[109] R. Zhou, D. H. Thomas, and V. A. Ferrari. "Imaging stem cells implanted in infarcted myocardium". In: *J. Am. College Cardiol.* 48 (2006), pp. 2094–2106 (cit. on pp. 50, 53).

[110] H.P Simonian, A. H. Maurer, L. C. Knight, S. Kantor, V. Megalooikonomou, R. S. Fisher, and H. P. Parkman. "Simultaneous assessment of gastric accommodation and emptying: studies with liquid and solid meals". In: *J Nucl Med* 45 (2004), pp. 1155–1160 (cit. on pp. 50, 53).

[111] J. C. Quintana and M. J. Blend. "The dual-isotope Prostascint imaging procedure: clinical experience and staging results in 145 patients". In: *Clin Nucl Med* 25 (2000), pp. 33–40 (cit. on pp. 50, 53).

[112] M. J. Blend and V. A. Bhadkamkar. "Impact of radioimmunoscintigraphy on management of colorectal and ovarian cancer patients: a retrospective study". In: *Cancer Invest* 16 (1998), pp. 431–441 (cit. on pp. 50, 53).

[113] M. I. Karamat. "Strategies and scientific basis of dose reduction on state-of-the-art multi-row detector X-ray CT systems". In: *Crit Rev Biomed Eng* 43.1 (2015), pp. 33–59 (cit. on p. 51).

[114] S. I. Heiba, D. Kolker, B. Mocherla, K. Kapoor, M. Jiang, H. Son, B. Rangaswamy, L. Kostakoglu, I. Savitch, M. DaCosta, and J. Machac. "The optimized evaluation of diabetic foot infection by dual isotope SPECT/CT imaging protocol". In: *J. Foot Ankle Surg* 49 (2010), pp. 529–536 (cit. on p. 53).

[115] M. Y. Paek, J. S. Lee, D. S. Lee, J. K. Chung, and M. C. Lee. "Crosstalk and scatter correction in simultaneous dual isotope SPECT imaging using four energy window method". In: *IEEE Nuclear Science Symposium Conference Record* 2 (2000), pp. 13/153–13/156 (cit. on pp. 54, 76).

[116] S. C. Moore, R. J. English, C. Syravanh, D. E. Tow, R. E. Zimmerman, K. H. Chan, and M. F. Kijewski. "Simultaneous Tc-99m/Tl-201 imaging using energy based estimation of the spatial distribution of contaminant photons". In: *IEEE Trans Nucl Sci* 42.3 (1995), pp. 1189–1195 (cit. on pp. 54, 76).

[117] J. M. Links, J. L. Prince, C. Syravanh, and S. N. Gupta. "A vector Wiener filter for dual radionuclide imaging". In: *IEEE Trans Med Imaging* 42.3 (1996), pp. 1189–1195 (cit. on pp. 54, 76).

[118] J. Feng and B. C. Penny. "Accurate spill-down and scatter correction for Tc-99m/In-111 SPECT". In: *Proc. 2002 IEEE Medical Imaging Conf* (2003), pp. 1562–1566 (cit. on p. 54).

[119] T. Ichihara, K. Ogawa, N. Motomura, A. Kubo, and S. A. Hashimoto. "Compton scatter correction using tripple-energy window method for single and dual isotope SPECT". In: *J Nucl Med* 34 (1993), pp. 2216–2221 (cit. on pp. 54, 61).

[120] W. T. Wang, E. C. Frey, B. M. W. Tsui, and C. Tocharoenchai. "A model-based crosstalk compensation method for simultaneous Tl-201 and Tc-99m dual isotope myocardial SPECT imaging". In: *Proc. 2001 IEEE Medical Imaging Conf* 4 (2001), pp. 1732–1736 (cit. on pp. 54, 76, 118).

[121] X. Song, E. C. Frey, W. T. Wang, and B. M. W. Tsui. "Validation and evaluation of model-based crosstalk compensation method in simultaneous ^{99m}Tc stress and ^{201}Tl rest myocardial perfusion SPECT". In: *IEEE Trans Nucl Sci* 51.1 (2004), pp. 72–79 (cit. on pp. 54, 76, 117).

[122] Y. Du and E. C. Frey. "Quantitative evaluation of simultaneous reconstruction with model-based crosstalk compensation Tc-99m/I-123 dual isotope simultaneous acquisition brain SPECT". In: *Med Phys* 36.6 (2009), pp. 2021–2033 (cit. on pp. 54, 76).

[123] D. J. Kadrmas, E. C. Frey, and B. M. W. Tsui. "Simultaneous technetium-99m/thallium-201 SPECT imaging with model-based compensation for cross-contaminating effects". In: *Phys Med Biol* 44 (1999), pp. 1843–1860 (cit. on p. 54).

[124] M. X. Zheng, I. G. Zubal, J. P. Seibyl, and M. A. King. "Correction for crosstalk contamination in dual radionuclide ^{99m}Tc and ^{123}I images using artificial neural network". In: *IEEE Trans Nucl Sci* 51.1 (2004), pp. 2649–2653 (cit. on pp. 55, 77).

[125] J. Bai, J. Hashimoto, K. Ogawa, T. Nakahara, T. Suzuki, and A. Kubo. "Scatter correction based on an artificial neural network for ^{99m}Tc and ^{123}I dual isotope SPECT in myocardial and brain imaging". In: *Ann Nucl Med* 21.1 (2007), pp. 25–32 (cit. on pp. 55, 77).

[126] C. J. Chang, W. S. Huang, K. H. Su, and J. C. Chen. "Separation of two radionuclides in simultaneous dual-isotope imaging with independent component analysis". In: *Biomed. Eng. Appl. Basis Comm.* 18 (2006), pp. 264–269 (cit. on pp. 55, 77).

[127] "Emission Tomography: the fundamentals of PET and SPECT". In: ed. by M. N. Wernick and J. N. Aarsvold. 1st. Elsevier Inc., 2004. Chap. Simulation Techniques and Phantoms, pp. 551–561 (cit. on p. 55).

[128] H. M. Hudson and R. S. Larkin. "Accelerated image reconstruction using ordered subsets of projection data". In: *IEEE Trans in Med Imaging* 13.4 (1993), pp. 601–604 (cit. on pp. 56, 77).

[129] T. H. Farncombe, S. Liu, M. A. King, A. B. Brill, and M. G. Stabin. "Accelerated SPECT Monte Carlo simulation using convolution-based forced detection". In: *Proc. Soc. Nuclear Med. Annu. Conf* (2006) (cit. on p. 58).

[130] C. E. Floyd Jr, R. J. Jaszczak, and R. E. Coleman. "Scatter detection in SPECT imaging: dependence on source depth, energy, and energy window". In: *Phys Med Biol* 33.9 (1988), pp. 1075–1081 (cit. on p. 71).

[131] R. J. Bennink, L. J.Rijsk, L. A. Noordyun, A. G. Jenssen, and G. W. Sloof. "Estrogen receptor status in primary breast cancer: Iodine 123-labelled cis-11β -methoxy-17α -iodovinyl Estradiol scintigraphy". In: *Radiology* 220.3 (2001), pp. 774–779 (cit. on pp. 75, 84).

[132] B. VanD. Bossche and C. VanD. Wiele. "Receptor imaging in oncology by means of nuclear medicine: current status". In: *J Clin Oncol* 22.17 (2004), pp. 3593–3607 (cit. on p. 75).

[133] R. J. Bennink, G. V. Tienhoven, L. J. Rijsk, L. A. Noordyun, A. G. Jenssen, and G. W. Sloof. "In vivo prediction of response to antiestrogen treatment in estrogen receptor-positive breast cancer". In: *J Nucl. Med.* 45 (2004), pp. 1–7 (cit. on p. 75).

[134] L. Zhou, J. Oldan, P. Fisher, and G. Gindi. "Low-contrast detection in tomosynthesis breast imaging using a realistic breast phantom". In: *Proc. SPIE* (2006) (cit. on p. 78).

[135] K. Bliznakova, Z. Bliznakov, V. Bravou, Z. Kolitsi, and N. Pallikarakas. "A three dimensional breast software phantom for mammography simulation". In: *Phys. Med. Biol.* 48 (2003), pp. 3699–3719 (cit. on p. 78).

[136] M. I. Karamat and T. H. Farncombe. "A Comparison between GATE and Accelerated Convolution-based Forced Detection SIMIND for Low- and Medium-energy Collimators: A Simulation Study". In: *IEEE Trans in Nucl Sci* (2016), Accepted for publication (cit. on pp. 92, 95).

[137] K. Vunckx, A. Atre, K. Baete, A. Reilhac, C. M. Deroose, K. Van Laere, and J. Nyuts. "Evaluation of Three MRI-Based Anatomical Priors for Quantitative PET Brain Imaging". In: *IEEE Trans. Med. Imag.* 31.3 (2012), pp. 599–612 (cit. on p. 94).

[138] P. H. Pretorius, M. A. King, T. S. Pan, D. J. de Vries, S. J. Glick, and C. L. Byrne. "Reducing the influence of the partial volume effect on SPECT activity quantitation with 3D modelling of spatial resolution in iterative reconstruction". In: *Phys. Med. Biol.* 43 (1998), pp. 407–420 (cit. on p. 96).

[139] P. H. Pretorius, M. A. King, T-S Glick S. J. Pan, and D. S. Luo. "Reducing the effect of non-stationary resolution on activity quantitation with the frequency distance relationship in SPECT". In: *IEEE Trans in Nucl Sci* 43 (1996), pp. 3335–3341 (cit. on p. 97).

[140] K. Vunckx, M. Germino, Y. Jian, C. Chan, J. Nyuts, and R. E. Carson. "A Simple and Flexible MAP Approach for Static and Dynamic Emission Tomography Reconstruction". In: *Proc. 2014 IEEE Medical Imaging Conf* (2014), In press (cit. on pp. 111, 114, 119).

[141] K. Kacperski, K. Erlandsson, S. Ben-Haim, D. Van Gramberg, and B. F. Hutton. "Iterative deconvolution of simultaneous dual radionuclide projections for CdZnTe based cardiac SPECT". In: *Proc. 2008 IEEE Medical Imaging Conf* (2008), pp. 5260–5263 (cit. on p. 117).

[142] S. Ben Haim, K Kacperski, S Hain, D. Van Gramberg, K Erlandsson B F Hutton, N Roth, W A Waddington, D S Berman, and P J Ell. "Simultaneous dual-radionuclide myocardial perfusion imaging with solid state dedicated cardiac camera". In: *Eur. J. Nucl. Med.* 37 (2010), pp. 1710–1721 (cit. on p. 117).

[143] W T Wang, B. M. W. Tsui, D S Lalush, C Tocharoenchai, and E C Frey. "Optimization of acquisition parameters for simultaneous ^{201}Tl and ^{99m}Tc dual-isotope myocardial imaging". In: *IEEE Trans. Nucl. Sci.* 52.5 (2005), pp. 1227–1235 (cit. on p. 118).

[144] Y Du, E C Frey, W T Wang, and B. M. W. Tsui. "Optimization of acquisition energy windows in Simultaneous ^{99m}Tc/^{123}I brain SPECT". In: *IEEE Trans. Nucl. Sci.* 50.5 (2003), pp. 1556–1561 (cit. on p. 118).

[145] X. Song, E C Frey, X He, W. P. Segars, and B. M. W. Tsui. "A mathematical observer study for evaluation of a model-based compensation method for crosstalk in simultaneous dual isotope SPECT". In: *IEEE Nuclear Science Symposium Conference Record*. 2003 (cit. on p. 118).

[146] B. L. R. Kam, J. J. M. Teunissen, E. P. Krenning, W. W. de Herder, S. Khan, E. I. van Vliet, and D. J. Kwekkeboom. "Lutetium-labelled peptides for therapy of neuroendocrine tumours". In: *Eur. J. Nucl. Med.* 39.1 (2012), S103–112 (cit. on p. 119).

[147] J. Svensson. "Targeted radionuclide therapy for patients with neuroendocrine tumours". PhD thesis. Gothenburg, Sweden: University of Gothenburg, 2016 (cit. on p. 119).

[148] R. P. Baum, H. R. Kulkarni, C. Schuchardt, A. Singh, M. Wirtz, S. Wiessalla, M. Schottelius, D. Mueller, I. Klette, and H. Wester. "Lutetium-177 PSMA Radioligand Therapy of Metastatic Castration-Resistant Prostate Cancer: Safety and Efficacy". In: *J Nucl. Med.* (2016) (cit. on p. 119).

[149] P. J. Kinsman and N. Nicolici. "NoC-based FPGA acceleration for Monte Carlo simulations with applications to SPECT imaging". In: *IEEE Trans. Computers* 62.3 (2013), pp. 524–535 (cit. on p. 119).

[150] K. Van Slambrouck and J. Nyuts. "Reconstruction Scheme for Accelerated Maximum Likelihood Reconstruction: The Patchwork Structure". In: *IEEE Trans Nucl Sci* 61.1 (2014), pp. 173–181 (cit. on p. 119).

Appendix A

A.1 Center Slice Theorem

$$P(\omega,\theta) = \int_{-\infty}^{\infty} p(s,\theta) exp(-j2\pi\omega s) ds$$

Using Equation 1.2

$$\begin{aligned} &= \int_{-\infty}^{\infty} \left[\int_{-\infty}^{\infty} \int_{-\infty}^{\infty} f(x,y)\delta(\mathbf{x}\cdot\boldsymbol{\theta} - s) dxdy \right] exp(-j2\pi\omega s) ds \\ &= \int_{-\infty}^{\infty} \int_{-\infty}^{\infty} f(x,y) \left[\int_{-\infty}^{\infty} \delta(\mathbf{x}\cdot\boldsymbol{\theta} - s) exp(-j2\pi\omega s) ds \right] dxdy \\ = \int_{-\infty}^{\infty} \int_{-\infty}^{\infty} f(x,y) exp(-j2\pi(\mathbf{x}\cdot\boldsymbol{\theta})\omega) dxdy &= F((\mathbf{x}\cdot\boldsymbol{\theta})\omega) = F(\omega_x,\omega_y) \end{aligned}$$

where $\omega_x = \omega cos\theta$ and $\omega_y = \omega sin\theta$.

A.2 Backprojection

By definition of inverse Fourier transform, a $2-$D activity distribution $f(x,y)$ can be obtained from its Fourier transform $F(\omega_x,\omega_y)$, as:

$$f(x,y) = \int_{-\infty}^{\infty} \int_{-\infty}^{\infty} F(\omega_x,\omega_y) e^{j2\pi(\omega_x+\omega_y)} d\omega_x d\omega_y$$

Conversion to polar coordinates ω and θ yields

$$= \int_0^{2\pi} \int_{-\infty}^{\infty} F(\omega cos\theta, \omega sin\theta) e^{j2\pi(\omega cos\theta + \omega sin\theta)} \omega d\omega d\theta$$

Use of center slice theorem from Appendix A.1 gives

$$= \int_0^{2\pi} \int_{-\infty}^{\infty} P(\omega, \theta) e^{j2\pi(\omega cos\theta + \omega sin\theta)} \omega d\omega d\theta$$

We know that in frequency domain $P(\omega, \theta + \pi) = P(-\omega, \theta)$ which implies above Equation can also be written as:

$$= \int_0^{\pi} \int_0^{\infty} P(-\omega, \theta) e^{j2\pi(\omega cos(\theta+\pi) + \omega sin(\theta+\pi))} \omega d\omega d\theta$$

or

$$= \int_0^{\pi} \int_{-\infty}^{0} P(\omega, \theta) e^{j2\pi(\omega cos\theta + \omega sin\theta)} (-\omega) d\omega d\theta$$

i.e.

$$= \int_0^{\pi} \int_{-\infty}^{\infty} P(\omega, \theta) e^{j2\pi(\omega cos\theta + \omega sin\theta)} |\omega| d\omega d\theta$$

This shows that object activity distribution, $f(x, y)$, can only be recovered through backprojecting a version of inverse Fourier transform $F(\omega_x, \omega_y)$ (i.e. inverse Fourier transform of projection data according to center slice theorem) scaled by $|\omega|$ in frequency domain.